

THERMOMECHANICAL BEHAVIOR AND MICROSTRUCTURE EVOLUTION
OF TANTALUM THIN FILMS DURING THE BETA-ALPHA PHASE
TRANSFORMATION

A Dissertation

Presented to the Faculty of the Graduate School

of Cornell University

In Partial Fulfillment of the Requirements for the Degree of

Doctor of Philosophy

by

Robert Alan Knepper

January 2007

© 2007 Robert Alan Knepper

THERMOMECHANICAL BEHAVIOR AND MICROSTRUCTURE EVOLUTION
OF TANTALUM THIN FILMS DURING THE BETA-ALPHA PHASE
TRANSFORMATION

Robert Alan Knepper, Ph. D.

Cornell University 2007

Thin tantalum films were prepared on oxidized silicon substrates in the metastable β phase using an ultra-high vacuum sputter deposition system. Stresses that arose in the films due to interactions between the film and substrate during thermal cycles from room temperature to 700°C were measured using an *in situ* substrate curvature measurement system, allowing oxygen content to be controlled during both deposition and thermal cycling. X-ray diffraction experiments were used to determine crystal phase and orientation before and after cycling. The transformation from the β phase to the stable α phase takes place in conjunction with a distinct jump in stress in the tensile direction. The magnitude of the jump and the temperature at which it occurs were strongly affected by the amount of oxygen to which the film is exposed and whether the exposure took place during deposition, between deposition and thermal cycling, or during thermal cycling. Increasing oxygen content inhibited the phase transformation, requiring higher temperatures to complete it. It is shown that the phase transformation must occur by thermally activated hopping of atoms across the phase boundaries, and it is proposed that oxygen added to the system inhibits the transformation by slowing boundary motion through solute drag.

The microstructure of phase-transformed films were studied using electron backscatter diffraction (EBSD). A unique, previously unobserved microstructure was

found, characterized by smooth, continuous gradients in crystal orientation of up to $4^\circ/\mu\text{m}$ over distances of up to $6\ \mu\text{m}$ within individual grains. Rotation axes were analyzed using rotation pole figures and compared to those of dislocation arrays that could cause such orientation gradients to occur. The addition of oxygen during deposition was found to have a large effect on the microstructure, leading to much larger grain sizes, lower angle grain boundaries, and smaller orientation gradients within grains.

Biographical Sketch

Rob was born and raised in Erie, PA. He attended Penn State University and graduated with a bachelor's degree in Engineering Science. He then spent a year working as a methods engineer at Sandvik Coromant in Fair Lawn, NJ before deciding that manufacturing is rather boring. He then returned to Penn State for a master's degree in Engineering Science, where he decided that a career in research would be a much more interesting way to spend his life. As such, he decided to come to the Materials Science and Engineering Department at Cornell University. During his time at Cornell, Rob has grown quite fond of the Ithaca area; it's wonderful landscapes and varied terrain, the variety of music and arts, and the plethora of wineries in the vicinity. Upon completion of his degree, Rob is looking forward to taking a vacation before beginning his post-doctoral work.

Acknowledgements

There are a great number of people I would like to acknowledge for their contributions both to my research and for making my time at Cornell one of the most rewarding and enjoyable periods of my life. First and foremost, I want to thank my advisor, Shefford Baker. His attention to detail in both experimentation and in communicating results has shown me what it means to be a research scientist. I greatly appreciate his dedication to my project in the face of numerous experimental and financial setbacks, and I will always fondly remember having to “translate” between Shef and Ray during our discussions about rotation axes.

I would also like to thank my committee members, Matthew Miller and Stephen Sass, for their advice and support.

I want to thank the members of the Baker research group, past and present, for all of their help throughout my time at Cornell. Thanks to Jon Shu for all his work on the UHV system and for teaching me how to use it, and to Prita Pant, Dave Nowak, and Aaron Vodnick for useful discussions. Special thanks to Ray Fertig for all of his help in analyzing crystal orientation and rotation axis data and to undergraduate students Kate Jackson, Blake Stevens, and Max Aubain who put in countless hours working with me on various aspects of this project.

I thank CCMR facilities managers John Hunt, John Grazul, and Maura Weathers for all of their help in refining my experimental procedures, and John Sinnott for his help in troubleshooting problems with the UHV system.

The financial support of the following agencies and facilities is gratefully

acknowledged: U.S. Department of Energy (grant number DE-FG02-02ER46001), the x-ray, electron microscopy, and ion beam facilities of the Cornell Center for Materials Research (CCMR) with support from the National Science Foundation Materials Research Science and Engineering Centers (MRSEC) program (DMR-0079992), U.S. Department of Education (GAANN Fellowship award P200A000800-02), the National Science Foundation (CAREER award DMR-9875119), the Office of Naval Research (Grant No. N00014-99-1-0650 DURIP), and Cornell University. Additionally, I would like to thank Hewlett-Packard for providing the impetus for this project (even if their financial support was never realized).

Thanks to all of my friends who made my years in Ithaca some of the best of my life. Thanks to Karen Downey and Joe Ford for always being there for me, introducing me to the wines of the Finger Lakes, and welcoming me into their home these past few months while I completed my dissertation. Thanks to James and Heidi Miller for helping keep me sane by showing me how crazy my life could be. To James, Heidi, Karen, Joe, Shawn Allison, and Anne Geiger, thanks for all the great times at chorale. I consider myself privileged to have performed with you and will always be proud of the music we made. Thanks to all of my gaming friends for a good laugh whenever I needed one; to the poker group—thanks for stopping by.

Finally, I want to thank my family and especially my parents, Robert and Candis Knepper, for their love and support through the years. Thanks everyone; I couldn't have done it without you!

Table of Contents

1	Introduction.....	1
1.1	Motivation.....	1
1.2	Structure of this thesis.....	2
1.3	Tantalum thin films.....	3
1.3.1	Deposition and crystal structure.....	4
1.3.2	Dependence of stress on deposition conditions in β -Ta.....	9
1.3.3	Thermal cycling and microstructure evolution.....	14
1.3.3.1	Grain growth.....	15
1.3.3.2	Oxygen incorporation.....	15
1.3.3.3	Phase transformation.....	16
1.4	Kinetics of solid-solid phase transformations.....	19
1.4.1	Diffusion.....	21
1.4.2	Kinetics of boundary migration and solute drag.....	25
1.4.3	Kinetics of phase transformations.....	27
1.4.3.1	Nucleation and growth.....	27
1.4.3.2	Shear transformations.....	28
2	Experimental Details.....	35
2.1	Overview.....	35
2.2	Film deposition and thermal cycling.....	35
2.3	Microstructure analysis.....	39
2.3.1	X-ray diffraction.....	40
2.3.2	Electron backscatter diffraction (EBSD).....	42
2.3.3	Film thickness measurements.....	49
3	Effect of oxygen on the thermomechanical behavior of tantalum thin films during the β-α phase transformation.....	51
3.1	Abstract.....	51
3.2	Introduction.....	52
3.3	Experiment.....	56
3.3.1	Sample preparation.....	56
3.3.2	Thermal cycling and stress measurements.....	57
3.3.3	Microstructural characterization.....	58
3.4	Films without added oxygen.....	59
3.4.1	Results.....	59
3.4.2	Discussion.....	64

3.5	Films exposed to oxygen.....	68
3.5.1	Oxygen incorporated during deposition.....	68
3.5.1.1	Oxygen content.....	68
3.5.1.2	Thermomechanical results.....	69
3.5.1.3	Discussion.....	72
3.5.2	Oxygen exposure between deposition and testing.....	77
3.5.2.1	Oxygen content.....	77
3.5.2.2	Thermomechanical results.....	78
3.5.2.3	Discussion.....	78
3.5.3	Oxygen incorporated during thermal cycling.....	80
3.5.3.1	Oxygen content.....	80
3.5.3.2	Thermomechanical results.....	81
3.5.3.3	Discussion.....	81
3.6	Summary and Conclusions.....	84
3.7	Acknowledgements.....	85
4	Driving Force and Activation Energy of the β-α Phase Transformation in Tantalum Thin Films.....	91
5	Coefficient of Thermal Expansion and Biaxial Elastic Modulus of β Phase Tantalum Thin Films.....	99
6	Microstructure of Phase-transformed Tantalum Films.....	108
6.1	Abstract.....	108
6.2	Introduction.....	109
6.3	Experiment.....	109
6.3.1	Sample preparation.....	109
6.3.2	Microstructure characterization.....	111
6.4	EBSD orientation maps.....	112
6.4.1	Analysis.....	112
6.4.2	Results.....	113
6.4.3	Discussion.....	114
6.5	Rotation pole figures.....	120
6.5.1	Analysis.....	120
6.5.2	Results.....	121
6.5.3	Discussion.....	124
6.6	General discussion.....	127
6.7	Conclusions.....	128
7	Effect of Oxygen on the Microstructure of Phase-transformed Tantalum Films.....	131
7.1	Abstract.....	131
7.2	Introduction.....	132

7.3	Experiment.....	134
	7.3.1 Sample preparation.....	134
	7.3.2 Microstructure characterization.....	135
7.4	Results.....	135
7.5	Discussion.....	145
7.6	Conclusions.....	147
8	Summary and Conclusions.....	149

List of figures

1.1	Crystal structure β tantalum (viewed down the c -axis) as described by Arakcheeva <i>et al.</i> . The black and white circles indicate two consecutive levels of the primary atomic nets separated by $0.5c$ (host sublattice). The gray atoms indicate the channel atoms of the guest sublattices, located midway between the primary nets. The numbers indicate crystallographically equivalent positions within the unit cell.....	5
1.2	(a) Fraction of α Ta as a function of argon ion energy in a dual rf excitation plasma sputtering process at two different values of relative ion flux (n_i indicates the normalized ion flux, the number of bombarding Ar ions per Ta atom deposited) and (b) resistivity and % α Ta as a function of argon ion flux at an ion energy of 10 eV . The data are from films deposited on SiO ₂ substrates.....	8
1.3	“Window” for α Ta growth in Ar ion flux and energy for sputter deposited films on SiO ₂ substrates	10
1.4	As-deposited stress as a function of deposition pressure in β Ta films deposited on thermally oxidized silicon wafers	12
1.5	As-deposited stress as a function of substrate bias in tantalum films sputter-deposited onto silicon substrates	13
1.6	Increase in compressive stress of an unpassivated β Ta film with thermal cycling in a helium atmosphere with a small amount of oxygen contamination	17
1.7	AES depth profile of a Ta film before and after thermal cycling seven times to 400°C in a helium atmosphere with a small amount of oxygen contamination	18
1.8	Stress as a function of temperature during β to α phase transformation in a 100 nm sputtered Ta film	20
2.1	Schematic diagram of the UHV system used for deposition and thermal cycling of the tantalum films investigated in this thesis.....	36
2.2	Schematic diagram of the 2-circle θ - θ diffractometer.....	41
2.3	Schematic diagram of a typical EBSD setup	44
2.4	Comparison of EBSD maps showing (a) raw and (b) noise-reduced data...	47

3.1	(a) Thermomechanical behavior of a 180 nm Ta film cycled repeatedly to 400°C in an atmosphere containing a small, but undetermined amount of oxygen, after Cabral <i>et al.</i> . (b) Thermomechanical behavior of a 100 nm Ta film thermally cycled to 850°C, after Clevenger <i>et al.</i> . X-ray analysis showed the film to be β phase as-deposited and α phase after cycling.....	54
3.2	Thermomechanical behavior of 350 nm Ta films cycled to 335°, 355°, 450°, and 600°C deposited and cycled in a deposition system with $< 2 \times 10^{-9}$ Torr base pressure. The stress jump is associated with the β - α phase transformation and occurs at much lower temperatures than in previous reports based on oxygen-containing films (<i>e.g.</i> Fig. 3.1b).....	60
3.3	Theta-theta x-ray scans of 350 nm Ta films (a) as-deposited, and after thermal cycling to (b) 335°C, (c) 355°C, (d) 450°C, and (e) 600°C in ultra high vacuum. The as-deposited film shows a strong (002) β phase texture. The films show a gradual transformation from β to α with increasing cycling temperature. The film cycled to 600°C has completely phase transformed.....	62
3.4	Plot of the x-ray peak volume ratio, $V_{\text{cycled}}/V_{\text{as-dep}}$, of the (002) β peak after thermally cycling to various temperatures. This ratio gives a quantitative estimate of the volume fraction of β phase remaining. The temperature range over which the volume fraction of β decreases coincides with the large increase in stress shown in Figure 3.2.....	63
3.5	Stress-temperature behavior of Ta films deposited in partial pressures of oxygen ranging from 1.7×10^{-6} Torr to 1.5×10^{-5} Torr. The shift in the stress jump to higher temperatures with increasing oxygen pressure arises from solute drag on α/β phase boundaries. At the highest oxygen content, no jump occurs when cycling the film between room temperature and 700°C.....	71
3.6	Change in activation energy for phase boundary motion normalized to that of an oxygen-free film as a function of calculated as-deposited oxygen content. The curve is a line to guide the eye and should not be interpreted as a functional form.....	75
3.7	Stress-temperature behavior of Ta films exposed to various amounts of oxygen between deposition and thermal cycling to form an oxide layer. The phase transformation is arrested when the oxygen from the oxide layer diffuses into the film. While the total stress change remains essentially constant, higher temperatures are needed to complete the transformation as the film is exposed to greater amounts of oxygen.....	79

3.8	Stress-temperature behavior of a ~ 350 nm Ta film thermally cycled in an atmosphere containing ~ 10 ⁻⁵ Torr oxygen. As temperature increases, there is a competition between oxygen incorporation (leads to higher activation energies for boundary motion, inhibiting the phase transformation and causing increased compressive stresses) and the increase in thermal energy (allows the β - α phase transformation to progress, causing increased tensile stresses). Note the shape of the curve is similar to that reported by Clevenger <i>et al.</i> (Fig. 3.1b).....	82
4.1	Images taken from GADDS x-ray scans of a 400 nm tantalum film (a) as-deposited in the β phase and (b) after scanning in the DSC. A comparison of the (002) β peak volumes was used to determine how much of the film transformed during DSC experiments.....	94
4.2	DSC scan of a tantalum film deposited in the metastable β phase. The peak indicates an exothermic reaction consistent with β - α phase transformation, and its area gives the energy released during the reaction (driving force of the transformation).....	95
4.3	Activation energies for the β - α phase transformation as a function of oxygen content in the film. The activation energies that were estimated in Chapter 3 based on the change in strain energy during the transformation are displayed for comparison.....	97
5.1	Stress vs. temperature data for (a) a 390 nm tantalum film deposited in the β phase on an ~ 0.5 mm (100) silicon substrate and (b) a 280 nm tantalum film deposited in the β phase on an ~ 0.5 mm fused silica substrate. The large increase in stress at ~ 300°C during heating is due to densification of the film during the β - α phase transformation . Linear fits to the data below 200°C are shown by the solid lines and represent thermoelastic slopes for the β phase (heating, before the transformation) and the α phase (cooling, after the transformation).....	102
6.1	Stress-temperature plot of a 400 nm tantalum film deposited in the metastable β phase thermally cycled between room temperature and 700°C. The film transforms to the stable α phase between 300° and 375°C, accompanied by a large change in stress in the tensile direction.....	110
6.2	(a) EBSD map showing the local out-of-plane crystal orientations of a tantalum film deposited in the α phase. The film has a strong (110) out-of-plane orientation, as can be seen from (b) the (110) pole figure and (c) the out-of-plane inverse pole figure, and a grain size on the order of the film thickness. Note the well-defined grains enclosed by high angle grain boundaries.....	114

6.3	EBSD map showing the local out-of-plane crystal orientations of a tantalum film deposited in the β phase and transformed to the α phase during thermal cycling. The crystal orientation gradually changes with position in much of the film. Few high angle ($> 8^\circ$, shown by black lines) or low angle grain boundaries (between 2° and 8° , shown by gray lines) are present, and many are discontinuous. The red line lies in the middle of a region that visibly demonstrates a large, gradual change in crystal orientation seen commonly in these films.....	115
6.4	(001), (110), and (111) out-of-plane pole figures of a phase-transformed tantalum film and an out-of-plane inverse pole figure of the same film. Note the diffuse nature of the PFs and the peak in the IPF, indicating a film that is textured, but not sharply.....	117
6.5	Plot depicting the change in misorientation angle with position along the red line shown in Figure 6.3 (relative to the bottom endpoint). Note that the linear trend indicates a constant rotation of $\sim 4^\circ/\mu\text{m}$ over a distance of more than seven micrometers.....	118
6.6	Rotation pole figures in crystal coordinates showing the distribution of pixel-to-pixel rotations about crystal axes in a phase-transformed Ta film for (a) $0\text{--}0.2^\circ$, (b) $0.2\text{--}0.45^\circ$, and (c) $0.45\text{--}2^\circ$ misorientations. The peak around the [211] direction (denoted by the star) is consistent with the rotation generated by an array of aligned edge dislocations on a primary slip system.....	122
6.7	Rotation pole figures in sample coordinates showing the distribution of pixel-to-pixel axes of rotation relative to the sample coordinate system for (a) $0\text{--}0.2^\circ$, (b) $0.2\text{--}0.45^\circ$, and (c) $0.45\text{--}2^\circ$ misorientations. The intensity near the edge of the sample RPF indicates that the rotation axes are primarily in or near the plane of the film.....	123
6.8	Comparison of misorientation in crystal reference coordinates with misorientation in sample reference coordinates with position along the red line shown in Figure 6.3. Note that while the misorientation crystal coordinates varies linearly with position over the entire distance, the misorientation in sample coordinates has distinct changes in slope characteristic of a change in the dominant axis of rotation.....	126
7.1	(a) EBSD map of a 300 nm oxygen-free tantalum film deposited in the β phase and transformed to the α phase during thermal cycling. The oxygen-free phase-transformed film has a discontinuous grain boundary structure, and continuous gradients in crystal orientation within individual grains. (b) Stress-temperature plot of tantalum films deposited with varying partial pressures of oxygen. Increasing oxygen content inhibits the phase transformation, requiring higher temperatures to initiate and to reach completion.....	133
7.2	EBSD maps of phase-transformed tantalum films deposited with (a) $2.5 \times$	

	10 ⁻⁶ , (b) 4.6 × 10 ⁻⁶ , and (c) 8.1 × 10 ⁻⁶ Torr of oxygen.....	136
7.3	Plot of average grain size with oxygen content. Error bars indicate the standard deviation. The grain size increases with increasing oxygen.....	138
7.4	Histograms showing the variation in grain boundary angles with increasing oxygen partial pressure during deposition. As the oxygen content increases, high-angle grain boundaries are gradually replaced with a greater percentage of low-angle boundaries.....	139
7.5	Comparison of the distribution of misorientations between neighboring pixels with increasing oxygen partial pressure during deposition. While all films show a peak at ~ 0.4°/pixel, note appearance of a second peak at ~ 0.1°/pixel in the film deposited in 8.1 × 10 ⁻⁶ Torr of oxygen.....	140
7.6	Inverse pole figures depicting the out-of-plane crystal orientation distribution in phase-transformed tantalum films deposited with (a) no oxygen, (b) 2.5 × 10 ⁻⁶ , (c) 4.6 × 10 ⁻⁶ , and (d) 8.1 × 10 ⁻⁶ Torr of oxygen. All IPFs are normalized to their mean intensity, with color scaling as shown.....	141
7.7	Rotation pole figures showing distributions of axes of rotation in an oxygen-free film in crystal and sample coordinates for (a) and (d) 0-0.2°, (b) and (e) 0.2-0.45°, and (c) and (f) 0.45-2° misorientations.....	143
7.8	Rotation pole figures showing distributions of axes of rotation in the film deposited with 8.1 × 10 ⁻⁶ Torr of oxygen in crystal and sample coordinates for (a) and (d) 0-0.1°, (b) and (e) 0.1-0.35°, and (c) and (f) 0.35-2° misorientations.....	144

List of tables

- 3.1 Summary of data for films with oxygen incorporated during deposition: oxygen partial pressure during deposition, estimated oxygen concentration in the film, C_{ox} , estimated lower bound of activation energy for phase boundary motion, ΔG_a , and additional tensile stress due to oxygen leaving the film during the phase transformation..... 70
- 5.1 Comparison of thermoelastic slopes of β and α phase tantalum films deposited on (100) silicon and fused silica substrates and the calculated CTE and biaxial elastic modulus of each phase. Values of the CTE and the biaxial elastic modulus (for both (100) and (111) crystal orientations) of bulk bcc tantalum are given for comparison..... 103

Chapter 1

Introduction

1.1 Motivation

Many devices commonly used by people throughout the world rely on thin films, ranging in thickness from a few nanometers to a few micrometers, deposited on rigid substrates. Thin films have properties that can often differ greatly from those of similar bulk materials and depend heavily on preparation and processing conditions and the resultant microstructure. These materials are often chosen on the basis of their electronic, magnetic, or optical properties. However, the devices in which they operate must be reliable, and the materials chosen must provide adequate resistance to mechanical failure. Thus, relationships between microstructure and mechanical properties of thin films are crucial to the stability of these micro- and nanofabricated devices.

This thesis focuses on the thermomechanical behavior and microstructure of tantalum thin films. Tantalum films are used in a variety of microelectronic applications, ranging from diffusion barriers between copper metallizations and silicon substrates to thin film resistors and capacitors to masks for x-ray optics. One aspect of tantalum films that has allowed them to be used in such a wide range of applications is that they can be deposited in two different crystal structures, the stable bcc α phase and the metastable tetragonal β phase, that have very different mechanical and electrical properties. However, it can be difficult to deposit a film in the desired phase or, in the case of β phase films, to keep it there during device operation. In addition, very large stresses can develop in tantalum films when heated above a few hundred degrees Celsius, due to either a transformation of the crystal structure from β to α or from the incorporation

of oxygen into the film. Such stresses may lead to device failure by film cracking or delamination. The relationships between film preparation and processing, microstructure, and stress must be understood in order to better design films that not only meet their functional requirements when prepared, but continue to maintain their integrity over the specified lifetime of a device.

1.2 Structure of this thesis

This thesis is organized into eight chapters. This chapter provides background information on tantalum thin films, focusing on previous studies related to the work detailed in this thesis, as well as a general overview of the kinetics of phase transformations. Chapter 2 provides supplemental details of the experimental techniques described in Chapters 3-7. Chapter 3 addresses the thermomechanical behavior of tantalum films during the β - α phase transformation and the effects of various methods of oxygen incorporation on stress and microstructure evolution. This chapter, entitled “Effect of oxygen on the thermomechanical behavior of tantalum thin films during the β - α phase transformation,” has been published in the Journal of Applied Physics. Chapter 4 is an addendum to Chapter 3 in which the driving force and activation energy of the phase transformation are more accurately determined. Chapter 5 addresses the physical properties of the β phase in a short paper entitled “Coefficient of thermal expansion and biaxial elastic modulus of β phase tantalum thin films” that is being prepared for journal submission. Chapter 6 provides a detailed description of the microstructure of phase-transformed α Ta films from EBSD data and compares the very unusual microstructure that develops to that of a similar film deposited in the α phase. The results of this analysis have been used to suggest a dislocation structure that must occur in the phase-transformed film in order for the observed microstructure to exist and how this structure might develop. In Chapter 7, we show how increasing oxygen

content affects the microstructure of these phase-transformed films and describes a mechanism by which this may occur. Both Chapters 6 and 7 are in preparation for journal submission. Finally, in Chapter 8, the overall conclusions of this work are summarized and suggestions for further research are presented.

1.3 Tantalum thin films

Tantalum films are used extensively in a number of microelectronic and x-ray based applications. Tantalum has a very high melting temperature (3269 K), and is a good x-ray absorber. It forms a thin oxide layer (~ 2 nm thick) when exposed to an oxygen-containing atmosphere [1, 2] that allows the material, which is otherwise very reactive, to be nearly chemically inert at low temperatures.

Sputter-deposited Ta thin films can be made in two different crystal phases that have very different properties. The crystal structure nucleated depends on both the substrate and deposition conditions. The bcc α phase is the same as formed in bulk tantalum. It has a low resistivity (15-60 $\mu\Omega$ cm), is very ductile, and is nearly immiscible in copper, making it an excellent material for use in thin film capacitors [3-5] and in interconnects as a diffusion barrier between copper and silicon [6-8]. Tantalum can also be deposited in a metastable structure with tetragonal symmetry known as the β phase. This phase has a much higher resistivity (170-210 $\mu\Omega$ cm) [5, 9], is brittle compared to the α phase [10], and has been found to be much more susceptible to reactive ion etching [11], making these films considerably easier to pattern. As such, β -Ta films have thus found uses as masks for x-ray lithography [12], as an interface between the heater element and the ink in thermal ink-jet devices [13], and as thin film resistors in micro- and nanofabricated devices [3-5].

For many applications, it is important that the Ta thin film stress behavior during thermal cycling be well understood. In addition to differential thermal expansion, irre-

versible microstructural changes often occur during thermal cycling that can generate significant changes in stress. In general, the thermomechanical behavior of thin metal films on substrates is studied by subjecting samples to thermal cycles and determining stresses either using the substrate curvature method, in which stresses are deduced from changes in the curvature of the film/substrate package, or from strains determined using x-ray measurements. In such experiments, there are often strong effects on thermomechanical behavior arising from small changes in impurity content not only in tantalum, but in many other materials as well [14].

This literature review will focus on the thermomechanical behavior and microstructure evolution of Ta films deposited in the β phase, with a brief discussion on substrates and deposition conditions that lead to preferential growth of either the α or β phase. The focus will be on the factors that influence stresses in these films, especially those occurring during thermal cycling.

1.3.1 Deposition and crystal structure

The β phase was initially discovered in 1965 by Read and Altman [15], who reported the crystal structure as having a sixteen-atom tetragonal unit cell with a theoretical density of 16.9 g/cm³. Further x-ray analysis by Moseley and Seabrook [16] suggested a thirty-atom unit cell with a density of 16.33 g/cm³, and further specified the crystal symmetry to that of the $P4_2/mnm$ space group, isomorphous with β uranium. It is this crystal structure that has been most commonly referenced in the literature. However, Arakcheeva *et al.* [17] have recently argued that a similar thirty-atom unit cell, but with $P\bar{4}2_1m$ symmetry and a density of 16.28 g/cm³, is the correct structure. These structures are nearly identical when viewed from an [001] zone axis (shown in Figure 1.1) and are differentiated only by a slight lateral shift in the atoms forming the doubly

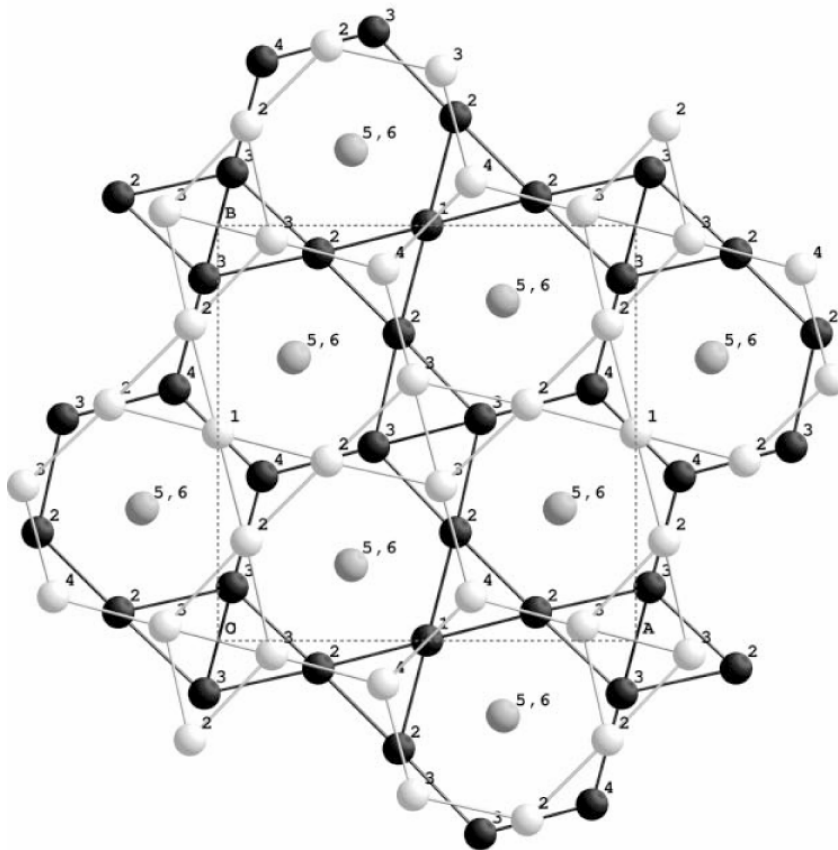


Figure 1.1: Crystal structure β tantalum (viewed down the c -axis) as described by Arakcheeva *et al* [17]. The black and white circles indicate two consecutive levels of the primary atomic nets separated by $0.5c$ (host sublattice). The gray atoms indicate the channel atoms of the guest sublattices, located midway between the primary nets. The numbers indicate crystallographically equivalent positions within the unit cell.

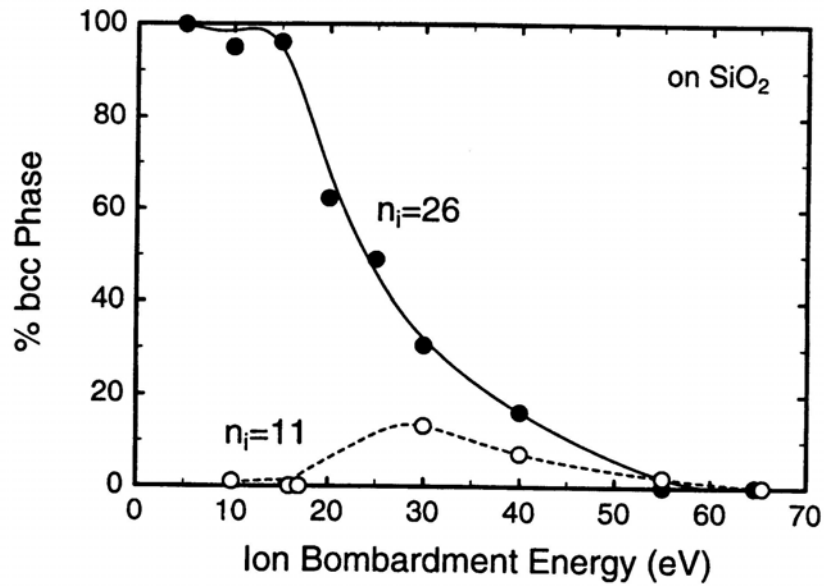
occupied columns in the model proposed by Arakcheeva *et al.* [18]. Despite its use in a number of devices, the physical properties of this structure remained largely unknown prior to the work detailed in Chapter 5 of this thesis. In addition, as the β phase is not an equilibrium polymorph of tantalum, it is not clear why this structure is able to form, although Jiang *et al.* have suggested that the β phase may have a lower energy crystal structure for very small clusters of tantalum atoms (less than ~ 100 atoms) [19]. Similar metastable structures have also been observed in other bcc films, such as tungsten [20] and chromium [21], but these phases do not appear to be as stable as β tantalum and have been studied very little.

While the majority of studies on tantalum have focused on sputter-deposited films, tantalum can also be deposited using electron-beam evaporation. In evaporated tantalum films, another structural phase can be formed in addition to the α and β phases. A pure fcc structure has been found in very thin films (up to approximately 7-8 nm thick), with the bcc phase beginning to form with increasing thickness [22]. Thicker films (up to 320 nm) have been shown to have up to 50% fcc structure present, as identified by x-ray data [22]. Neal and Bombin [22] determined that in order for the fcc phase to form, the pressure during evaporation had to be less than 10^{-7} Torr, the deposition temperature less than 770 K, and the film thickness small (for pure fcc phase). While all three phases have been identified in evaporated films [22-24], little work has been done in identifying the deposition conditions under which each of these phases will be formed, and no industrial applications of the fcc phase have been reported.

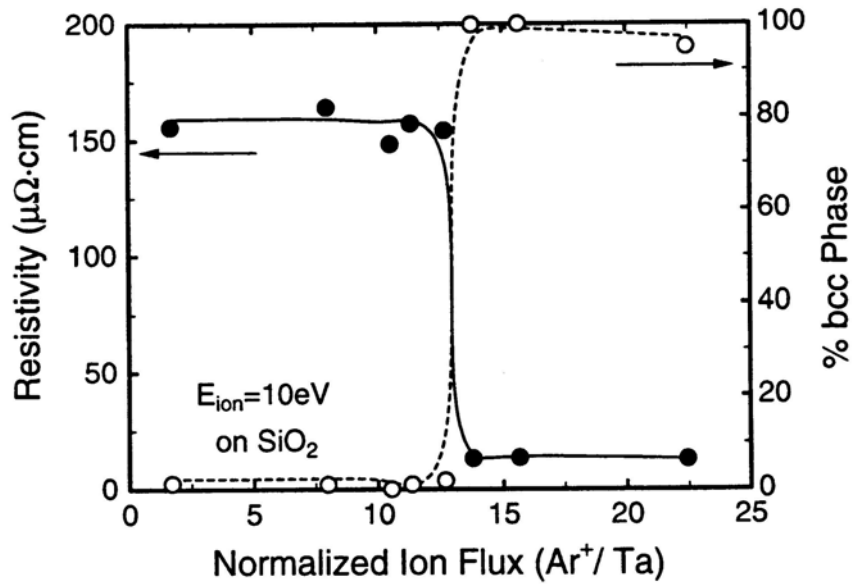
The crystal structure of sputter-deposited films depends on several factors, the most important of which are the substrate and the ion bombardment conditions during deposition. Feinstein and Huttemann [25] reported three classes of substrates: (I) oxides, or substrates that readily form surface oxides in air at room temperature (glass,

Ta₂O₅, quartz, sapphire, Cu, Ni, Si, and SiO₂) nucleate the β phase; (II) substances that do not readily form oxides (Au, Pt, Rh, Be, and W) nucleate bcc tantalum; and (III) substances which do not rapidly form surface oxides in air at room temperature but that may be oxidized at higher temperatures (Mo, Ta₂N, Si₃N₄), which form the α phase when freshly prepared and the β phase when oxidized. This suggests that there is a strong heteroepitaxial crystallographic effect on the phase nucleated. The deposition conditions in the Feinstein and Huttemann study were not greatly varied, and recently, several notable exceptions have been found to these categories. Aluminum, which would be classified as a group I substrate material, has been shown to generally nucleate bcc tantalum [26], and Si and SiO₂ substrates can nucleate either the α or β phase, depending on the ion bombardment conditions [27, 28]. More recently, Hieber and Lautenbacher [29] proposed that the formation of the β phase depends on the ability of the depositing tantalum atoms to react with the substrate and form a thin interlayer upon which the β phase can grow.

The sputtering conditions, primarily the ion energy and flux of the bombarding species, can have a large effect on the crystal structure nucleated. The substrate temperature, however, appears to have little effect on the structure deposited until very high temperatures are reached ($\sim 600^\circ\text{C}$) where films that would be deposited in the β phase at lower temperatures instead form the bcc structure [30, 31]. Ion energy and flux can be controlled by either changing the substrate bias in the sputtering process [28], which affects both ion energy and flux, or by using dual rf excitation plasma process equipment, which can independently control bombardment energy, ion flux, and film growth rate [27]. Ino *et al.* have shown that the percentage of bcc phase in a film (as measured by x-ray texture analysis) is maximized at low ion bombardment energies and high flux, as can be seen in Figure 1.2 [27]. On Si and SiO₂ substrates, low flux values will produce films that are almost entirely β Ta, regardless of the



(a)



(b)

Figure 1.2: (a) Fraction of α Ta as a function of argon ion energy in a dual rf excitation plasma sputtering process at two different values of relative ion flux (n_i indicates the normalized ion flux, the number of bombarding Ar ions per Ta atom deposited) and (b) resistivity and % α Ta as a function of argon ion flux at an ion energy of 10 eV [27]. The data are from films deposited on SiO_2 substrates.

bombardment energy, while high energy bombardment will always produce the β phase, regardless of the flux. The majority of bombardment conditions will cause formation of the β phase, but there is a narrow region of low-energy, high-flux bombardment that will cause α Ta to nucleate [27] (see Figure 1.3). This result is very important for the large number of microelectronics applications where a particular crystal structure is desired for its resistivity or patternability properties.

1.3.2 Dependence of stress on deposition conditions in β Ta

The stress dependence on deposition conditions is important for films used in many types of devices. As tantalum films in devices operated at low temperatures are unlikely to experience significant structural changes or stress relaxation at or near room temperature due to the very low homologous temperatures and slow self-diffusivity, and the majority of the stress in these films will be due to the deposition process. In addition, the stresses in films exposed to higher temperatures where structural changes do occur can be strongly affected by deposition stresses.

Little work has been done to characterize stress levels in evaporated films. In the absence of external ion bombardment, evaporated Ta films are generally in a state of tensile stress [24]. This can be explained by the non-equilibrium growth conditions inherent in evaporated metal films when substrate temperatures are low [32]. As film atoms are deposited, there is typically not enough thermal energy for the atoms to reach equilibrium positions, and thus they are “frozen” into non-equilibrium positions by subsequently deposited atoms. Tensile stresses will form as the film is constrained from shrinking to a more energetically favorable configuration due to its interaction with the substrate.

Two main factors influence the as-deposited stress in sputtered tantalum films: sputtering pressure and substrate bias voltage. Of secondary importance are the sput-

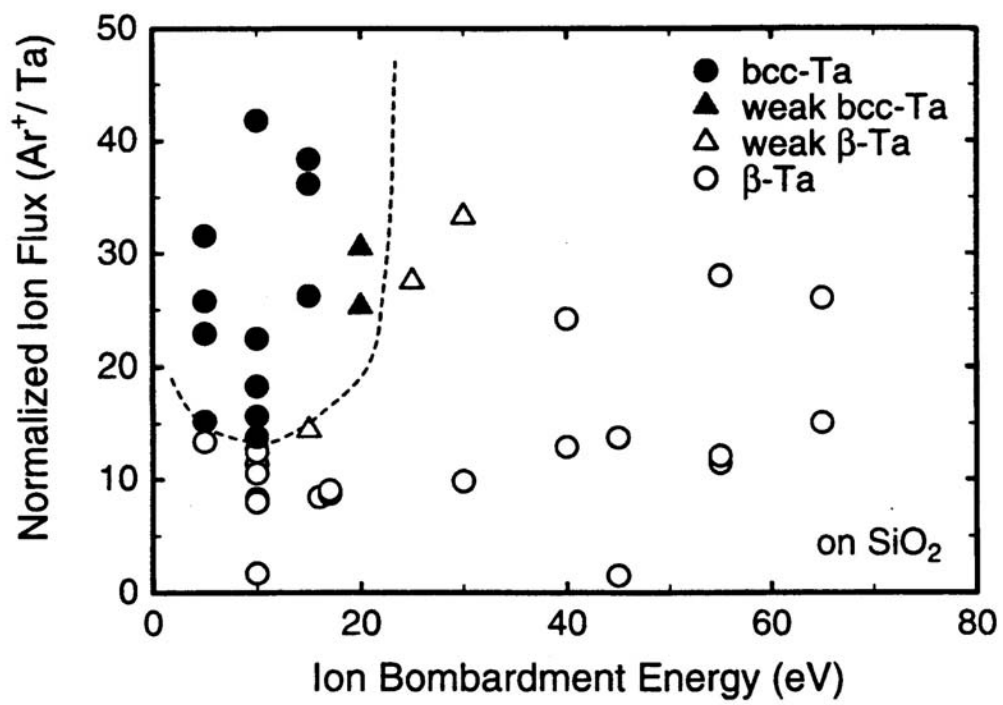


Figure 1.3: “Window” for α Ta growth in Ar ion flux and energy for sputter deposited films on SiO_2 substrates [27].

tering gas used, substrate temperature, sputtering power, and the geometry of the system. As seen in Figure 1.4, lower sputtering pressures during tantalum film deposition (at a constant target-to-substrate distance, substrate bias, film thickness, and low substrate temperature) result in more compressive stresses, while higher sputtering pressures yield more tensile stresses [24]. This is consistent with trends found for sputter deposition of many other materials as well [32]. Tensile stresses occur at high sputtering pressures as the film sees very little bombardment. Thus, depositing adatoms do not have enough energy to move from where they land on the substrate, and the film forms in a low-density structure similar to that of an evaporated film [32]. As the sputtering pressure is decreased, the ion bombardment becomes more energetic and gives depositing adatoms enough energy to reach local equilibrium positions, resulting in a near-zero stress state. Compressive stresses are reached at even lower pressures when the bombarding species have enough energy to embed themselves into interstitial sites below the film surface, causing an expansion of the lattice and an increase in the equilibrium in-plane dimensions of the film relative to the substrate [32].

Figure 1.5 shows how the stress in as-deposited tantalum films varies with substrate bias, with a peak in the compressive stress between -100 and -200 V [28]. The substrate bias also has a significant effect on the crystal structure, with films deposited on silicon substrates forming α Ta with little or no bias applied, and becoming nearly all β phase with -100 V or greater applied voltages. The increase in substrate bias increases the average energy of the bombarding species, so that more atoms are implanted and a higher compressive stress is reached up to about -200 V. It has been theorized that plastic flow begins at this point for Ta films and lowers the stress levels as the bias voltage increases further [33].

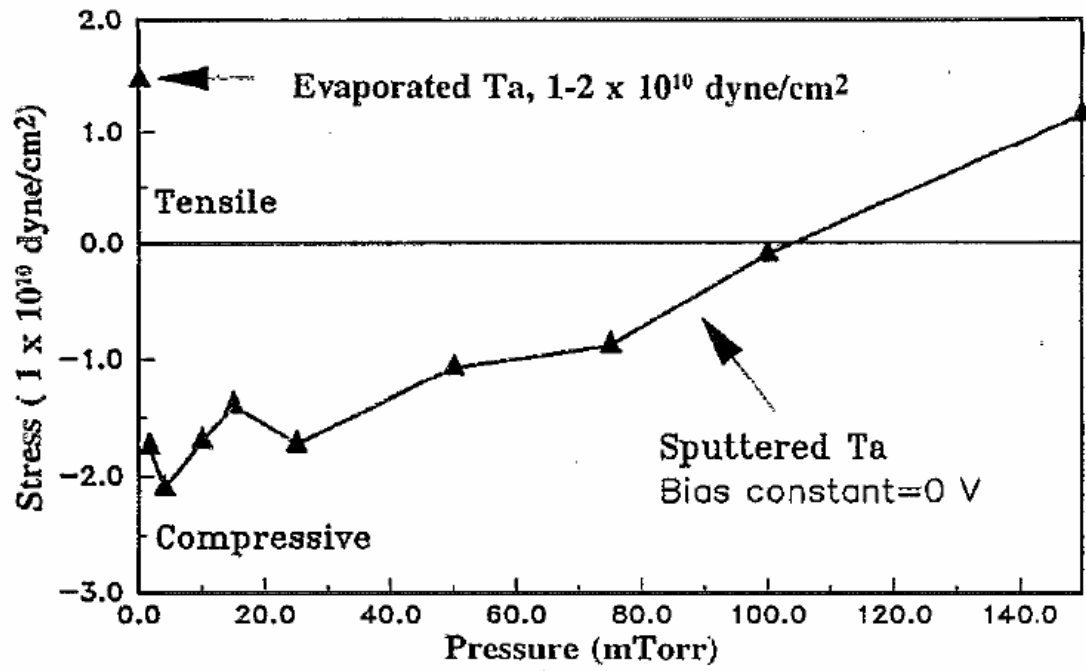


Figure 1.4: As-deposited stress as a function of deposition pressure in β Ta films deposited on thermally oxidized silicon wafers [24].

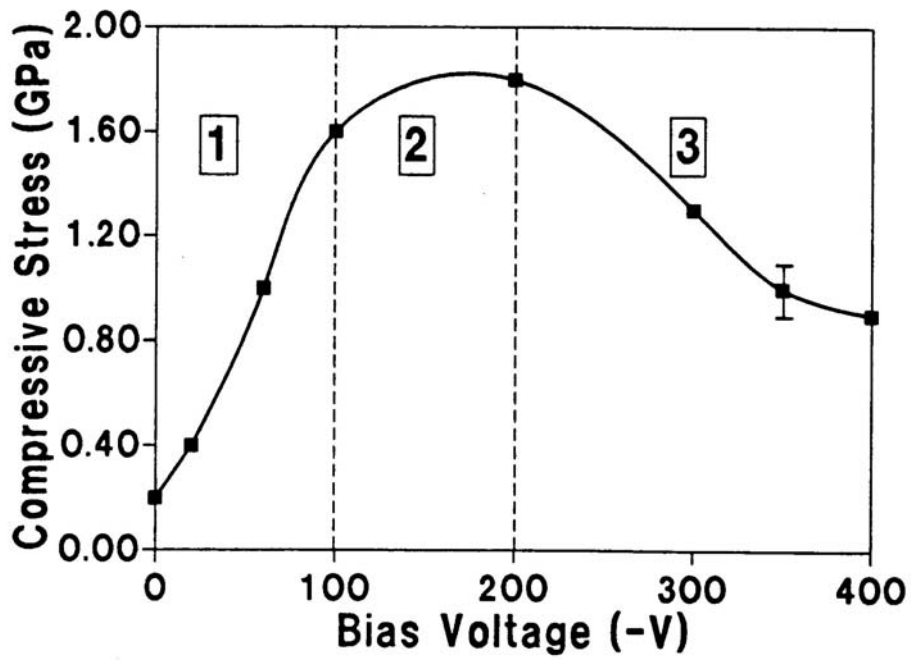


Figure 1.5: As-deposited stress as a function of substrate bias in tantalum films sputter-deposited onto silicon substrates [28].

1.3.3 Thermal cycling and microstructure evolution

A change in temperature of a film/substrate system will cause a change in stress in the film if the coefficients of thermal expansion (CTE) of the two materials are different. This is used in Chapter 5 to determine some of the physical properties of β phase tantalum films. In the case of a tantalum film on a silicon substrate, tantalum has a significantly higher CTE ($6.3 \times 10^{-6}/^{\circ}\text{C}$ for bulk bcc tantalum at room temperature) [34] than silicon ($2.6 \times 10^{-6}/^{\circ}\text{C}$ for (100) single crystals at room temperature) [35] and thus, an unconstrained film would expand more quickly than the substrate as the temperature is increased. A strain is induced in the film as it is constrained to adopt the in-plane dimensions of the thicker substrate. The in-plane strain, $\varepsilon_{thermal}$, can be determined with knowledge of the CTE of the film, α_f , and substrate, α_s , as a function of temperature according to:

$$\varepsilon_{thermal} = -\int_{T_0}^T \{\alpha_f(T) - \alpha_s(T)\} dT. \quad (1.1)$$

Approximating the CTE values as constants over the temperature range of interest, this equation can be simplified to:

$$\varepsilon_{thermal} = -(\alpha_f - \alpha_s)(T - T_0) = -\Delta\alpha\Delta T \quad (1.2)$$

where ΔT is the change in temperature. Assuming an equal biaxial stress state and isotropic elastic deformation, the in-plane change in stress in the film, $\Delta\sigma$, is given by:

$$\Delta\sigma = Y_f \varepsilon_{thermal} \quad (1.3)$$

where Y_f is the biaxial elastic modulus of the film.

In addition to the changes in stress and strain from differential thermal expansion, thermal cycling can also have various effects on the crystal structure, morphology, and composition, all of which can affect the resultant stress in a film. Some of the more prominent effects on stresses in films can result from grain growth, oxidation, and crystal texture or phase changes that may occur at elevated temperatures. These processes are relevant primarily to the discussion of stress evolution in Chapter 3 but also

to the microstructural studies in Chapters 6 and 7 and will be discussed in the following sections.

1.3.3.1 Grain growth

Very little has been reported regarding grain growth during annealing in tantalum films, with no numerical data available on grain sizes after annealing. As-deposited grains are generally columnar, with diameters of around 20–60 nm, depending on the film thickness and deposition conditions [26, 27, 36]. It has been reported, however, that grains that remain (002) β Ta show “almost no change” in grain size during annealing to 500°C [26], while grains that transform into α phase show a dramatic increase in grain size, towards the value of the Ta layer thickness [26]. Grain growth causes a densification of the film from the reduction of free volume associated with grain boundaries which leads to an increase in stress in the tensile direction, according to the equation:

$$\Delta\sigma = -Y_f\delta\left(\frac{1}{d_1} - \frac{1}{d_0}\right) \quad (1.4)$$

where δ is the excess free volume per unit area of the grain boundary (typically ~ 1 Å), and d_0 and d_1 are the initial and final grain sizes, respectively [37]. This equation applies to cases where the film is isotropic in plane and the biaxial elastic modulus remains constant during grain growth. However, it appears that for temperatures below $\sim 750^\circ\text{C}$, grain growth in tantalum films does not occur independently of the phase transformation.

1.3.3.2 Oxygen incorporation

In general, oxygen will begin to diffuse into tantalum films when heated to temperatures above 250–300°C in oxygen-containing atmospheres [5, 38-41], with kinetics as

described by Lugomer *et al* [41]. At these temperatures, oxygen is absorbed even with only minimal partial pressures present [36, 42]. Oxygen diffuses into a tantalum film during annealing rather than forming only a surface oxide, and it has been observed that a thin layer of tantalum oxide will be absorbed into a thicker tantalum layer when annealed to temperatures above $\sim 375^{\circ}\text{C}$ under high vacuum conditions [8, 43].

Some studies [13, 44, 45] have reported large changes in stress in the compressive direction in films cycled between room temperature and $400\text{--}450^{\circ}\text{C}$. In these studies, stresses were determined from changes in substrate curvature measured in inert gas purged but nonetheless oxygen-containing atmospheres, and the stress changes were attributed to the incorporation of oxygen into the film. At temperatures above $\sim 300^{\circ}\text{C}$, compressive stresses were observed to increase with each thermal cycle, reaching a magnitude of ~ -6 GPa [44] (Figure 1.6). Cabral *et al.* [44] determined that while the crystal structure remained that of the β phase, Auger electron spectroscopy (AES) depth profiling indicated that more than 10 at.% of oxygen was incorporated uniformly through the thickness of the film (Figure 1.7). In a different experiment by French and Bilello in which similar films were heated to 600°C in air, the films completely oxidized to form Ta_2O_5 , and compressive stresses of up to -4 GPa were observed before the films started to blister in order to relieve stress [46].

1.3.3.3 Phase transformation

The transformation from β to α has been studied in a number of systems with widely varying results. Depending on the substrate, annealing atmosphere, and deposition conditions, the transformation has been observed beginning at temperatures as low as $200\text{--}400^{\circ}\text{C}$ [26] in some systems and not completing until temperatures of 800°C or higher in others [47]. The annealing atmosphere has an enormous impact, as even small amounts of oxygen in the atmosphere have been shown to inhibit the phase

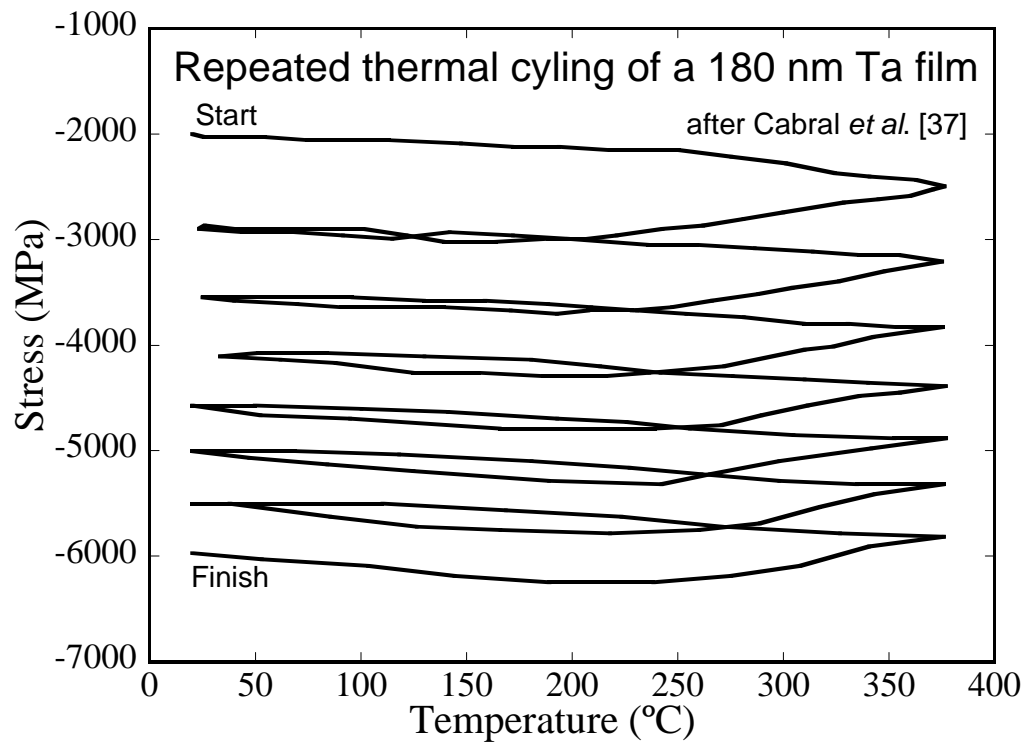


Figure 1.6: Increase in compressive stress of an unpassivated β Ta film with thermal cycling in a helium atmosphere with a small amount of oxygen contamination [44].

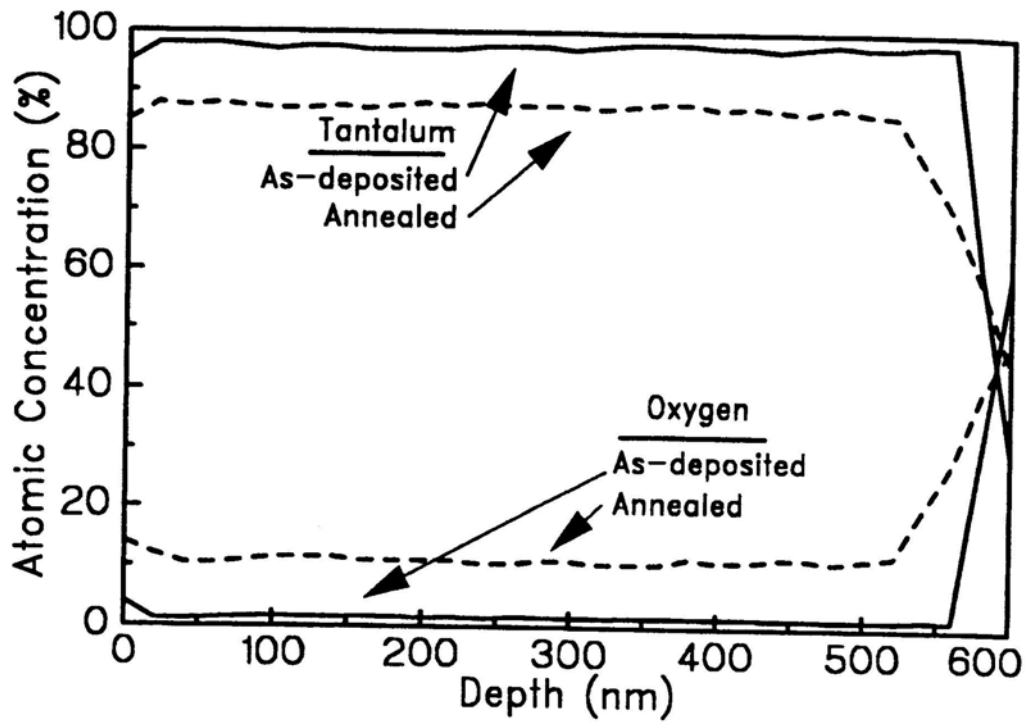


Figure 1.7: AES depth profile of a Ta film before and after thermal cycling seven times to 400°C in a helium atmosphere with a small amount of oxygen contamination [44].

transformation [36, 42]. To the author’s knowledge, until the work detailed later in this thesis, no annealing studies had been performed in which atmospheric conditions were used that would effectively prevent oxidation (the lowest base pressure previously recorded had been 10^{-6} Torr) [47].

Clevenger *et al.* [24] reported that the phase transformation is generally accompanied by a large change in stress in the tensile direction (measured by changes in substrate curvature during annealing in an inert gas purged atmosphere), as shown in Figure 1.8. The data from this paper represent the only published results of the thermomechanical behavior of tantalum films during the β - α phase transformation prior to the work presented in this dissertation. While no x-ray data or other direct determination of crystal structure are shown in this paper, Clevenger *et al.* do show an abrupt decrease in the electrical resistivity of the film that is consistent with the change from β to α over the same temperature range as the increase in tensile stress and have stated that x-ray diffraction data were consistent with the phase transformation. Clevenger *et al.* [24] also report a “stress anomaly” in many of their films around 400°C, where the stress increased abruptly in the tensile direction but found no “significant structural changes” that correlated with it. These data and their interpretation are discussed further in Chapter 3.

1.4 Kinetics of solid-solid phase transformations

A phase transformation from one crystal structure to another can occur in a material when that transformation results in a decrease in the Gibbs free energy of the system, such as in the β - α phase transformation in Ta films. However, a reduction in free energy does not guarantee that such a transformation will take place. Typically, there is a significant energy barrier which must be overcome before a phase transformation can occur. This barrier can be overcome through the random thermal motion of the atoms

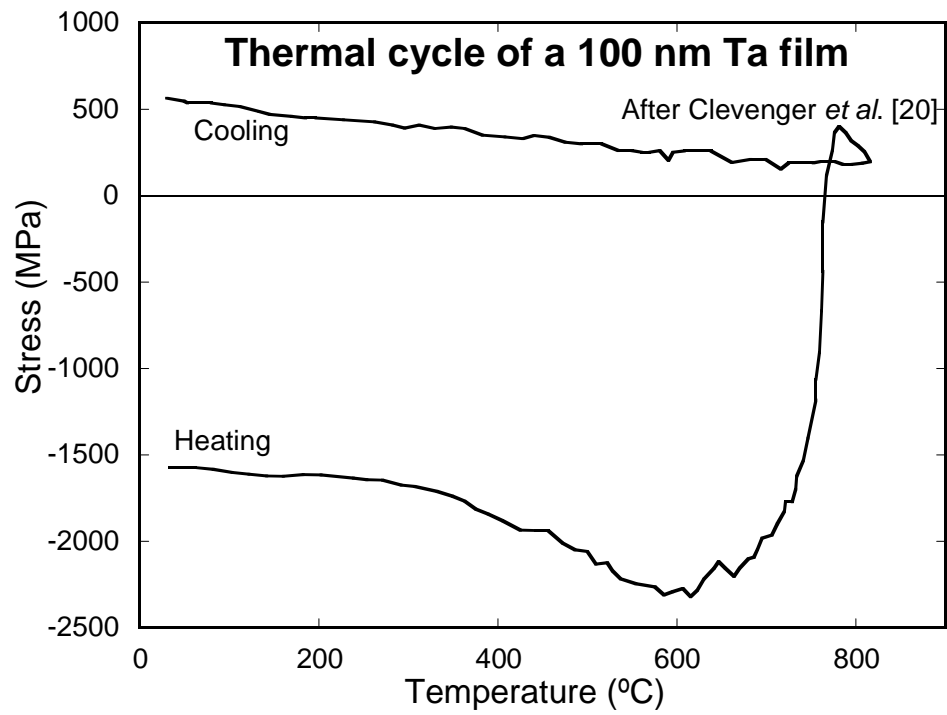


Figure 1.8: Stress as a function of temperature during β to α phase transformation in a 100 nm sputtered Ta film [24].

in the material by a process called thermal activation. The probability that any particular atom will have sufficient energy to pass over the activation barrier is given by $\exp(-\Delta G_a / kT)$, where ΔG_a is activation free energy barrier and k is Boltzmann's constant. Thus, the rate at which the transformation progresses will be proportional to this quantity. A number of other factors can also have an impact on the rate at which a phase transformation occurs. These will be detailed in the following sections and also serve as necessary background for the discussion in Chapter 3 of the mechanism of the β - α phase transformation in tantalum films and how oxygen inhibits it.

1.4.1 Diffusion

One of the most fundamental means by which a phase transformation can occur is through diffusion. Diffusion is critical for the initial formation of second phase nuclei in a solid and is the rate-limiting process in many phase transformations. In addition, the diffusion of impurity atoms into a film can have a large impact on its behavior. As the study of diffusion is much too large to be completely summarized here, this review will be limited to a brief overview of the atomic mechanism of diffusion and the calculation of the intrinsic diffusivity for different types of diffusion along the lines of those found in Shewmon [48] or Porter and Easterling [49].

As most studies of diffusion involve atoms diffusing in response to a concentration gradient, this discussion will begin in a similar manner. In the exchange of atoms between two adjacent atomic planes, a distance δ apart, the net flux of atoms jumping from plane 1 to plane 2, J , is given by:

$$J = \frac{1}{6}(n_1 - n_2)\Gamma \quad (1.5)$$

where Γ is the jump frequency and n_1 and n_2 be the numbers of diffusing atoms per unit area of the two planes of interest. The quantity $(n_1 - n_2)$ can be related to the concentration by observing that $n_1 / \delta = c_1$ and $n_2 / \delta = c_2$, where c_1 and c_2 are the con-

centrations per unit volume of diffusing atoms. Assuming the concentration changes slowly enough to be considered linear over such short distances,

$$c_1 - c_2 = -\delta \frac{\partial c}{\partial x} \quad (1.6)$$

where $\partial c / \partial x$ indicates the concentration gradient with position. Thus, the net flux can be written as:

$$J = -\frac{1}{6} \delta^2 \Gamma \frac{\partial c}{\partial x} \quad (1.7)$$

If we define a diffusion coefficient as:

$$D = \frac{1}{6} \delta^2 \Gamma \quad (1.8)$$

and substitute, we get:

$$J = -D \frac{\partial c}{\partial x} \quad (1.9)$$

which is known as Fick's first law of diffusion.

The diffusion coefficient is an important quantity in diffusion problems, as it allows for quick estimation of the net distance, r , an atom undergoing random walk diffusion will travel in a given amount of time, t , from:

$$r = 2.4\sqrt{Dt} \quad (1.10)$$

As D depends linearly on the jump frequency, Γ , it is useful to examine some of the factors that determine the magnitude of Γ .

We first consider interstitial diffusion, which generally occurs by smaller atoms diffusing through a parent crystal lattice of larger atoms along interstitial locations. In order for an interstitial atom to move from its current position to an adjacent interstitial position, the parent lattice must be briefly forced apart into higher energy positions. The work that must be done to accomplish this is known as the activation energy, ΔG_a . On average, the fraction of atoms with sufficient energy to accomplish such a jump is given by $\exp(-\Delta G_a / RT)$. Thus, if an interstitial atom is vibrating at a frequency ω , it makes ω attempts to jump per second, with the number that are successful

given by $\exp(-\Delta G_a / RT)$. For an atom surrounded by z sites in three-dimensional space to which it can jump, the jump frequency is given by:

$$\Gamma = z\omega \exp\left(-\frac{\Delta G_a}{RT}\right) \quad (1.11)$$

As the activation energy can be considered to be the sum of a large activation enthalpy, ΔH_a , and a small activation entropy term, $-T\Delta S_a$, the diffusion coefficient for interstitial diffusion, D_i , can be written as:

$$D_i = \left[\frac{1}{6} \delta^2 z\omega \exp\left(\frac{\Delta S_a}{R}\right) \right] \exp\left(-\frac{\Delta H_a}{RT}\right) \quad (1.12)$$

By grouping all of the temperature-independent terms into a single material constant, D_{io} , the diffusion coefficient can be expressed as a simple Arrhenius-type equation:

$$D_i = D_{io} \exp\left(-\frac{\Delta H_a}{RT}\right) \quad (1.13)$$

where

$$D_{io} = \frac{1}{6} \delta^2 z\omega \exp\left(\frac{\Delta S_a}{R}\right) \quad (1.14)$$

Thus, D and Γ both increase exponentially with temperature at a rate determined by the activation enthalpy. Often, ΔH_a is written as Q to more generically denote an activation barrier.

For self-diffusion in a pure metal, a similar situation occurs with the exception that a diffusing atom is no longer surrounded by available sites to which it can jump. Vacant sites in the lattice are necessary to accommodate diffusion in this case; if an atom has no vacancies neighboring it, it cannot jump to an adjacent site. This is manifested by an extra term in the jump frequency equation that indicates the probability of a lattice site being vacant, $\exp(-\Delta G_v/RT)$. Thus, the diffusion coefficient for self-diffusion, D_l , can be written as:

$$D_l = D_{lo} \exp\left(\frac{-(\Delta H_a + \Delta H_v)}{RT}\right) \quad (1.15)$$

where

$$D_{lo} = \frac{1}{6} \delta^2 z \omega \exp\left(\frac{\Delta S_a + \Delta S_v}{R}\right) \quad (1.16)$$

and ΔH_v and ΔS_v are the enthalpy and entropy of vacancy formation, respectively.

Note that here, $Q_l = \Delta H_a + \Delta H_v$. As can be deduced from the additional energy term, substitutional self-diffusion generally occurs at a significantly slower rate than interstitial diffusion.

In a similar manner, diffusion can occur at much faster rates when atoms are diffusing through regions with lower activation energies, such as along grain boundaries or free surfaces. It has been found experimentally that diffusion along grain boundaries and free surfaces can be described by:

$$D_b = D_{bo} \exp\left(-\frac{Q_b}{RT}\right) \quad (1.17)$$

or

$$D_s = D_{so} \exp\left(-\frac{Q_s}{RT}\right) \quad (1.18)$$

where D_b and D_s are the grain boundary and surface diffusivities, Q_b and Q_s are experimentally determined activation energies, and D_{bo} and D_{so} experimentally determined constants. For grain boundary diffusion in polycrystalline metals, D_{bo} is usually approximately equal to D_{lo} , while Q_b is about 0.4–0.5 Q_l [48, 50]. In general, $D_s > D_b > D_l$ at any given temperature.

While Fick's first law is based on the assumption that diffusion eventually stops and equilibrium is reached when concentrations are the same everywhere, this is usually not the case in real materials. As most materials contain defects such as grain boundaries, phase boundaries, dislocations, and lattice defects, some atoms (often impurities) can lower their free energy by migrating to these locations. Thus, at "equilibrium," the concentration of impurities may be much higher in the vicinity of these de-

fects than in the lattice. This segregation of atoms to grain boundaries, interfaces, and dislocations is of great technological significance and will be discussed in further detail in the following section.

1.4.2 Kinetics of boundary migration and solute drag

A phase or grain boundary will often move so as to reduce the total energy of a system. In a polycrystalline material, grains will grow to reduce the excess free energy associated with grain boundaries. A phase boundary will move as a metastable phase transforms into a more stable, lower energy structure. A boundary will move by the net flux of atoms from one side of the boundary to the other. Much like in diffusion, there is an activation energy barrier that must be overcome for an atom to make such a jump.

In order for an atom to jump across a boundary, it must acquire an activation energy of ΔG_a . If there are n atoms per unit area along the boundary, each vibrating with a frequency ω , the number of atoms per unit area per unit time able to successfully jump across the boundary will be given by $n\omega \exp(-\Delta G_a/RT)$. For a boundary in equilibrium, there are an equal number of atoms jumping in either direction. In order for a boundary to move, there must be a net flux of atoms in one direction. Consider two neighboring grains of similar composition and density. If there is a driving force, ΔG , for atoms to move from one grain to the other, the net flux of atoms across the boundary, J_{net} , will be given by

$$J_{net} = n\omega \exp\left(-\frac{\Delta G_a}{RT}\right) \left[1 - \exp\left(-\frac{\Delta G}{RT}\right)\right] \quad (1.19)$$

Thus, if $\Delta G = 0$, there will be no net flux and the boundary will be stable. If $\Delta G \neq 0$, there will be a net flux of atoms and the boundary will move. The speed of the boundary, v , can be related to the net flux by

$$J_{net} = \frac{v}{V_a} \quad (1.20)$$

where V_a is the atomic volume. Substituting into Equation 1.19 and assuming that the driving force is small compared to RT gives a boundary speed of

$$v = V_a n \omega \frac{\Delta G}{RT} \exp\left(-\frac{\Delta G_a}{RT}\right) \quad (1.21)$$

Thus, for a driving force that is small compared to RT , the boundary velocity scales linearly with ΔG .

As was mentioned previously, impurity atoms often segregate to low energy positions in grain or phase boundaries. This can have a substantial effect on the ability of such boundaries to move in response to a driving force. If the boundary starts to move, these impurity atoms will be left behind in higher energy locations. The boundary will thus exert an attractive force on these atoms causing them to preferentially diffuse in the direction of the moving boundary. These impurity atoms will, in turn, exert a force on the boundary, slowing its movement. If the boundary moves slowly enough, the impurities will move along with the boundary. This phenomenon is known as impurity drag or solute drag. A basic treatment of this effect after Lucke and Detert [51] is presented here; more detailed analyses can be found elsewhere [52-60].

For the case where the boundary moves slowly enough for the impurities to move along with it, the average drift velocity of the atoms is given by

$$v_{drift} = \frac{D}{kT} f \quad (1.22)$$

where D is the lattice diffusivity of the impurity atoms and f is the average value of the attractive force applied by the boundary. As the impurity atoms are moving along with the boundary, this will also be the boundary speed. The total force on the boundary will be given by nf , where n is the number of impurity atoms per unit area along the boundary. If the boundary is assumed to move at a constant speed, the drag force must

be equal to the driving force for boundary motion, P . Thus, Equation 1.22 can be rewritten as:

$$v = \frac{DP}{nkT} \quad (1.23)$$

Note that this predicts that the boundary speed will increase linearly with increased driving force and diffusivity of the impurity atoms and will decrease linearly with impurity content. While this is an overly simplistic model of what actually occurs in the boundary, it correctly predicts the direction of trends in speed with each of these variables. The actual relationships are, however, much more complex. It has been observed that very little effect on the boundary speed is seen until a certain critical concentration of impurities is reached [51-53], and that there can often be very large changes in boundary speed with small changes in impurity concentration, driving force, or temperature [53].

1.4.3 Kinetics of phase transformations

Diffusion and thermally activated boundary migration are the primary mechanisms by which phase transformations typically occur in metals. Some of the issues associated with the kinetics of such transformations are discussed in below.

1.4.3.1 Nucleation and growth

Nucleation during a phase transformation is the initial formation of stable second phase regions in an otherwise metastable matrix. In solids, nucleation is almost always heterogeneous, occurring in high-energy sites such as those containing defects like dislocations, grain boundaries, or inclusions. If the creation of a nucleus results in the destruction of all or part of a defect, the free energy released, ΔG_d , will act to reduce the activation energy barrier for the formation of a nucleus. In general, the total change in free energy during heterogeneous nucleation, ΔG_{het} , can be expressed as

$$\Delta G_{het} = -V(\Delta G_v - \Delta G_s) + A\gamma - \Delta G_d \quad (1.24)$$

where V is the transformed volume, ΔG_v is the change in free energy per unit volume due to the transformation, ΔG_s is the increase in free energy due to additional misfit strain arising from a change in density during the transformation, and $A\gamma$ gives the increase in energy due to the creation of additional surfaces. If these energies are known, a critical nucleus size can be calculated. Nuclei larger than this critical size will be stable and continue to grow, while smaller nuclei will be unstable and may return to their previous state. One of the most common locations for the formation of nuclei in polycrystalline materials is at grain boundary triple junctions. These locations allow a forming nucleus to maximize the ΔG_d term and result in a smaller critical nucleus size.

Once stable transformed nuclei have formed in a material, they will start to grow into the surrounding metastable matrix. How this occurs often depends on the nature of the phase transformation. If the two phases have significantly different compositions, as is often the case in many alloys, long-range diffusion through the lattice, as described in Section 1.4.1, will be necessary for the transformation to proceed. If this is typically the rate-limiting step, such transformations are said to be diffusion-controlled. If the two phases have similar compositions, such as in polymorphic transformations of a single component system or massive transformations in alloys, no long-range diffusion is necessary for the phase front to progress through a material. The phase front can progress via thermally activated hopping of atoms across the boundary, as described in Section 1.4.2. Such transformations are said to be interface-controlled. A more detailed discussion of these mechanisms can be found elsewhere [61]. Regardless of the mechanism for growth, these phase-transformed materials often have grain sizes that are very different from their precursors that are a result of the relative rates of nucleation and growth.

Note that impurities can have a significant impact on both the nucleation and growth processes. In addition to the solute drag phenomenon discussed in the previous section, the presence of small amounts of impurities ($\sim 0.01\%$) has been seen to significantly reduce the nucleation rate in aluminum alloys during recrystallization experiments [51]; it is possible that impurities may reduce nucleation rates for phase transformations in a similar fashion. Note also that while small amounts of impurities can play a large role in the kinetics of interface-controlled growth, they should not be as important in diffusion-controlled processes.

1.4.3.2 Shear transformations

At low homologous temperatures, there is often insufficient thermal energy for atoms to overcome their activation energy barriers for diffusion or for thermally activated jumping across a boundary. However, phase transformations can occur at low temperatures in a number of materials, most commonly with the martensitic transformation in quenched steels. This type of transformation is more generally known as a shear transformation. It involves no significant diffusion or other thermally activated motion of atoms but rather relies on the coordinated movement of many atoms over distances of less than an interatomic spacing. These regimented movements are sometimes termed “military” in contrast to the random walk, or “civilian,” movement of atoms during diffusion. While the method by which shear transformations occur is not well-known and a detailed discussion of the current theories is beyond the scope of this review, one of the main characteristics of these transformations of interest in the current study is that there can be no grain growth during shear transformations. This fact can be of use in identifying the mechanism by which a phase transformation occurs and is discussed further in Chapter 3.

REFERENCES

1. Mathieu, H.J., M. Datta, and D. Landolt, *Thickness of natural oxide films determined by AES and XPS with/without sputtering*. J. Vac. Sci. Technol. A, 1985. **3**(2), p. 331-335.
2. Kim, Y., J. Zhao, and K. Uosaki, *Formation and electric property measurement of nanosized patterns of tantalum oxide by current sensing atomic force microscope*. Journal of Applied Physics, 2003. **94**(12), p. 7733-7738.
3. Baker, P.N., *Preparation and properties of tantalum thin films*. Thin Solid Films, 1972. **14**, p. 3-25.
4. Schwartz, N., W.A. Reed, P. Polash, and M.H. Read, *Temperature coefficient of resistance of beta-tantalum films and mixtures with b.c.c.-tantalum*. Thin Solid Films, 1972. **14**, p. 333-347.
5. Westwood, W.D., N. Waterhouse, and P.S. Wilcox, *Tantalum Thin Films*. (Academic Press, London, 1975).
6. Holloway, K. and P.M. Fryer, *Tantalum as a diffusion barrier between copper and silicon*. Applied Physics Letters, 1990. **57**(17), p. 1736-1738.
7. Clevenger, L.A., N.A. Bojarczuk, K. Holloway, J.M.E. Harper, C. Cabral, R.G. Schad, F. Cardone, and L. Stolt, *Comparison of high vacuum and ultra-high vacuum tantalum diffusion barrier performance against copper penetration*. J. Appl. Phys., 1993. **73**(1), p. 300-308.
8. Laurila, T., K. Zeng, and J.K. Kivilahti, *Effect of oxygen on the reactions in the Si/Ta/Cu metallization system*. J. Mater. Res., 2001. **16**(10), p. 2939-2946.
9. Westwood, W.D. and F.C. Livermore, *Phase composition and conductivity of sputtered tantalum*. Thin Solid Films, 1970. **5**, p. 407-420.
10. Lee, S.L. and D. Windover, *Phase, residual stress, and texture in triode-sputtered tantalum coatings on steel*. Surface and Coatings Technology, 1998. **108-109**, p. 65-72.
11. Kondo, K., M. Nakabayashi, K. Kawakami, T. Chijimatsu, M. Nakaishi, M. Yamada, M. Yamabe, and K. Sugishima, *Stress stabilization of β -tantalum and its crystal structure*. J. Vac. Sci. Technol. A, 1993. **11**, p. 3067-3071.
12. Yoshihara, T. and K. Suzuki, *Sputtering of fibrous-structured low-stress Ta films for x-ray masks*. J. Vac. Sci. Technol. B, 1994. **12**(6), p. 4001-4004.
13. Wu, D.S., M.L. Lee, and T.Y. Lin, *Properties of multilayered thin films for thermal ink-jet printing devices*. Applied Surface Science, 1996. **92**, p. 626-629.

14. Baker, S.P., R.-M. Keller, and E. Arzt. *Energy storage and recovery in thin metal films on substrates*. in *Thin-Films-Stresses and Mechanical Properties VII. Symposium, 1-5 Dec. 1997*. (Mater. Res. Soc, Boston, MA, USA, 1998).
15. Read, M.H. and C. Altman, *A new structure in tantalum thin films*. Applied Physics Letters, 1965. **7**(3), p. 51-52.
16. Moseley, P.T. and C.J. Seabrook, *The crystal structure of β -tantalum*. Acta Cryst., 1973. **B29**, p. 1170-1171.
17. Arakcheeva, A., G. Chapuis, and V. Grinevitch, *The self-hosting structure of beta-Ta*. Acta Cryst., 2002. **B58**, p. 1-7.
18. Tillmann, K., A. Thust, A. Gerber, M.P. Weides, and K. Urban, *Atomic structure of β -tantalum nanocrystallites*. Microsc. Microanal., 2005. **11**, p. 534-544.
19. Jiang, A., A. Yohannan, N.O. Nnolim, T.A. Tyson, L. Axe, S.L. Lee, and P. Cote, *Investigation of the structure of β -tantalum*. Thin Solid Films, 2003. **437**, p. 116-122.
20. Rossnagel, S.M., I.C. Noyan, and C. Cabral Jr., *Phase transformation of thin sputter-deposited tungsten*. Journal of vacuum Science and Technology B, 2002. **20**(5), p. 2047-2051.
21. O'Keefe, M.J., S. Horiuchi, J.M. Rigsbee, and J.P. Chu, *Effect of oxygen and carbon on the formation and stability of A-15 crystal structure chromium thin films*. Thin Solid Films, 1994. **247**, p. 169-177.
22. Neal, W.E.J. and R.M.A. Bombin, *Deposition parameters, structure and electrical properties of evaporated tantalum films*. Thin Solid Films, 1977. **44**(2), p. 169-183.
23. Chopra, K.L., M.R. Randlett, and R.H. Duff, *Face-centred cubic modification in sputtered films of tantalum, molybdenum, tungsten rhenium, hafnium and zirconium*. Philosophical Magazine, 1967. **16**, p. 261-273.
24. Clevenger, L.A., A. Mutscheller, J.M.E. Harper, C. Cabral, and K. Barmak, *The relationship between deposition conditions, the beta to alpha phase transformation, and stress relaxation in tantalum thin films*. J. Appl. Phys., 1992. **72**(10), p. 4918-4924.
25. Feinstein, L.G. and R.D. Huttemann, *Factors controlling the structure of sputtered Ta films*. Thin Solid Films, 1973. **16**, p. 129-145.
26. Hoogeveen, R., M. Moske, H. Geisler, and K. Samwer, *Texture and phase transformation of sputter-deposited metastable Ta films and Ta/Cu multilayers*. Thin Solid Films, 1996. **275**, p. 203-206.
27. Ino, K., T. Shinohara, T. Ushiki, and T. Ohmi, *Ion energy, ion flux, and ion species effects on crystallographic and electrical properties of sputter-deposited Ta thin films*. J. Vac. Sci. Technol. A, 1997. **15**(5), p. 2627-2635.

28. Catania, P., R.A. Roy, and J.J. Cuomo, *Phase formation and microstructure changes in tantalum thin films induced by bias sputtering*. J. Appl. Phys., 1993. **74**(2), p. 1008-1014.
29. Hieber, K. and E. Lautenbacher, *Stabilization of sputtered β -tantalum by a tantalum silicide interlayer*. Thin Solid Films, 1980. **66**, p. 191-196.
30. Sosniak, J., W.J. Polito, and G.A. Rozgonyi, *Effect of background-gas impurities on the formation of sputtered β -tantalum films*. Journal of Applied Physics, 1967. **38**(8), p. 3041-3044.
31. Mills, D., L. Young, and F.G.R. Zobel, *Ionic conductivity, dielectric constant and optical properties of anodic oxide films on two types of sputtered tantalum films*. Journal of Applied Physics, 1966. **37**(4), p. 1821-1824.
32. Thornton, J.A. and D.W. Hoffman, *Stress-related effects in thin films*. Thin Solid Films, 1989. **171**(1), p. 5-31.
33. Wu, C.T. *Intrinsic stress of magnetron-sputtered niobium films*. in *International Conference on Metallurgical Coatings, 23-27 April 1979*. San Diego, CA, USA, 1979).
34. Touloukian, Y.S., R.K. Kirby, R.E. Taylor, and P.D. Desai, eds. *Thermal Expansion: Metallic Elements and Alloys*. Thermophysical Properties of Matter, ed. Y.S. Touloukian. Vol. 12. 1975, IFI/Plenum Data Company: New York.
35. Touloukian, Y.S., R.K. Kirby, R.E. Taylor, and T.Y.R. Lee, eds. *Thermal Expansion: Nonmetallic Solids*. Thermophysical Properties of Matter, ed. Y.S. Touloukian. Vol. 13. 1977, IFI/Plenum Data Company: New York.
36. Liu, L., H. Gong, Y. Wang, J. Wang, A.T.S. Wee, and R. Liu, *Annealing effects of tantalum thin films sputtered on [001] silicon substrate*. Materials Science and Engineering C, 2001. **16**, p. 85-89.
37. Thompson, C.V. and R. Carel, *Stress and grain growth in thin films*. J. Mech. Phys. Solids, 1996. **44**(5), p. 657-673.
38. Basseches, H., *The oxidation of sputtered tantalum films*. Journal of the Electrochemical Society, 1962. **109**(6), p. 475-479.
39. Steidel, C.A. and D. Gerstenberg, *Thermal oxidation of sputtered tantalum thin films between 100° and 525°C*. Journal of Applied Physics, 1969. **40**(9), p. 3828-3835.
40. Sato, S., T. Inoue, and H. Sasaki, *Thermal oxidation of beta-Ta below 500°C*. Thin Solid Films, 1981. **86**, p. 21-30.
41. Lugomer, S., M. Kerenovic, M. Stipanovic, and S. Lekic, *Comparitive in situ study of tantalum thin film oxidation in isothermal and nonisothermal conditions*. Vacuum, 1988. **38**(1), p. 15-19.

42. Liu, L., Y. Wang, and H. Gong, *Annealing effects of tantalum films on Si and SiO₂ substrates in various vacuums*. Journal of Applied Physics, 2001. **90**(1), p. 416-420.
43. Giber, J. and H. Oechsner, *Dissolution of anodic Ta₂O₅ layers into polycrystalline tantalum*. Thin Solid Films, 1985. **131**, p. 279-287.
44. Cabral, C., L.A. Clevenger, and R.G. Schad, *Repeated compressive stress increase with 400 C thermal cycling in tantalum thin films due to increases in the oxygen content*. J. Vac. Sci. Technol. B, 1994. **12**(4), p. 2818-2821.
45. Wu, D.S., C.C. Chan, R.H. Horng, W.C. Lin, S.L. Chiu, and Y.Y. Wu, *Structural and electrical properties of Ta-Al thin films by magnetron sputtering*. Applied Surface Science, 1999. **144-145**, p. 315-318.
46. French, B.L. and J.C. Bilello, *In situ observations of the real-time stress-evolution and delamination of thin Ta films on Si (100)*. Thin Solid Films, 2004. **446**, p. 91-98.
47. Lee, H.-J., K.-W. Kwon, C. Ryu, and R. Sinclair, *Thermal stability of a Cu/Ta multilayer: an intriguing interfacial reaction*. Acta Mater., 1999. **47**(15-16), p. 3965-3975.
48. Shewmon, P., *Diffusion in Solids*. 2nd ed. (The Minerals, Metals & Materials Society, Warrendale, PA, 1989).
49. Porter, D.A. and K.E. Easterling, *Phase Transformations in Metals and Alloys*. 2nd ed. (CRC Press, London, 1992).
50. Peterson, N.L., *Diffusion mechanisms and structural effects in grain boundaries*. Journal of Vacuum Science and Technology A, 1986. **4**(6), p. 3066-3070.
51. Lucke, K. and K. Detert, *A quantitative theory of grain-boundary motion and recrystallization in metals in the presence of impurities*. Acta Metallurgica, 1957. **5**, p. 628-637.
52. Cahn, J.W., *The impurity-drag effect in grain boundary motion*. Acta Metallurgica, 1962. **10**, p. 789-798.
53. Lucke, K. and H.P. Stuwe, *On the theory of impurity controlled grain boundary motion*. Acta Metallurgica, 1971. **19**, p. 1087-1099.
54. Hillert, M. and B. Sundman, *A treatment of the solute drag on moving grain boundary and phase interfaces in binary alloys*. Acta Metallurgica, 1976. **24**, p. 731-743.
55. Liu, Z.K., J. Agren, and M. Suehiro, *Thermodynamics of interfacial segregation in solute drag*. Materials Science and Engineering A, 1998. **247**, p. 222-228.
56. Hillert, M., *Solute drag, solute trapping and diffusional dissipation of Gibbs energy*. Acta Mater., 1999. **47**(18), p. 4481-4505.

57. Hillert, M. and M. Schalin, *Modeling of solute drag in the massive phase transformation*. Acta Mater., 2000. **48**, p. 461-468.
58. Mendeleev, M.I. and D.J. Srolovitz, *A regular solution model for impurity drag on a migrating grain boundary*. Acta Mater., 2001. **49**, p. 589-597.
59. Vilenkin, A., *Interaction of solute impurity with grain boundary: the impurity drag effect*. Interface Science, 2001. **9**, p. 323-329.
60. Hillert, M., *Solute drag in grain boundary migration and phase transformations*. Acta Mater., 2004. **52**, p. 5289-5293.
61. Hillert, M., *Diffusion and interface control of reactions in alloys*. Metallurgical Transactions A, 1975. **6A**, p. 5-19.

Chapter 2

Experimental Details

2.1 Overview

This chapter contains information not included in Chapters 3-7 about the experimental methods used in this thesis. It comprises a brief overview of the UHV sputter deposition and stress measurement system used in this work, as well as details about the different microstructural analysis techniques that were employed, including a review of the function and limitations of the electron backscatter diffraction (EBSD) techniques used in Chapters 6 and 7.

2.2 Film deposition and thermal cycling

Film deposition and thermal cycling were conducted in a custom-made UHV sputter deposition and stress measurement system, shown schematically in Figure 2.1. The system consists of a high vacuum load-lock chamber and three UHV chambers with typical base pressures below 10^{-9} Torr: a sputter deposition chamber, a sample heating chamber for *in situ* substrate curvature stress measurements, and a transfer chamber.

All samples studied in this thesis were prepared in the following manner. 100 mm diameter (100) oriented single crystal silicon or amorphous fused silica substrates were placed into the load-lock chamber, which was evacuated to a pressure less than 10^{-8} Torr before introduction to the transfer chamber. A manipulator arm in the transfer chamber was used to move the substrates from the load-lock to the sample heating chamber, where a reference substrate curvature measurement was taken. From there,

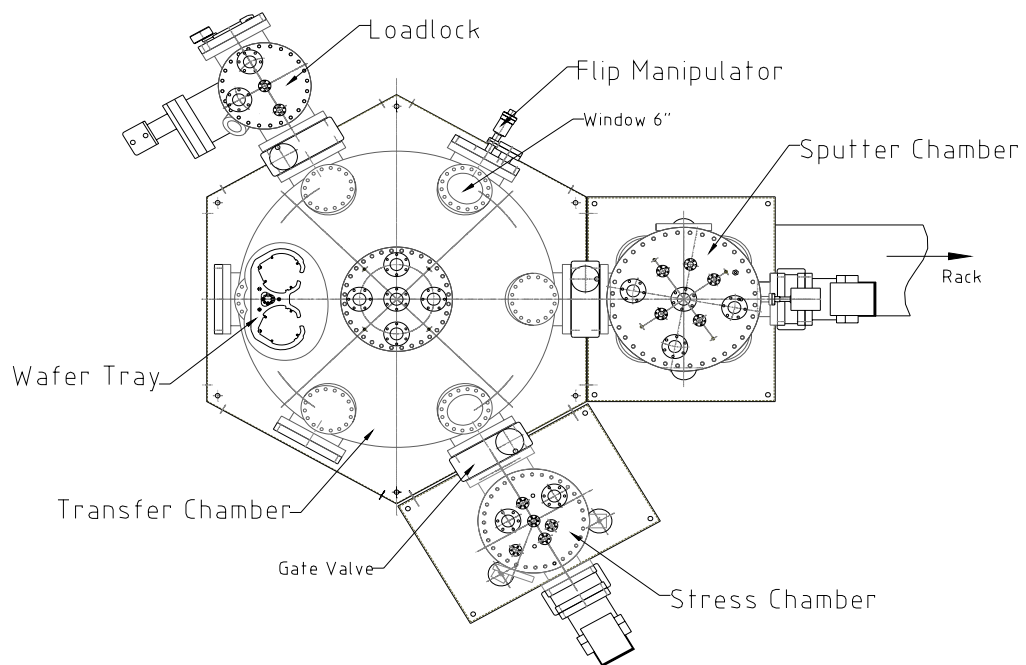


Figure 2.1: Schematic diagram of the UHV system used for deposition and thermal cycling of the tantalum films investigated in this thesis.

the substrate was moved to the deposition chamber, where films were sputter deposited as described in Chapters 3-7. Following deposition, samples were returned to the sample heating chamber using the manipulator arm. In this chamber, samples were subjected to thermal cycling while film stresses were monitored by substrate curvature measurements [1-3] performed using a two-dimensional laser scanning method in which substrate curvature was measured in two perpendicular directions across the substrate surface [4]. Further details regarding the UHV system can be found elsewhere [4].

Average biaxial stress in a thin film can be determined from changes in substrate curvature. Edge forces exerted on the substrate by the biaxial stress in the film cause the substrate to deform elastically in biaxial bending. The amount of bending depends on the stress in the film, σ_f , the thicknesses of the film and substrate, t_f and t_s , and the biaxial elastic modulus of the substrate, Y_s , according to:

$$K = \frac{1}{R} = \frac{6\sigma_f t_f}{Y_s t_s^2} \quad (2.1)$$

where K is the curvature and R is the radius of curvature. Thus, the stress in a film can be determined from the curvature by:

$$\sigma_f = \frac{Y_s t_s^2}{6t_f} K = \frac{Y_s t_s^2}{6t_f R} \quad (2.2)$$

Note that equations 2.1 and 2.2 assume an initially flat substrate. As typical substrates will almost always have some initial curvature, K_o , K must be replaced by $\Delta K = K - K_o$, which leads to:

$$\sigma_f = \frac{Y_s t_s^2}{6t_f} (K - K_o) = \frac{Y_s t_s^2}{6t_f} \left(\frac{1}{R} - \frac{1}{R_o} \right) \quad (2.3)$$

which is commonly known as the Stoney equation [1]. This method of determining stresses in thin films can be very useful, as it requires no information regarding the material properties of the film, which are often unknown. Note that stresses induced in

the film due to the curvature of the substrate or to the compliance of the substrate are ignored in this calculation. As the maximum curvature and stress in the substrate are both small for the current studies ($\sim 0.05 \text{ m}^{-1}$ and 1 MPa, respectively), their effect on the resultant film stress is negligible ($\pm \sim 1.5 \text{ MPa}$).

The design of the UHV sputter deposition and stress measurement system is particularly useful in this work due to the high degree of atmospheric control during sample synthesis, testing, and the time between. Using this system, it is possible to deposit and thermally cycle films without significant exposure to reactive atmospheric contaminants such as oxygen. It is also possible to expose samples to controlled amounts of impurities at any time by the use of leak valves located in both the sputter deposition chamber and the sample heating chamber. This allows the effects of small amounts of contaminants added at various times during the deposition and testing process to be studied precisely.

While this particular UHV system is well suited to the requirements of the experiments performed in this thesis, there are certain limitations in the data that could be collected, primarily associated with the sample heating chamber. Temperature control during thermal cycling was not precise in UHV, as heat transfer could only be accomplished by radiation. As such, ramp rates were somewhat variable, with oscillations in temperature of up to $\pm 15^\circ\text{C}$. The ramp rates during heating reported in later chapters were an average over $\sim 40^\circ\text{C}$. While the ramp rates during much of the cooling half-cycle did not suffer as much local variation due to the low power output required, the cooling rate was highly dependent on temperature, especially below 200°C . Cooling from 200°C to room temperature generally took several hours, much slower than the average ramp rates over the rest of the experiment (typically $\sim 5^\circ\text{C}/\text{min}$.) Fortunately, slow cooling rates did not appear to greatly affect the thermomechanical behavior of the tantalum films, as the homologous temperature was too low for significant stress

relaxation to occur. Previous thermal cycling experiments using this UHV system had been performed using 1 Torr of filtered ultra-high purity helium to promote more controllable heat transfer rates [4, 5]; this method proved unsuccessful in studying tantalum films as even the filtered helium contained sufficient oxygen to noticeably affect the thermomechanical behavior of the films studied.

Uncontrollable variations in the temperature ramp rate of samples thermally cycled under UHV conditions led to some uncertainty in the temperature during stress-temperature measurements. As a substrate curvature measurement would take up to 10 seconds to complete, there were occasionally changes in temperature of several degrees while the measurement took place. This can be described by a maximum uncertainty in the temperature during heating of $\pm 3^\circ\text{C}$ near the end of the heating half-cycle. As the cooling rates did not suffer as much local variation, the temperature uncertainty was approximately $\pm 1^\circ\text{C}$ during the cooling half-cycle.

In addition to this uncertainty in temperature, precision in stress measurements was limited to $\pm \sim 10$ MPa, primarily due to vibrations in the room. Absolute system accuracy was difficult to gauge. Small shifts in substrate position between the measurements of K_o and K could lead to substantial changes in calculated stress values, as the initial curvature of a substrate is typically non-spherical. Often, the differences in stress calculated in two perpendicular directions in the plane of the film were as high as 100 MPa. As the average of these stress values is reported in later chapters, it is not unreasonable to assign an uncertainty in absolute stress of ± 50 MPa.

2.3 Microstructure analysis

As the UHV chamber was not outfitted for microstructure characterization, all characterization was performed *ex situ*. A variety of techniques were used to determine the crystal structure and orientation distribution (both locally and globally), dislocation

structure, and thickness of different tantalum films. Details of these measurements are given in the following sections.

2.3.1 X-ray diffraction

Symmetric x-ray scans, where 2θ varies and the scattering vector is always normal to the sample surface, were performed using a Scintag, Inc. θ - θ diffractometer shown schematically in Figure 2.2. These scans were performed primarily to determine the tantalum crystal phase(s) present in a given sample and also provided some information about the orientation distribution of these crystal structures, giving a qualitative measure of which crystal planes were aligned parallel to the film surface. X-rays were generated from a copper source having a K- α wavelength of 1.5405 Å. All scans shown in Chapter 3 were performed with the source voltage set at 45 kV and the detector current at 40 mA. The slits used (as shown in Figure 2.2) were 1 mm for the divergent beam slit and 3 mm for the scatter slit on the source, and 0.3 mm for the scatter slit and 0.1 mm for the diffracted beam slit on the detector. Samples were cut so as to ensure a uniform beam footprint on each.

For the small-grained as-deposited β phase films, θ - 2θ x-ray scans were also used to determine average grain size. The grain size, d , of very small crystallites can be determined from the measured width of their diffraction curve using Scherrer's formula [6]:

$$d \approx \frac{\lambda}{B \cos \theta_B} \quad (2.2)$$

where λ is the wavelength of the incident x-rays, B is the full width of the x-ray peak at half of its maximum intensity, and $2\theta_B$ is the nominal 2θ value of the peak. Note that this is only an approximate value and does not account for other factors that may cause peak broadening, such as inhomogeneous stresses in the sample.

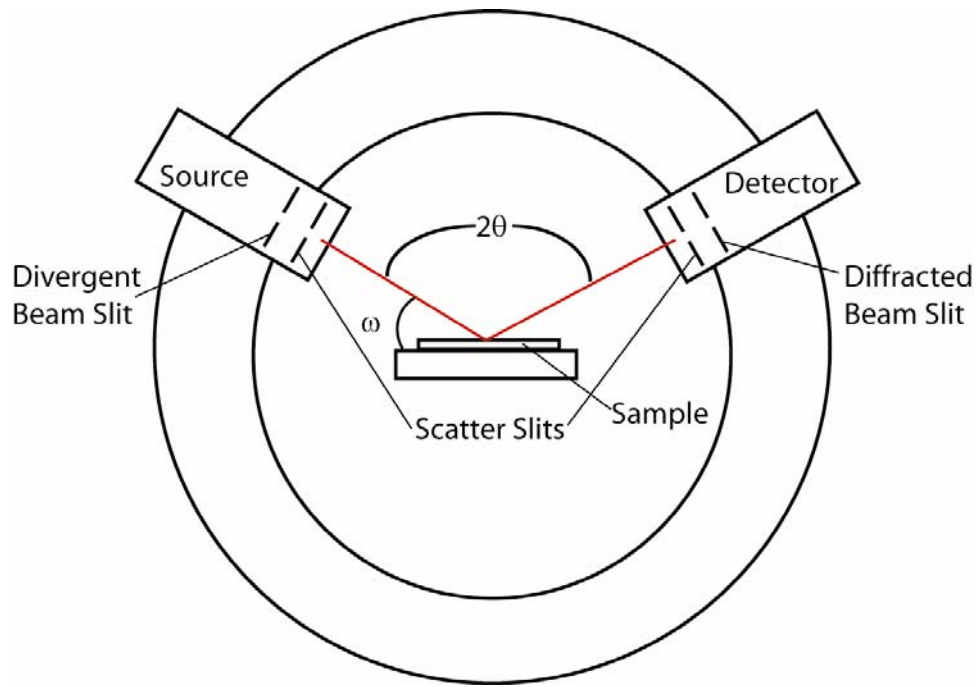


Figure 2.2: Schematic diagram of the 2-circle θ - θ diffractometer.

A series of rocking scans, where 2θ is held constant and the angle between the x-ray source and the sample plane, ω , varies, were used to quantitatively estimate the volume fraction of β phase remaining in a film after thermal cycling to various temperatures. This is possible because the β phase is very well textured in the films studied here, with (002) planes oriented within a few degrees of the surface and a random in-plane orientation. The “volume” of the (002) β phase x-ray peak, given by the integrated intensity of the series of rocking scans, can thus be used to estimate the amount of β phase in a given sample by comparing its (002) β phase peak volume to that of an as-deposited film that is roughly 100% β phase. To measure the peak volume, a series of nine rocking scans in ω was taken for each sample with 2θ values varying by 0.1° , centered at the 2θ value corresponding to (002) β peak maximum in a θ - 2θ scan. Peak volume was calculated by multiplying each peak area in ω by a width of 0.1° in 2θ and summing over the series of rocking scans. The amount of β phase remaining in a given sample was estimated by the ratio of the peak volume of the sample of interest to the peak volume of an as-deposited film.

A similar analysis was performed on several samples using a General Area Detector Diffraction Source (GADDS). Samples were scanned in GADDS using a geometry similar to that of a θ - θ diffractometer, but with a CCD area detector instead of a line detector. In this way, a range of 2θ and ω angles can be observed simultaneously and peak volumes can be found in a single scan. Peak volume analysis in GADDS has the advantage of being much faster than the series of rocking scans described above, but it is also less accurate due to the limited resolution of the detector.

2.3.2 Electron backscatter diffraction (EBSD)

EBSD was used to characterize the microstructure of all α phase samples. The technique is based on the acquisition and rapid automated analysis of diffraction patterns

from samples in a scanning electron microscope (SEM). A schematic of a typical EBSD setup is shown in Figure 2.3 [7]. An electron beam is focused onto the sample surface at an incident angle 70° from the surface normal. As the electron beam enters the crystal, it scatters diffusively in all directions. As a result, there are always some electrons arriving at the Bragg angle for every set of lattice planes, diffracting a portion of the incoming beam. The source of electron scattering can be considered to be between lattice planes, and thus two cones of radiation are produced from each family of planes, one from either side of the source [8]. If a recording medium is positioned so as to intercept the cones, a pair of parallel conic sections result which are nearly straight and appear as parallel lines. These lines are called Kikuchi lines, and each pair has a distinct width that corresponds to a distinct set of crystallographic planes. The pattern of these lines, called the Kikuchi pattern, contains information regarding all of the angular relationships within a crystal. This pattern is captured by a CCD camera, noise reduced by averaging over several frames and subtracting background noise, and analyzed to determine the three dimensional crystal orientation at that location. By scanning an array of points across the sample surface, maps depicting local crystal orientation can be generated. The crystallographic data obtained can be further analyzed to generate pole figures or other means of displaying orientation distributions.

To generate the EBSD orientation maps shown in Chapters 6 and 7, a Leica 440 SEM operating at an accelerating voltage 25 kV and a probe current of 1.2 nA was used in conjunction with an HKL Nordlys II EBSD area detector and HKL's CHANNEL 5 software. Samples were prepared by cleaving a samples into $\sim 1 \text{ cm}^2$ squares and adhering to an aluminum stud using cyanoacrylate adhesive. In order to prevent charging of the sample, the perimeter was coated with conductive carbon paint, establishing electrical contact between the sample surface and the SEM stud. Diffraction patterns were collected using the CHANNEL 5 software with 4×4 binning

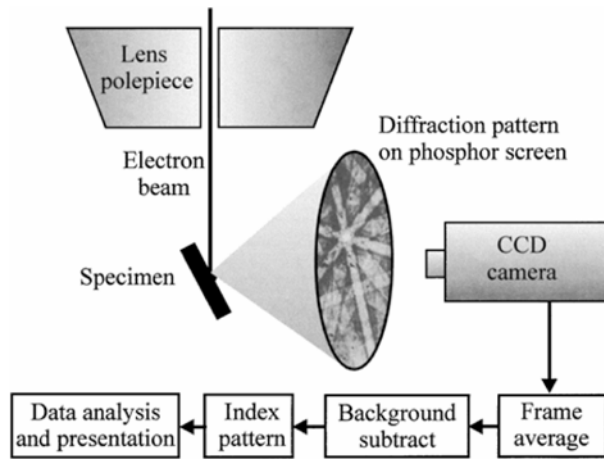


Figure 2.3: Schematic diagram of a typical EBSD setup [7].

and “high” gain, averaged over ten frames, and subjected to a static background subtraction before they were analyzed. Band detection was performed using the following settings in the CHANNEL 5 software: band center detection, standard divergence, 4–5 bands detected, and a Hough space resolution of 60. Scans were performed in “beam scan” mode and required approximately 0.8 seconds per data point for pattern collection and analysis.

Two dimensional orientation maps were generated by scanning a 120×120 point array with a measurement point spacing of 100 nm. These scans were performed to study local orientation variations and to obtain an estimate of the grain size of a sample. These data are displayed according to their out-of-plane crystal orientation and show “high-angle” and “low-angle” grain boundaries, which we have arbitrarily defined as greater than 8° and between 2° and 8° , respectively.

Noise reduction was performed on most orientation maps using two methods. First, the CHANNEL 5 software identified and removed pixels deemed to be wrongly indexed. Then, certain non-indexed data points were replaced with an average of the surrounding data points. Points that have been indexed incorrectly are called “wild spikes” and can sometimes occur when a diffraction pattern is symmetrical or when the pattern quality is low [7]. Incorrect indexing is rare in a well-calibrated system, and these points usually appear as isolated pixels surrounded by high-angle grain boundaries on an orientation map. The software allows such points to be identified and removed automatically. Poor pattern quality, usually due to surface irregularities, high dislocation densities, or grain boundaries, can also cause the software to be unable to identify the crystal orientation of a particular location. These non-indexed points show up on an orientation map as black pixels. If a non-indexed point is surrounded by a user-determined number of indexed points (from 1–8, we chose 5 for the orientation maps shown in Chapters 6 and 7), the non-indexed point is replaced by the average

orientation of its indexed neighbors. In generating orientation maps for the tantalum films studied in this work, typically about 80–85% of the points were correctly indexed, with ~ 1–2% wild spikes and the remainder non-indexed. Following noise reduction, greater than 90% of the points on an orientation map were indexed. Noise reduction was performed only on orientation maps to provide a better representation of the local microstructure of these films. A comparison of raw and noise-reduced data is shown in Figure 2.4.

Global orientation distributions were determined from data obtained by scanning a much larger area in a sample using a much larger step size (~ 1–2 μm). Several scans were performed in various locations on each sample in order to obtain a statistically relevant distribution. These data have been displayed in pole figures and inverse pole figures generated by the CHANNEL 5 software with a Gaussian width around each point of 8° .

Grain boundary spacing and character were determined from a series of line scans. Points along a line on the sample surface were scanned in the EBSD with a step size of 100 nm over a distance of 40 μm . A series of 5 lines was scanned with a spacing between lines of 1–2 μm . The particular spacing used for a given sample was determined from the estimated grain size (from previously collected orientation maps) such that samples with larger grain sizes had a larger spacing between lines. Multiple sets of line scans were performed in random locations on the sample surface and with the sample rotated randomly around the film normal. Boundary spacing and character were determined from misorientation profiles generated along each line. Abrupt changes of greater than 2° were considered as boundaries, with the exception of single pixel “grains,” which were left out of the analysis as it could not be determined from line scans whether these points were correctly indexed. As such, only those grains larger than ~ 200 nm were considered in this analysis. Grain boundaries were character-

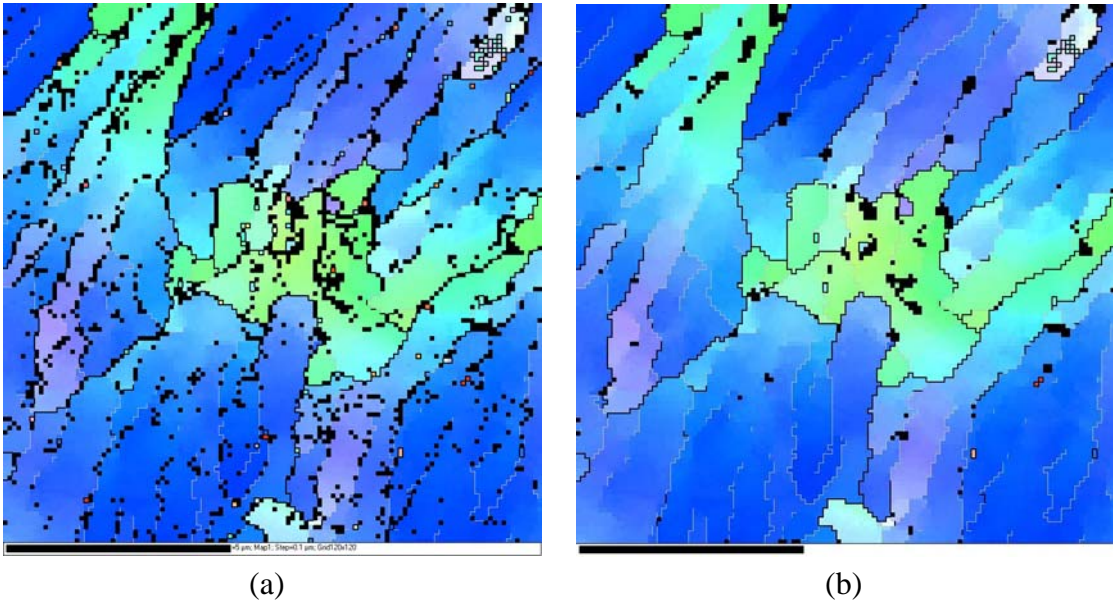


Figure 2.4: Comparison of EBSD maps showing (a) raw and (b) noise-reduced data.

ized by their misorientation and grouped into the following categories: low-angle (2° – 5°), medium-angle (5° – 15°), or high-angle ($> 15^\circ$). Grain size was determined by the mean boundary spacing over all line scans performed on a given sample.

As many of the grains contained orientation gradients, the axes of rotation between neighboring pixels within a grain were identified using MATLAB. The orientation data from an EBSD map was exported as a listing of pixel position and a set of three Euler angles describing the crystal orientation at that location. Axes of rotation between neighboring pixels in both sample coordinates and crystal coordinates were calculated from these data and displayed on “rotation pole figures.” Unfortunately, axes of rotation between pixels determined from EBSD can have limited accuracy, especially when dealing with small rotations such as those commonly found in most of the samples detailed in Chapters 6 and 7. For the tantalum films analyzed in this thesis, the maximum angular uncertainty was estimated at $\pm 0.1^\circ$. As the pixel-to-pixel angular uncertainty is of the same order of magnitude as the long-range orientation gradients seen in many samples, there is a large uncertainty in identifying a particular axis of rotation, as described by Prior [9] and Bate *et al* [10], which can be expressed as:

$$\langle \beta \rangle = \tan^{-1}(\delta / \omega) \quad (2.3)$$

where $\langle \beta \rangle$ is the average angle error in the misorientation axis and δ the error in determining the misorientation angle ω between pixels, leading to an uncertainty of up to 20° in the determination of any given axis of rotation. Despite the potential error in determining a particular axis of rotation, if consistent long-range orientation rotations around a particular axis are present, the data will be distributed around a peak that can be detected.

It has been shown that the “orientation noise” is a strong function of probe current in the SEM and that higher current results in less noise and better Kikuchi pattern quality [11]. Unfortunately, high probe currents can also adversely affect the spatial

resolution of the scan [11]; thus, the probe current was not altered from its 1.2 nA setting.

2.3.3 Film thickness measurements

Film thicknesses were measured either using Rutherford Backscattering Spectrometry (RBS) or profilometry in CCMR facilities at Cornell University. Film thicknesses determined using profilometry were determined from an average of several scans taken across regions near the edge of the substrate that were shadowed during deposition. As the film thickness has been shown to vary by $\sim 10\%$ from the center to the edge of the substrate in this system [4], appropriate corrections were made in the calculations of film stress described in Section 2.2. Films analyzed using RBS were subjected to a He^{2+} ion beam at an energy of ~ 2 MeV and an angle of incidence of $\sim 15^\circ$. Film thicknesses were determined using RUMP analysis, accurate to $\pm 10\text{\AA}$. Thicknesses of films deposited in oxygen-containing atmospheres were not analyzed, as these films delaminated after exposure to atmosphere. While RBS can also be used to determine film composition, oxygen concentrations were too low to be detected in any of the samples analyzed by RBS.

REFERENCES

1. Stoney, G., *The tension of metallic films deposited by electrolysis*. Proceedings of the Royal Society of London, 1909. **A82**, p. 172-175.
2. Flinn, P.A., D.S. Gardner, and W.D. Nix, *Measurement and interpretation of stress in aluminum-based metallization as a function of thermal history*. IEEE Transactions on Electron Devices, 1987. **ED-34**(3), p. 689-699.
3. Nix, W.D., *Mechanical properties of thin films*. Metallurgical Transactions A, 1989. **20A**, p. 2217-2245.
4. Shu, J.B., *Plastic deformation and thermomechanical behavior of passivated copper thin films on silicon substrates*, Ph.D. thesis, Cornell University, 2003.
5. Shu, J.B., B. Clyburn, T.E. Mates, and S.P. Baker, *Effect of oxygen on the thermomechanical behavior of passivated Cu thin films*. Journal of Materials Research, 2003. **18**(9), p. 2122-2134.
6. Scherrer, P., *Estimation of the size and structure of colloidal particles by Rontgen rays*. Nachrichten von der Koniglichen Gesellschaft der Wissenschaften zu Gottingen, Mathematisch-Physikalische Klasse, 1918. **2**, p. 96-100.
7. Humphreys, F.J., *Grain and subgrain characterisation by electron backscatter diffraction*. Journal of Materials Science, 2001. **36**, p. 3833-3854.
8. Randle, V. and O. Engler, *Introduction to texture analysis: Macrotecture, microtexture, and orientation mapping*. (Taylor & Francis, London, 2000).
9. Prior, D.J., *Problems in determining the misorientation axes, for small angular misorientations, using electron backscatter diffraction in the SEM*. Journal of Microscopy, 1999. **195**(3), p. 217-225.
10. Bate, P.S., R.D. Knutsen, I. Brough, and F.J. Humphreys, *The characterization of low-angle boundaries by EBSD*. Journal of Microscopy, 2005. **220**(1), p. 36-46.
11. Humphreys, F.J., Y. Huang, I. Brough, and C. Harris, *Electron backscatter diffraction of grain and subgrain structures - resolution considerations*. Journal of Microscopy, 1999. **195**(3), p. 212-216.

Chapter 3

Effect of oxygen on the thermomechanical behavior of tantalum thin films during the β - α phase transformation

Robert Knepper, Blake Stevens, and Shefford P. Baker

*Cornell University, Department of Materials Science and Engineering, Bard Hall,
Ithaca, NY 14853-1501*

Reused with permission from Robert Knepper, Blake Stevens, and Shefford P. Baker, Journal of Applied Physics, 100, 123508 (2006). Copyright 2006, American Institute of Physics.

3.1 Abstract

Tantalum thin films were prepared in the metastable β phase, and their thermomechanical behaviors were investigated *in situ* in an ultrahigh vacuum environment. Controlled levels of oxygen were incorporated into the films either during deposition, by surface oxidation after deposition, or during thermomechanical testing. The transformation from the β phase to the stable α phase takes place in conjunction with a distinct increase in tensile stress. The thermomechanical behavior is strongly affected by the amount of oxygen to which the film is exposed and the method of exposure. Increasing oxygen content inhibits the phase transformation, requiring higher temperatures to reach completion. It is shown that the phase transformation takes place by a nucleation and growth process that is limited by growth. Changes in the activation en-

ergy for the phase transformation due to solute drag are estimated as a function of oxygen content and the mechanisms behind the stress evolution are elucidated.

3.2 Introduction

Tantalum thin films are of interest for use in micro- and nano-fabricated devices because of the wide range of properties available. Depending on the deposition conditions and substrate, Ta films can be formed with one of two different crystal structures [1-5]: the stable bcc α phase, or the metastable tetragonal β phase [6-8]. The β phase is found only in thin films and has a high resistivity ($\sim 180 \mu\Omega \text{ cm}$), making it suitable for thin film resistors and heaters [1, 9-11]. It is easier to pattern using reactive ion etching than the α phase [12] and is therefore also used for masks in x-ray optics [12, 13]. The α phase is the only known stable polymorph of tantalum. It has a much lower resistivity ($\sim 13 \mu\Omega \text{ cm}$), is less brittle, and is commonly used for thin film capacitors [9-11] and is preferred as a diffusion barrier between copper and silicon in microelectronic devices [14-16].

Stresses that build up in these films during thermal cycling can cause reliability problems in devices, as they may lead to cracking or delamination [17, 18]. Two processes having to do with irreversible microstructural changes can act to produce very large changes in stress in Ta films during thermal cycling: the incorporation of oxygen into the film and the β - α phase transformation. Two distinct types of thermo-mechanical behavior corresponding to these processes have been reported for Ta films, as shown in Figure 3.1.

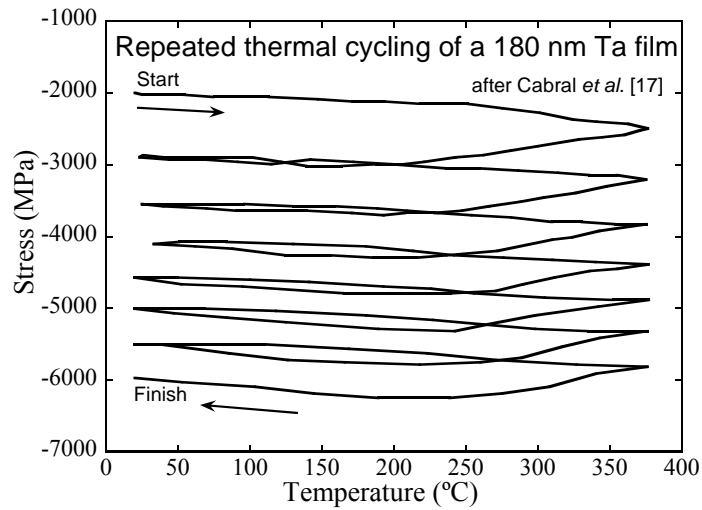
A few groups [17-19] have reported large changes in stress in the compressive direction in films cycled between room temperature and 400–450°C (*e.g.* Figure 3.1a). In these studies, stresses were determined from changes in substrate curvature measured in inert-gas-purged but nonetheless oxygen-containing atmospheres. Cabral *et al.*

[17] determined that atmospheric oxygen diffused into the bulk of the films at elevated temperatures, causing an expansion of the equilibrium in-plane dimension of the films. As each film was constrained by its substrate and not permitted to expand, compressive stresses developed. With repeated thermal cycling, these stresses reached magnitudes as high as ~ 6 GPa [17] (Figure 3.1a). While the crystal structure remained that of the β phase, Auger electron spectroscopy (AES) depth profiling indicated that more than 10 at.% of oxygen was incorporated into the film [17]. In a different study [20], similar films heated to 600°C in air oxidized completely to form Ta_2O_5 , and compressive stresses of up to -4 GPa were observed before the films started to blister in order to relieve stress.

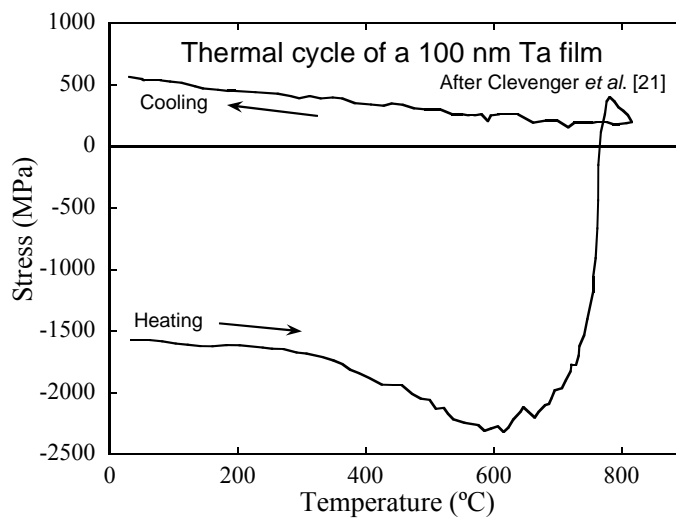
By heating samples to higher temperatures, Clevenger *et al.* [21] found a different behavior in substrate curvature experiments conducted in helium-purged atmospheres (Figure 3.1b). While their samples showed the same shift towards compression as those reported by Cabral *et al.* [17] at lower temperatures (indicating the presence of oxygen during thermal cycling), a large change in stress in the tensile direction was seen above 600°C during the first heating half cycle. X-ray measurements showed that the films were β phase before and α phase after thermal cycling, and these authors attributed the large tensile stress change to the phase transformation.

While the previous studies of the thermomechanical behavior of thin Ta films [17-21] have shown that large stress changes are possible, the range of likely stress evolution behaviors has not been elucidated. To do so requires progress in three areas:

- The mechanism of the β - α phase transformation must be understood. It has been suggested [21] that it occurs by a shear distortion along the (001) planes of the tetragonal β phase. However, recent work suggests that β -Ta has a σ -type structure [8] and a simple shear mechanism is not sufficient to transform a σ -type structure to bcc [22]. On the other hand, molecular dynamics studies by



(a)



(b)

Figure 3.1: (a) Thermomechanical behavior of a 180 nm Ta film cycled repeatedly to 400°C in an atmosphere containing a small, but undetermined amount of oxygen, after Cabral *et al.* [17]. (b) Thermomechanical behavior of a 100 nm Ta film thermally cycled to 850°C, after Clevenger *et al.* [21]. X-ray analysis showed the film to be β phase as-deposited and α phase after cycling.

Jiang, Tyson, and Axe [23] were unable to show this to be a nucleation and growth process since no α phase formed during their simulations of the annealing of single crystals of the β phase up to the melting temperature.

- The pathways by which oxygen can be incorporated into films must be explored. Existing studies have looked only at the effects of oxygen incorporated during thermal cycling. However, oxygen may be incorporated into a film during deposition, or an oxide layer may be grown on the film surface by exposure to atmosphere following deposition. The latter case is particularly interesting since it is known that the thin (~ 2 nm), stable, passivating oxide that forms on the surface at low temperatures [24, 25] can dissolve into the bulk of the film when heated above 375°C in a high vacuum environment [26].
- The effect of oxygen content on the phase transformation must be understood. It has been qualitatively observed that the β - α phase transformation is inhibited by increasing oxygen content in the film [27], but neither a quantitative analysis nor a mechanism has been proposed. Since the prior data are from oxygen-containing films, the behavior of oxygen-free tantalum films has not been previously reported.

Understanding these phenomena is not only of fundamental interest, but may also be technologically important. Understanding the effects of oxygen and the phase transformation on the evolution of stress in these films necessary in order to avoid mechanical failure of devices. Furthermore, the ability to control the phase transformation leads to new possibilities in devices and fabrication. For example, one may wish to ensure that a β phase component in a device remains in the β phase under operating conditions. On the other hand, one may wish to take advantage of the fact that the β phase can easily be patterned using standard microfabrication methods [12] and then transform the patterned film to the α phase for use in a device.

In the present work, we address all three of the bulleted points above. We prepared Ta films in the β phase using a special vacuum system in which both film deposition and stress measurements can be performed in the same ultra-high vacuum (UHV) environment [28]. We incorporated controlled levels of oxygen into the films either during deposition, by surface oxidation after deposition, or during thermomechanical testing. We obtained stress-temperature (σ - T) data for all films, without adding additional oxygen in the former two cases. The microstructure of these films was examined *ex situ* using x-ray diffraction. From these data, the relationships among thermomechanical behavior, microstructure evolution, and oxygen content were determined. The mechanisms of the phase transformation and oxygen incorporation are described, along with their effects on stress evolution. Furthermore, the effect of oxygen content on the phase transformation is quantified and interpreted in terms of a solute drag model.

3.3 Experiment

3.3.1 Sample preparation

Samples were prepared by magnetron sputter deposition in a UHV chamber evacuated to less than 2×10^{-9} Torr. This UHV deposition system uses a confocal arrangement in which the substrate is mounted on a rotating stage over several 76 mm diameter magnetron sputter guns oriented 23° from the substrate normal and with a mean target-to-substrate distance of 12.5 cm. 100 mm diameter oxidized Si (100) substrates were used. Before deposition, each substrate was cleaned using a 25 W radio-frequency bias in 8 mTorr of argon (99.9997% pure) for 1 minute to remove adsorbed gas molecules from the substrate surface. Tantalum films were then sputtered to a thickness of 300–400 nm using a DC magnetron source and a 99.95% pure Ta target containing ~ 15 ppm oxygen. A sputtering pressure of 8 mTorr of argon and a sputtering power of \sim

400 W were used. The Ta deposition rate was approximately 15 nm/min. All films were deposited with the substrate grounded. Substrates were rotated at 5 rpm and were unheated during deposition. The maximum temperature reached during deposition was approximately 100°C, as measured by a thermocouple located behind the substrate.

Four sets of films were prepared. The first was not exposed to oxygen beyond that in the base pressure. For the second, a fixed oxygen partial pressure in the range of 1.7×10^{-6} to 1.5×10^{-5} Torr was added to the sputtering gas during deposition by use of a leak valve, with the partial pressure measured both before and after deposition. The third set of films were deposited without oxygen but were exposed to different, higher concentrations of oxygen (0.1–31 mTorr) immediately following deposition by opening a leak valve until the pressure in the chamber reached a predetermined value, holding for a few seconds, then quickly closing the valve. Films in the fourth set were exposed to oxygen-containing atmospheres only during thermal cycling as described below.

3.3.2 Thermal cycling and stress measurements

After deposition, samples were transferred to a vacuum furnace within the same UHV system. Films were thermally cycled in UHV, except for the fourth set, which were cycled in atmospheres containing a small amount of oxygen ($\sim 10^{-5}$ Torr). Thermal cycles were between room temperature and 700°C at 5°C/min. The well-known substrate curvature method [29, 30] was used to determine the stresses in the film *in situ* during thermal cycling. Changes in the curvature of the film/substrate package due to changes in the equilibrium in-plane dimensions of the film relative to the substrate were measured using a custom-designed system [28] that employs an optical deflection curvature measurement technique. Film stresses were calculated from these meas-

urements using the Stoney equation [31]. For the experiments reported here, this system has a stress accuracy of about 40 MPa, and a precision of about 10 MPa.

3.3.3 Microstructural characterization

All films were characterized *ex situ* at room temperature. Two types of x-ray scans were used to determine the crystal phases and orientations present in the films. These scans were completed using a θ - θ x-ray diffractometer (Scintag, Inc.). The diffractometer used a copper x-ray source operated at 45 kV and 40 mA with a wavelength of 1.5405 Å (k- α). All samples were large enough that the entire beam illuminated the sample, ensuring a uniform beam footprint. Symmetric θ - 2θ scans were used for phase identification and for determining grain size in the as-deposited film using Scherrer analysis [32]. For these scans, the scattering vector was held parallel to the film normal, while the angle, θ , between the incident beam and the film plane was varied. Scans over the range $10^\circ \leq 2\theta \leq 100^\circ$ were used to identify the lattice planes oriented parallel to the film plane. Rocking scans were conducted by holding 2θ constant while varying the angle, ψ , between the scattering vector and the film plane normal. Scans were taken at a series of 2θ values in increments of 0.1° around the (002) peak from each film, centered at the peak maximum of the θ - 2θ scan ($33.4^\circ \leq 2\theta \leq 34.4^\circ$, $-15^\circ \leq \psi \leq 15^\circ$, resolution = 0.02°), in order to determine the peak volume (peak intensity integrated over 2θ and ψ). This volume was used to obtain a quantitative estimate of the amount of β phase remaining after thermal cycling by comparing the peak volume after cycling with that of an as-deposited film. Grain sizes in the films after thermal cycling were analyzed using electron backscatter diffraction (EBSD), as described by Knepper *et al.* [33]. Film thickness measurements were performed using Rutherford

backscattering spectrometry (RBS). All films were found to be within 350 ± 40 nm thick.

3.4 Films without added oxygen

3.4.1 Results

Stress-temperature data for Ta films with no added oxygen cycled between room temperature and 335°, 355°, 450°, and 600°C are shown in Figure 3.2. To ensure minimal oxygen exposure over the entire experiment, the base pressure in the system was maintained at less than 2×10^{-9} Torr throughout deposition and testing. The stress in the as-deposited films at room temperature is about 900 MPa in compression. As each film is heated, the stresses gradually become more compressive due to thermal mismatch between the film and substrate. Up to about 275°C, the stress-temperature data from all films follow a thermoelastic line. Between 300° and 375°C, there is a drastic change in stress in the tensile direction for all films, with the magnitude of the stress jump reaching approximately 1.2 GPa for films cycled to maximum temperatures (T_{max}) greater than 375°C. At temperatures greater than 375°C, thermoelastic behavior is seen on both heating and cooling. For films cycled to lower temperatures, thermoelastic behavior is again observed on cooling below $\sim 250^\circ\text{C}$. An overall stress change of approximately 1.6 GPa is seen over the first thermal cycle for films cycled to $T_{max} > 375^\circ\text{C}$. For these films, subsequent thermal cycles to temperatures up to 600°C approximately retrace the first cycle cooling data on both heating and cooling. In contrast with previously reported films that were presumably cycled in oxygen-containing atmospheres (Figure 3.1b) [21], the large tensile stress jump occurs at a much lower temperature and over a much narrower temperature range (*i.e.* much more quickly), and the behavior prior to this stress jump is fully reversible (thermoelastic).

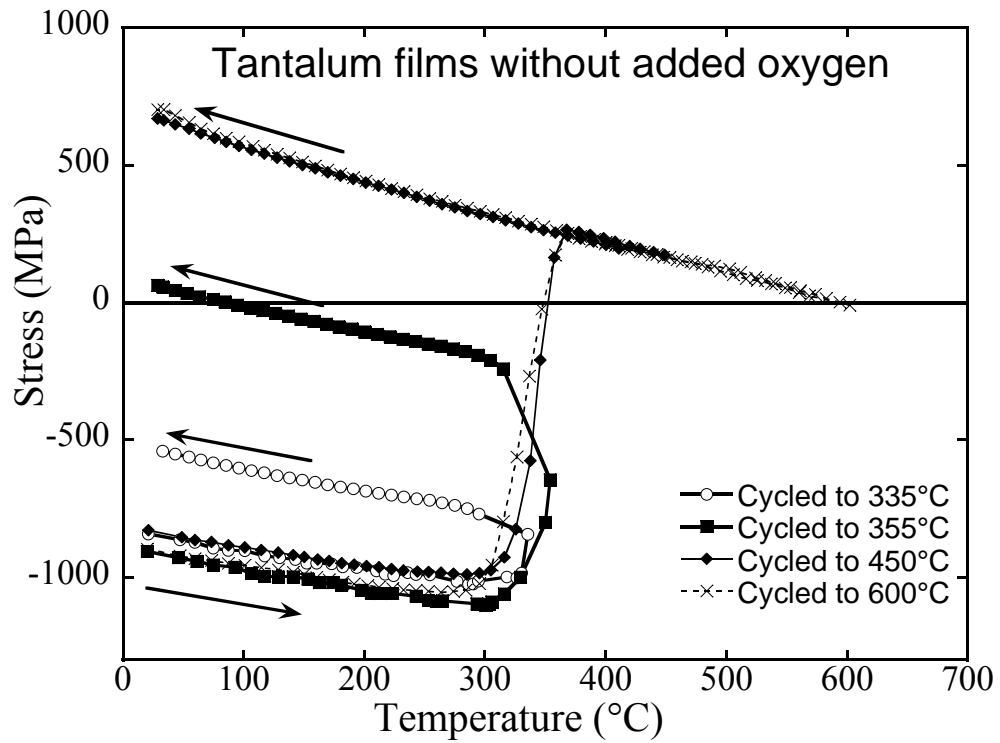


Figure 3.2: Thermomechanical behavior of 350 nm Ta films cycled to 335°, 355°, 450°, and 600°C deposited and cycled in a deposition system with $< 2 \times 10^{-9}$ Torr base pressure. The stress jump is associated with the β - α phase transformation and occurs at much lower temperatures than in previous reports based on oxygen-containing films (e.g. Fig. 3.1b).

Symmetric θ - 2θ x-ray scans of an as-deposited film and each of the films shown in Figure 3.2 are shown in Figure 3.3 (limited to $30^\circ \leq 2\theta \leq 80^\circ$, as all observed peaks were within this range). The as-deposited film was found to be strongly textured β phase with reflections detected only from grains having (001) planes parallel to the plane of the film. After annealing to different temperatures, the x-ray data illustrate that the strongly oriented (002) β phase is gradually replaced by a less well-oriented α phase between 300 and 375°C.

Since the β phase is so well oriented and only the (002) peak is evident, analysis of this peak was performed to determine the fraction of the film that had phase-transformed after cycling to different temperatures. The volume under the (002) β peak, obtained as described in Section 3.3.3, for films that had been thermally cycled, V_{cycled} , was compared to the peak volume of the as-deposited film, V_{as-dep} . The ratio V_{cycled}/V_{as-dep} gives a quantitative estimate of the amount of material that has phase-transformed that is insensitive to small variations in the sharpness of the texture from sample to sample (full widths at half maximum for rocking curves of the (002) peaks ranged from about 5°–8°). These data are shown in Figure 3.4 as a function of maximum cycling temperature, and confirm that the change in stress shown in Figure 3.2 is directly related to the phase transformation from β to α .

A significant amount of grain growth occurs during thermal cycling as well. The as-deposited film has a grain size of ~ 50 nm, as determined by Scherrer analysis of the (002) β x-ray peak width. After thermal cycling, the microstructure of the phase-transformed films is very unusual, exhibiting gradual changes in crystal orientation and few well-defined grains. Details of this structure can be found elsewhere [33]. In the phase-transformed films, an average spacing between high-angle grain boundaries of $\sim 1.8 \mu\text{m}$ has been determined from EBSD line scans [33].

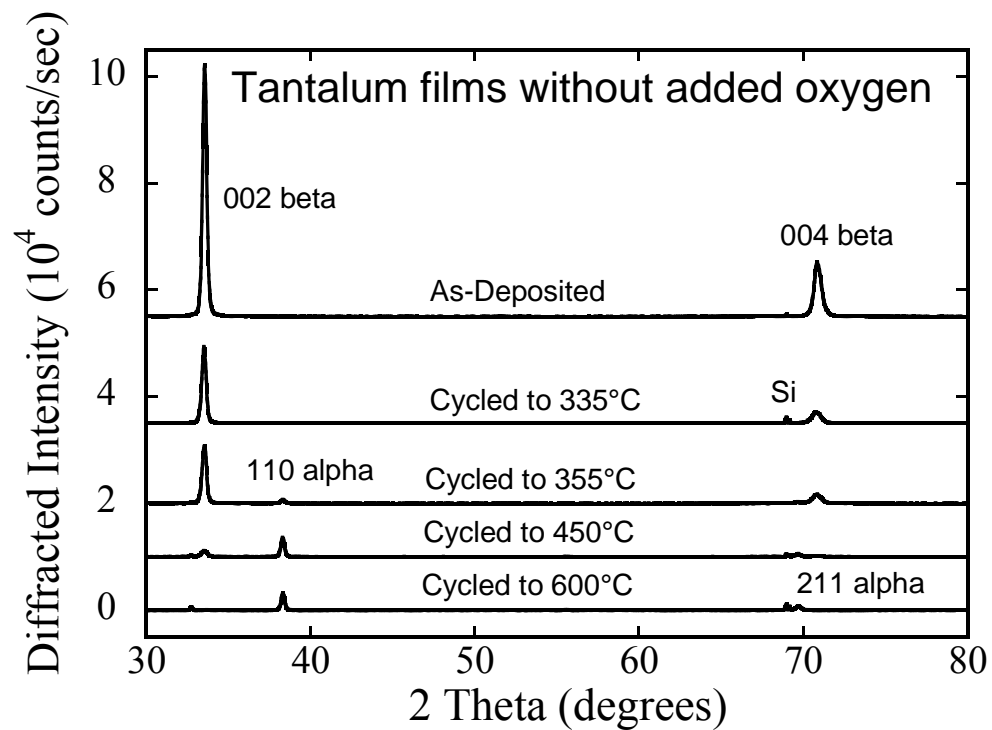


Figure 3.3: Theta-theta x-ray scans of 350 nm Ta films (a) as-deposited, and after thermal cycling to (b) 335°C, (c) 355°C, (d) 450°C, and (e) 600°C in ultra high vacuum. The as-deposited film shows a strong (002) β phase texture. The films show a gradual transformation from β to α with increasing cycling temperature. The film cycled to 600°C has completely phase transformed.

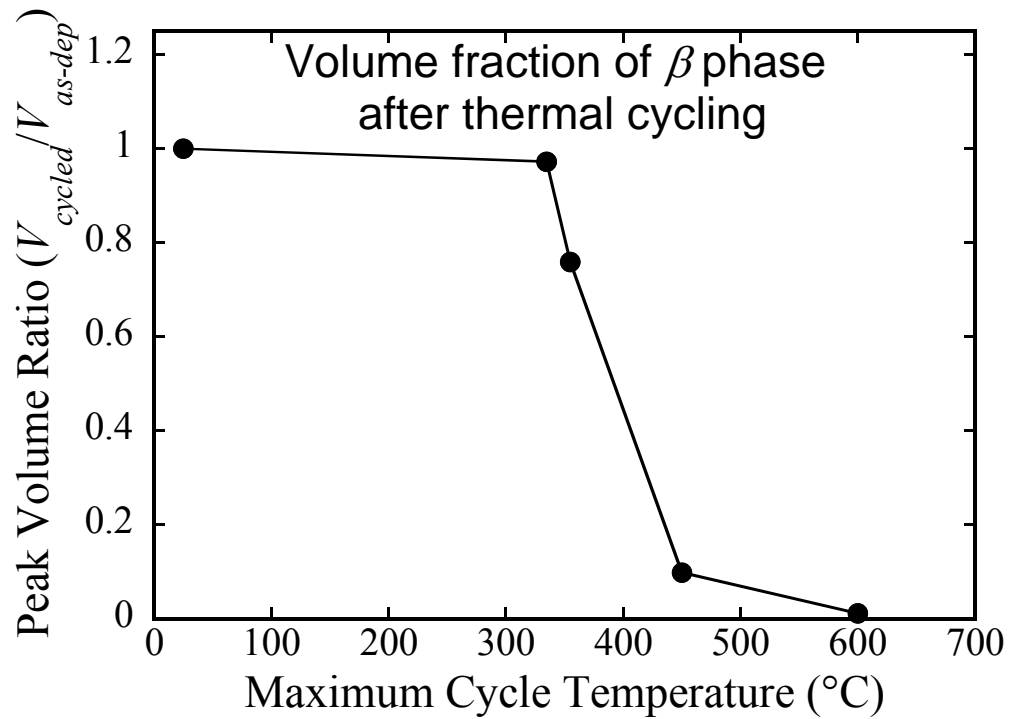


Figure 3.4: Plot of the x-ray peak volume ratio, $V_{\text{cycled}}/V_{\text{as-dep}}$, of the (002) β peak after thermally cycling to various temperatures. This ratio gives a quantitative estimate of the volume fraction of β phase remaining. The temperature range over which the volume fraction of β decreases coincides with the large increase in stress shown in Figure 3.2.

3.4.2 Discussion

The stress-temperature behavior shown in Figure 3.2 is very different from previously published results from Ta thin films (*e.g.* Figure 3.1). Not only are the increases in compressive stress associated with the incorporation of oxygen not seen, but the phase transformation occurs at much lower temperatures, supporting the idea that oxygen inhibits the phase transformation. As these results are free from the influence of oxygen, several conclusions can be drawn about both the origins of the stress change and the mechanism of the β - α phase transformation.

The large changes in stress that accompany the phase transformation in Figure 3.2 can be explained on the basis of densification and possibly changes in the elastic constants that accompany the phase transformation. Changes in film density may arise both from the difference in densities of the β and α phases and from grain growth. A theoretical density of $\rho_\beta = 16.33 \text{ g/cm}^3$ has been reported for the β phase [7, 34], while a density of $\rho_\alpha = 16.65 \text{ g/cm}^3$ has been reported for the α phase [35]. To calculate stress changes, the elastic constants must be known. Unfortunately, elastic constants of β -Ta have apparently not been reported. Thus, as a first approximation, we assume that the elastic constants of the α and β phases are identical and use the simple isotropic polycrystalline average elastic constants of the α phase ($E = 185 \text{ GPa}$, $\nu = 0.28$). Assuming a uniform dilatation,

$$e_T = \frac{\rho_\alpha - \rho_\beta}{\rho_\alpha}, \quad (3.1)$$

the increase in density due to the β - α phase transformation leads to a change in stress, $\Delta\sigma$, that can then be written as:

$$\Delta\sigma = -\frac{E}{1-\nu} \left(\frac{e_T}{3} \right). \quad (3.2)$$

Using the values of E , ν , and e_T described above, a change in stress of about 1.8 GPa in the tensile direction is calculated to occur in transforming a film completely from β to α .

Further increases in density arise from the removal of excess volume associated with grain boundaries during grain growth. Again assuming the elastic constants of the α and β phases to be the same, this relationship can be written as:

$$\Delta\sigma = -\frac{E}{1-\nu}\delta\left(\frac{1}{d_1} - \frac{1}{d_o}\right), \quad (3.3)$$

where δ is the average excess volume per unit area of the grain boundary, and d_o and d_1 the initial and final grain sizes, respectively (for a similar development, see Thompson and Carel [36]). Using $\delta = 1 \text{ \AA}$ and the experimentally obtained values $d_o = 50 \text{ nm}$ and $d_1 = 1.8 \text{ }\mu\text{m}$, an additional change in stress of $\sim 500 \text{ MPa}$ in the tensile direction is obtained.

Counting only the change in crystal structure and grain growth, the maximum total change in stress during the thermal cycle is predicted to be about 2.3 GPa in the tensile direction, which, given the coarseness of these estimations, is in reasonable agreement with the experimentally observed value of 1.6 GPa. Of course, the room temperature stress in the film would also be affected by changes in the elastic constants between the β and α phases, which we have neglected. We note that the thermoelastic slope during heating when the film is in the β phase is about half that during cooling when the film is in the α phase. This difference could, in principle, arise if the thermal expansion coefficient of α were twice that of β while the elastic constants were the same, or if α were twice as stiff as β while the expansion coefficients were the same. In reality, it is likely that both the expansion coefficients and the elastic constants of α and β are different.

As described in the Introduction, there has been much confusion regarding the mechanism of the β - α phase transformation. Our results show that the phase transformation occurs by a nucleation and growth process. While it has been speculated that the transformation could be martensitic [21], a shear transformation cannot account for the large changes in grain size (from ~ 50 nm to ~ 1.8 μm) that we observe. Furthermore, the rate of the phase transformation is strongly temperature dependent and shows no discernable dependence on the applied stress.

Both nucleation and growth are thermally activated. Since no composition change is associated with the simple polymorphic phase transformation in pure Ta, no long-range diffusion is required. If nuclei are present, then growth occurs by the motion of atoms hopping across the β/α interface. That is, growth is interface controlled. In Figure 3.2, the stress change—which is correlated with the phase transformation on the basis of Figure 3.4 and the arguments above—begins in earnest at about 300°C on heating. It is not possible to tell from the heating curve whether the phase transformation begins at this temperature due to the onset of nucleation or of growth. However, it is evident from the films cycled to 335 and 355°C that the phase transformation stops when the temperature drops below 300°C, although there is clearly α phase present. Thus, it is apparent that kinetic limits on boundary motion prohibit the phase transformation at temperatures below 300°C, and that nucleation is not limiting for the pure Ta films.

The fact that the transformation is kinetically limited is further evidenced by the time it takes to complete the transformation (~ 10 minutes at 2 minutes per data point in Figure 3.2). A simple analysis shows that interface-controlled boundary migration is reasonable at these temperatures. Using a model similar to that described by Porter and Easterling [37] for thermally activated migration of grain boundaries, the net flux of atoms from a β phase grain to a neighboring α phase grain, J_{net} , can be given by:

$$J_{net} = n\omega \exp\left(-\frac{\Delta G_a}{RT}\right) \left[1 - \exp\left(-\frac{\Delta G}{RT}\right)\right], \quad (3.4)$$

where n is the number of atoms per unit area (which can be estimated from the atomic density), ω the vibrational frequency of the atoms (\approx the Debye frequency), ΔG_a the activation energy for an atom jumping across the boundary, ΔG the driving force for the transformation, R the gas constant, and T the absolute temperature. While the driving force for the phase transformation is unknown, we can obtain a lower bound by observing that, while the strain energy density in the film is quite large ($\sim 2.5 \times 10^6$ J/m³ or ~ 28 J/mol, as determined from isotropic polycrystalline elastic constants and the measured stress) before the transformation begins, the transformation does not slow down as this driving force is reduced to zero. This suggests that the change in energy density associated with the phase transformation is at least of a similar magnitude. As this quantity is much smaller than RT , Equation 3.4 can be approximated by:

$$J_{net} = n\omega \frac{\Delta G}{RT} \exp\left(-\frac{\Delta G_a}{RT}\right). \quad (3.5)$$

If the boundary is moving at a speed v (estimated at ~ 1 nm/sec at 350°C from the transformation time and final grain size), the net flux must also be equal to v/V_a , where V_a is the atomic volume. Thus, the boundary speed can be written as a function of temperature, giving:

$$v = V_a n\omega \frac{\Delta G}{RT} \exp\left(-\frac{\Delta G_a}{RT}\right). \quad (3.6)$$

Using our estimates for the boundary speed and the lower bound of the driving energy of the phase transformation, along with the experimentally observed transformation temperature, we determine a lower bound on the activation energy of ~ 100 kJ/mol. While this simple model neglects many other factors that can influence boundary mobility, such as crystal orientation or boundary angle (for a review, see Gottstein *et al.* [38]), the activation energy we calculate is reasonable. 100 kJ/mol is roughly 25% the

reported activation energy for lattice diffusion and half that of typical estimates for grain boundary diffusion. These values correspond well with the trends found in molecular dynamics simulations of Schonfelder *et al.* [39, 40]. Note that Equation 3.6 predicts that boundary velocity will increase rapidly with temperature, rising by an order of magnitude for an increase in temperature from 300 to 400°C.

3.5 Films exposed to oxygen

Films exposed to oxygen have very different behaviors compared to those deposited and tested in UHV. In fact, the thermomechanical behavior differs significantly depending on whether oxygen was added during deposition, during thermal cycling, or between deposition and cycling.

3.5.1 Oxygen incorporated during deposition

3.5.1.1 Oxygen content

The oxygen content in a film is often seen to vary monotonically with oxygen partial pressure during deposition. For tantalum films in particular, several studies have shown oxygen content to vary in a roughly linear fashion with partial pressure over a wide range of deposition conditions and oxygen partial pressures [11, 41, 42]. A simple calculation gives the number of oxygen atoms incorporated into the film, N , as:

$$N = 2J_{ox}St, \quad (3.7)$$

where J_{ox} is the impingement rate of oxygen, S the sticking coefficient, and t the deposition time (the factor of 2 is due to the number of oxygen atoms in a molecule of oxygen gas). The impingement rate of oxygen can be calculated from the well-known Knudsen equation:

$$J_{ox} = \frac{N_A P_{ox}}{\sqrt{2\pi MRT}}, \quad (3.8)$$

where N_A is Avagadro's number, P_{ox} the partial pressure of oxygen, and M the molecular weight. Data from Gerstenberg and Calbick [41] for deposition in similar partial pressures of oxygen to those used in this work indicate that the sticking coefficient is approximately 0.01. The concentration of oxygen, C_{ox} , in the film can then be calculated from:

$$C_{ox} = \frac{2J_{ox}S}{J_{Ta} + 2J_{ox}S}, \quad (3.9)$$

where J_{Ta} is the flux of depositing tantalum atoms (determined from the deposition rate). Using this approach, we estimate the concentration of oxygen in our films as shown in Table 3.1, with values ranging from 0.6–5.2 at.%. For these samples, oxygen was expected to be distributed uniformly through the film thickness prior to thermal cycling in UHV.

3.5.1.2 Thermomechanical results

The σ - T behaviors of films into which oxygen was incorporated during deposition is shown in Figure 3.5. Films with small amounts of added oxygen (partial pressures during deposition less than 1.7×10^{-6} Torr) show the same behavior as films deposited without added oxygen. However, this behavior begins to change as oxygen content increases, with higher concentrations leading to higher transformation temperatures. In the film deposited with 4.6×10^{-6} Torr of oxygen, the phase transformation appears to take place in two distinct jumps, one between about 350 and 400°C and another at about 525 to 550°C. The jump in stress occurs entirely at $\sim 600^\circ\text{C}$ in the film deposited with 8.1×10^{-6} Torr of oxygen. When the partial pressure of oxygen is increased beyond this to 1.5×10^{-5} Torr, no jump in stress is observed at all in thermal cycling to 700°C, indicating that this film did not undergo phase transformation (confirmed by x-ray diffraction).

Table 3.1: Summary of data for films with oxygen incorporated during deposition: oxygen partial pressure during deposition, estimated oxygen concentration in the film, C_{ox} , estimated lower bound of activation energy for phase boundary motion, ΔG_a , and additional tensile stress due to oxygen leaving the film during the phase transformation.

P_{O_2} (10^{-6} Torr)	Estimated C_{ox} (at. %)	Estimated ΔG_a (kJ/mol)	Additional Tensile Stress (MPa)	Oxygen Leaving Film (at.%)	Remaining Oxygen (at.%)
1.7	0.6	96	0.6
2.5	0.9	96	0.9
4.6	1.7	121	300	0.6	1.1
8.1	2.9	136	500	1.1	1.8
15	5.2	146	5.2

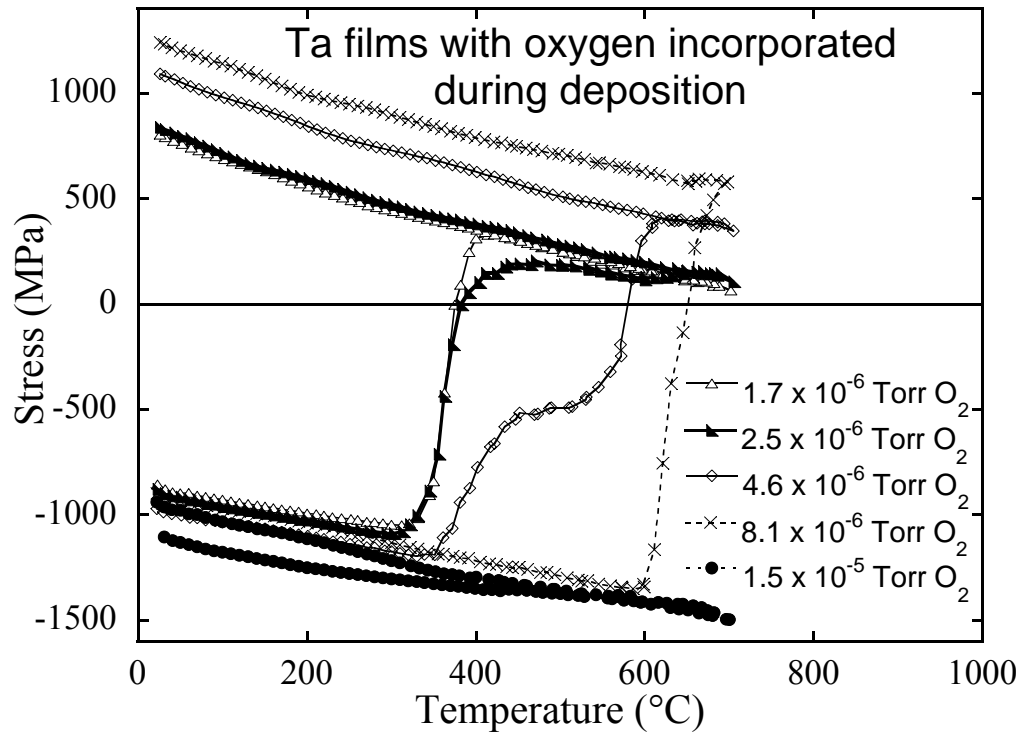


Figure 3.5: Stress-temperature behavior of Ta films deposited in partial pressures of oxygen ranging from 1.7×10^{-6} Torr to 1.5×10^{-5} Torr. The shift in the stress jump to higher temperatures with increasing oxygen pressure arises from solute drag on α/β phase boundaries. At the highest oxygen content, no jump occurs when cycling the film between room temperature and 700°C .

Phase-transformed films with oxygen added during deposition exhibited poor adhesion compared to oxygen-free films. Adhesion in these films worsened with increasing oxygen content, and films deposited with higher oxygen partial pressures would often delaminate from their substrates when samples were cleaved in preparation for microstructure analysis or when left exposed to atmosphere for several hours. In addition, the magnitude of the jump in stress is significantly greater in films deposited with high oxygen concentrations when compared to other phase-transformed films.

3.5.1.3 Discussion

The data in Figure 3.5 clearly show that the degree of inhibition of the phase transformation is systematically related to oxygen content. It is not immediately clear from these data, however, whether this is due to oxygen inhibiting the nucleation of the α phase, the growth process, or both. The key to our interpretation of these data lies in the oxygen concentration and mobility. The solubility of oxygen in the bulk α phase is 1.4% at 600°C [43]. The solubility of oxygen in the β phase is unknown, but is presumably similarly low at these low homologous temperatures. Yet Steidel and Gerstenberg [44] found that as-deposited tantalum films in either phase would retain their crystal structure while absorbing up to 12 at.% of oxygen during annealing, and Cabral *et al.* [17] measured an oxygen content higher than 10 at.% in β phase films after repeated thermal cycling to 400°C. At equilibrium, such high concentrations are only possible if the oxygen is contained in the grain boundaries. For comparison, a rough calculation assuming that one monolayer of oxygen fills all grain boundaries in a material with 50 nm grains leads to ~ 10 at.% oxygen, indicating that the grain boundary capacity in the as-deposited films is more than sufficient to contain the oxygen incorporated into our films (Table 3.1).

While the small grain size of the as-deposited films in the present study allows much more oxygen to be incorporated than would be thermodynamically favorable in the bcc lattice, the phase-transformed film has a much larger grain size ($\sim 1.8 \mu\text{m}$ [33]) and many fewer grain boundaries, so it cannot support such high oxygen concentrations. Thus, for the transformation to proceed by phase boundary motion, excess oxygen at the boundaries must be swept along with the transformation front, removed to the top or bottom interfaces, or left behind in the transformed film.

It is well known that the motion of a grain or phase boundary can be impeded by impurities through solute drag. This process is described in detail elsewhere [45-50] but can be summarized as follows. Impurities that segregate to low energy locations in boundaries will be left behind if the boundary starts to move without them. The boundary then exerts an attractive force on the impurity atoms that induces them to diffuse in the direction the boundary is moving. The impurities, in turn, exert a force on the boundary, slowing its movement to an extent dependent on the impurity concentration. Thus, a higher temperature is needed to obtain the same boundary velocity seen in impurity-free specimens, which is manifested as an increase in the activation energy for boundary motion [46, 50]. In addition, the presence of small amounts of impurities has also been observed to significantly reduce the nucleation rate in recrystallization experiments [45] and may do so in phase transformations as well.

Two features suggest that solute drag can account for the effect of oxygen on the β - α phase transformation. First, Cahn [46] and Lucke and Stuwe [47] predicted that solute drag would not inhibit boundary motion until a critical concentration of impurities is reached. This behavior is evident in Figure 3.5 where films with small amounts of oxygen behave nearly identically to films with no oxygen. Second, beyond the critical concentration, solute drag scales with impurity content and can slow boundary speed by many orders of magnitude [45-47], which may cause it to appear arrested.

This is consistent with the shift of the entire transformation to higher temperatures with increasing oxygen pressure during deposition seen in Figure 3.5. Using Equation 3.6, an estimate for the lower bound of the activation energy for each sample was determined as described in Section 3.4.2. An increase in ΔG_a is seen from ~ 100 kJ/mol in the film deposited with 1.7×10^{-6} Torr of oxygen to ~ 140 kJ/mol in the film with 8.1×10^{-6} Torr. These data, normalized by the activation energy determined for the oxygen-free films, are plotted in Figure 3.6. Temperatures used for this calculation were taken from the middle of the stress jump. For the film deposited with 4.6×10^{-6} Torr of oxygen, a temperature of 525°C was used, corresponding to the beginning of the higher temperature jump in stress. The increase in temperature necessary for the phase transformation to progress implies an increase in activation energy due to solute drag of more than 40%.

With knowledge of the concentration (Table 3.1) and mobility of oxygen in these films, all of the data shown in Figure 3.5 can be interpreted. The film deposited in 1.7×10^{-6} Torr of oxygen shows no effect, indicating that the concentration of oxygen is too low to cause substantial drag on the boundaries. The transformation in the film deposited in $P_{\text{ox}} = 2.5 \times 10^{-6}$ Torr starts at the same temperature but slows down near the end, presumably because oxygen builds up in the phase boundaries as they sweep through the film. Note that the oxygen concentration in both of these films is less than the equilibrium concentration in the α phase, so there is no requirement that oxygen be removed from the film.

For the film deposited in 4.6×10^{-6} Torr of oxygen, the start of the transformation is delayed, indicating that the oxygen concentration in the boundaries is now high enough to effect a small increase in activation energy. The fact that the transformation slows and then accelerates again may be due to the fact that oxygen accumulates in the boundaries as the boundaries sweep through the film. At first this slows the trans-

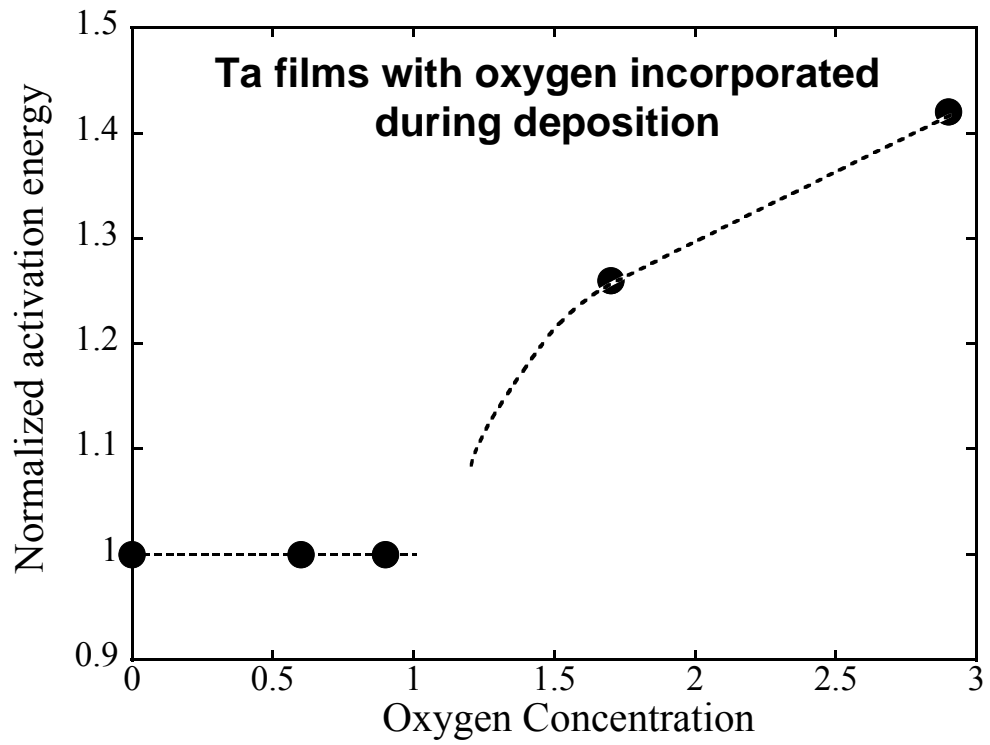


Figure 3.6: Change in activation energy for phase boundary motion normalized to that of an oxygen-free film as a function of calculated as-deposited oxygen content. The curve is a line to guide the eye and should not be interpreted as a functional form.

formation, but as the temperature increases, the transformation accelerates again. This slowing of the transformation also provides evidence that, even with the addition of oxygen to the film, the transformation is not limited by nucleation but by growth. This is further evidenced in the thermomechanical behavior of films exposed to oxygen between deposition and cycling, which will be discussed in Section 3.5.2.3.

Note that for the films with $P_{ox} = 4.6$ and 8.1×10^{-6} Torr, the initial oxygen concentration is greater than the equilibrium concentration in the α phase, suggesting that there is a driving force for oxygen to leave the film during the phase transformation. Indeed, the increased size of the stress jump during the phase transformation suggests that this happens. We estimated the amount of oxygen that would have to leave the film to produce the additional stress increment. To do so we assumed that dilatation scales linearly with oxygen content and used Cabral's result that the addition of 9 at.% oxygen leads to a 4.2% compressive dilatation [17]. From Equation 3.2, we estimate that approximately 0.6 and 1.1 at.% oxygen must leave the film during the phase transformation in the films with $P_{ox} = 4.6$ and 8.1×10^{-6} Torr, leaving 1.1 and 1.8 at.% oxygen in the transformed films, respectively. These values are summarized in Table 3.1. The calculated concentrations of oxygen remaining in these films are within 30% of the solubility limit (1.4 at.% at 600°C), remarkable agreement considering that no adjustable parameters were used in these calculations. This provides strong evidence that the increases in tensile stress in the films deposited with $P_{ox} = 4.6$ and 8.1×10^{-6} Torr arise from oxygen leaving the film during the transformation. One possible path for oxygen to leave the film is through the grain boundaries. While grain boundary diffusivity data for oxygen in tantalum have not been reported, it can be estimated from lattice diffusion data [51] by assuming that the activation energy for boundary diffusion is roughly half that of lattice diffusion [52]. Since the distances to the surface and film/substrate interface are short (100's of nm maximum) in these films and grain

boundary diffusion is fast (estimated diffusion distance over one second at 325°C is $\sim 1 \mu\text{m}$), grain boundary diffusion of oxygen is expected to play a significant role in this process. Oxygen expelled from the grain boundaries into to the film/substrate interface may account for the observed reduction of film adhesion with increased oxygen content as well.

For the film deposited in 1.5×10^{-5} Torr of oxygen, the oxygen concentration is such that the activation energy has increased to the point where the film does not transform at all during heating to 700°C. X-ray data confirm that only the β phase is present after thermal cycling indicating that the film's structure is stable up to these temperatures. It is interesting to note that, with an estimated C_{ox} of 5.2 at.% the grain boundaries in this film are still not near to being saturated with oxygen atoms (which would require an estimated $C_{ox} > 10$ at.%).

3.5.2 Oxygen exposure between deposition and testing

3.5.2.1 Oxygen content

Films exposed to oxygen immediately after deposition develop a thin passivating surface oxide layer, the thickness and composition of which may vary with the amount of oxygen to which the film is exposed. Unfortunately, a simple estimate based on impingement rate, J_{ox} , and sticking coefficient, S , as in Section 3.5.1.1 cannot be used to determine oxide thickness because S is expected to decrease rapidly with increasing oxygen surface coverage (in a manner similar to that observed for tantalum films exposed to nitrogen [11]). Nevertheless, the thickness of the oxide layer should scale (likely in a non-linear fashion) with the partial pressure of oxygen to which the film is exposed. As an upper bound, the native oxide thickness of tantalum films exposed to atmosphere has been reported as ~ 2 nm [24, 25]. Averaged over a 350 nm thick film,

this corresponds to an oxygen concentration of ~ 0.6 at.%, well below the solubility limit in bcc tantalum.

3.5.2.2 Thermomechanical results

In comparison to films in which oxygen was incorporated during deposition (Figure 3.5), films exposed to oxygen between deposition and thermal cycling show different thermomechanical behavior, as seen in Figure 3.7. Up to about 350°C , these films behave as the oxygen-free films (Figure 3.2). However, from $\sim 350^\circ\text{C}$ to the end of heating, the σ - T behavior depends on the amount of oxygen to which the film has been exposed. When exposed to very small amounts (0.15 mTorr), the film behaves identically to the films without oxygen. When exposed to greater amounts, the phase transformation is arrested at about 350°C and is completed at a higher temperature as indicated by a second jump in stress. With increasing oxygen exposure, the magnitude of the stress jump from 300 – 350°C is lessened slightly, and the secondary jumps in stress occur at higher temperatures. X-ray analysis indicated that all of these films had completed the phase transformation after cycling ($V_{\text{cycled}}/V_{\text{as-dep}} \approx 0.005$ in all films).

3.5.2.3 Discussion

As in Section 3.5.1.3, these results can be understood on the basis of the oxygen content and mobility in the film. It has been observed that a thin layer of tantalum oxide will dissociate and be dissolved into a sufficiently thick tantalum substrate when annealed under high vacuum conditions at temperatures above $\sim 375^\circ\text{C}$ [26], and we attribute the thermomechanical behavior shown in Figure 3.7 to this phenomenon. Up to $\sim 350^\circ\text{C}$, these films behave like the films shown in Figure 3.2, as the tantalum layers themselves are initially oxygen-free. However, oxygen from the oxide layer diffuses into the tantalum film, and the phase transformation is arrested when the grain

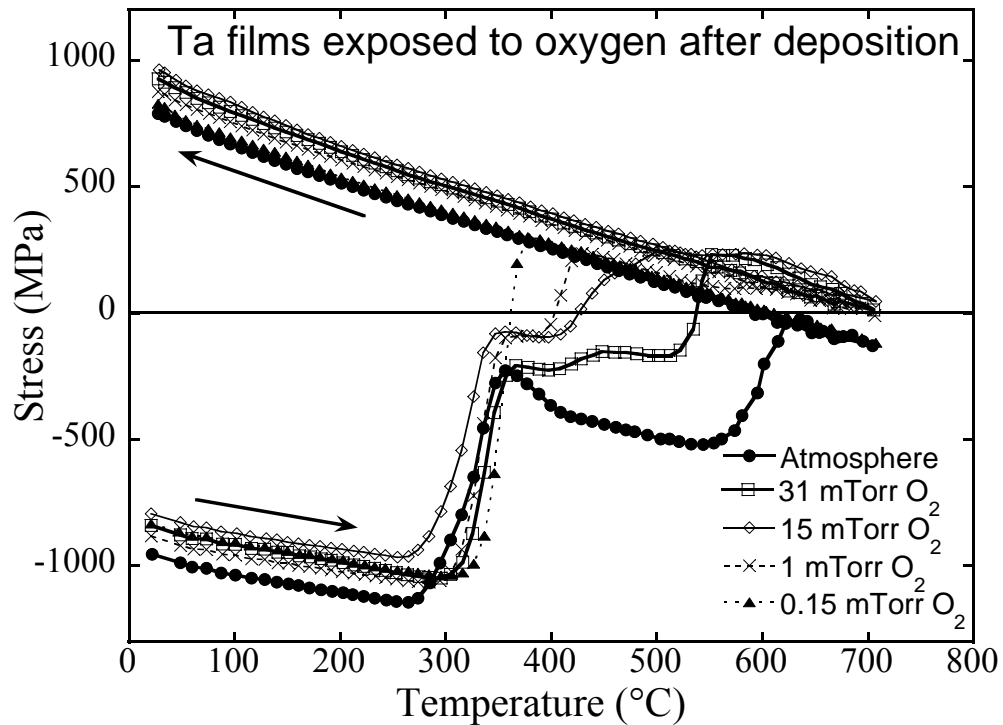


Figure 3.7: Stress-temperature behavior of Ta films exposed to various amounts of oxygen between deposition and thermal cycling to form an oxide layer. The phase transformation is arrested when the oxygen from the oxide layer diffuses into the film. While the total stress change remains essentially constant, higher temperatures are needed to complete the transformation as the film is exposed to greater amounts of oxygen.

boundary oxygen content becomes high enough for solute drag to be effective. At higher temperatures, the films in Figure 3.7 behave more like those in Figure 3.5, with the phase transformation shifted to higher temperatures due to the increasing activation energy for boundary motion. It is interesting to note that, in the film exposed to atmosphere, the stress changes in the *compressive* direction immediately following the first tensile stress jump. This suggests that, in this film, there is sufficient oxygen diffusing from the surface into the film to expand the equilibrium in-plane lattice parameter as described by Cabral *et al.* [17] (Figure 3.1a). Interestingly, the total change in stress over the first thermal cycle is independent of the oxygen exposure, confirming that the total oxygen content in all of these films is less than the solubility limit in the transformed films and no oxygen had to be removed from the film to accomplish the phase transformation.

An important result of this set of experiments is that the data in Figure 3.7 provide clear evidence that solute drag alone can stop the phase transformation. Since a substantial fraction of the film has already transformed to the α phase after the initial jump in stress, it is again evident that nucleation is not the limiting factor.

3.5.3 Oxygen incorporated during thermal cycling

3.5.3.1 Oxygen content

Tantalum films exposed to oxygen during thermal cycling will absorb oxygen from the atmosphere at elevated temperatures in a manner similar to that described by Cabral *et al.* [17]. In addition, the solubility, diffusivity, and absorption rate of oxygen in Ta all increase dramatically as the temperature increases (the latter because the oxygen pressure, and thus the impingement rate, increases with temperature.) This case is unlike the previous two in that the supply of oxygen is not limited to that deposited in the film or contained in the surface oxide. The amount of oxygen absorbed

during thermal cycling will depend greatly on the oxygen partial pressure in the atmosphere and the temperature history experienced during thermal cycling. With high enough oxygen pressures, temperatures, and times, the film will completely oxidize and form Ta_2O_5 [20]. While we did not attempt to calculate the oxygen content of films cycled in an oxygen-containing atmosphere, the dynamics of oxygen incorporation can be used to understand the behavior of these films.

3.5.3.2 Thermomechanical results

Representative results for a film into which oxygen was incorporated during thermal cycling are shown in Figure 3.8. The film starts off at about 700 MPa in compression and follows a thermoelastic slope until about 250°C. From ~ 250 to ~300°C, the slope of the curve deviates from the thermoelastic line, leading to even greater compressive stresses. From about 300–350°C, there is a rapid change in stress in the tensile direction of several hundred MPa, but this jump stops, and from 350–500°C, the stress changes in the compressive direction with a steeper slope than before. Above 500°C, the slope gradually becomes more positive until we see large changes in stress above 600°C, with an overall change of ~ 2 GPa in the tensile direction. Note that the maximum slope here, about 13 MPa/°C, is much lower than the maximum slopes, about 20 MPa/°C, seen in Figs. 3.2, 3.5, and 3.7. Upon cooling, the rate of increase in tensile stress is greater than the thermoelastic slope down to about 600°C, after which the thermoelastic slope is followed. This curve exhibits features similar to those reported by Clevenger *et al.* [21].

3.5.3.3 Discussion

When a film is exposed to oxygen in this manner, an increase in temperature generates a competition between the incorporation of oxygen, which increases the activation

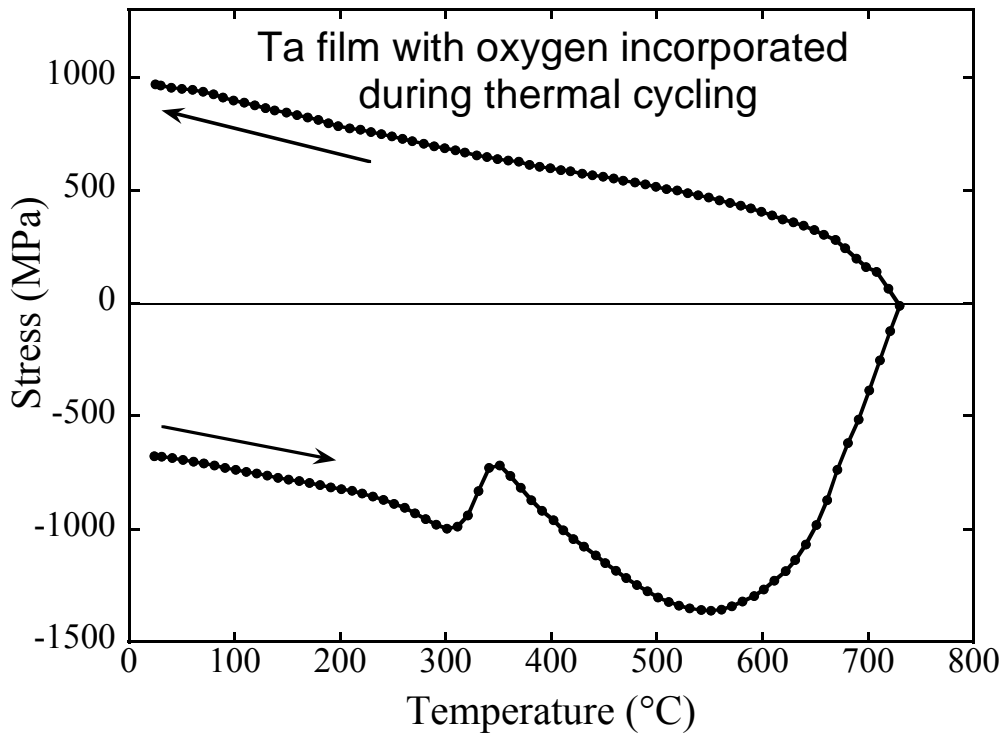


Figure 3.8: Stress-temperature behavior of a ~ 350 nm Ta film thermally cycled in an atmosphere containing $\sim 10^{-5}$ Torr oxygen. As temperature increases, there is a competition between oxygen incorporation (leads to higher activation energies for boundary motion, inhibiting the phase transformation and causing increased compressive stresses) and the increase in thermal energy (allows the β - α phase transformation to progress, causing increased tensile stresses). Note the shape of the curve is similar to that reported by Clevenger *et al.* [21] (Fig. 3.1b).

energy, ΔG_a (Figure 3.6), and inhibits the phase transformation, and the increase in thermal energy, RT , available to facilitate phase boundary motion which accelerates the phase transformation (see Equation 3.6). Since the incorporation of oxygen leads directly to more compressive stresses and the phase transformation to more tensile stresses, the outcome can easily be seen in the thermomechanical behavior. The film is likely to develop a thin oxide layer on its surface as heating commences, due to the long period of exposure to the oxygen-containing atmosphere. The initial deviation from the thermoelastic line occurs in the temperature range reported for the onset of oxygen incorporation into Ta films [11, 44, 53-55], causing a change in stress as described by Cabral *et al.* [17] (Figure 3.1a). The subsequent stress jump occurs at the same temperature as the β - α phase transformation takes place in the oxygen-free films (Figure 3.2), indicating that the transformation is briefly able to progress. But this stress jump is arrested after a few hundred MPa as oxygen dissolves into the film at an increased rate as the oxide layer starts to dissociate as described in Section 3.5.2.3 and stops the phase transformation through solute drag, similar to the films shown in Figure 3.7. Above 350°C, incorporation of oxygen gradually gives way to phase transformation and the slope of the stress-temperature data becomes more and more positive. The majority of the phase transformation takes place over 600°C, and the low transformation rate (compared with Figures 3.2, 3.5, and 3.7) can be attributed to the continuing uptake of oxygen.

These data look very similar to those of Clevenger *et al.* [21] (Figure 3.1b), suggesting that while the partial pressure of oxygen was not specified in those experiments, the oxygen content in their test atmosphere was similar. In this light, we reinterpret several of Clevenger *et al.*'s conclusions. They attributed the initial deviations from thermoelastic behavior to changing elastic constants. We find no evidence for this and are able to explain the results quantitatively on the basis of oxygen incorpora-

tion. They attributed the change in the stress-temperature slope to more positive values above 600°C (Figure 3.1b) to plasticity. We think this is the phase transformation starting to dominate. In addition, partial phase transformation events would account for the stress jumps at ~ 400°C that Clevenger *et al.* observed, but could not explain. Note that our interpretations can be applied only to films deposited under similar conditions; Clevenger *et al.* deposited films using a variety of different conditions (applied substrate bias and sputtering pressures) and obtained a wide range of thermomechanical behaviors. We make no attempt to explain their data for films deposited using conditions other than ours, as such films are likely to have significant differences in orientation, phase formation, and porosity [3, 56] that are not accounted for in the current analysis.

3.6 Summary and Conclusions

Tantalum films were deposited in the metastable β phase in an ultra-high vacuum (UHV) deposition system with control over the oxygen content in the film. Films were thermally cycled *in situ* and the effects of oxygen incorporation on the transformation to the stable α phase were investigated. Films deposited and tested without added oxygen reveal very different thermomechanical behavior from those published previously, suggesting that the films in prior studies were affected by oxygen contamination. In particular, in oxygen-free films the phase transformation occurs at a much lower temperature (300–400°C). Furthermore, the phase transformation is time- and not stress-dependent and is accompanied by significant grain growth. Thus, we conclude that the transformation takes place by a nucleation and growth process that is not limited by nucleation, but by growth. When films are exposed to oxygen, the phase transformation is shifted to higher temperatures in a way that is consistent with the inhibition of boundary motion due to solute drag: small amounts of oxygen have no

discernable effect, but larger oxygen concentrations can significantly delay the transformation. In addition, the thermomechanical behavior depends not only on the amount of oxygen to which the films are exposed, but also on how the exposure takes place. For films in which oxygen was incorporated during deposition, the transformation temperature is shifted to higher temperatures depending on oxygen content. For films with a surface oxide layer, the transformation starts at the same temperature as in oxygen-free films, but is arrested until higher temperatures when the oxide layer dissociates and the oxygen diffuses into the grain boundaries. Films cycled in oxygen see the competing effects of oxygen incorporation, which inhibits the phase transformation by increasing the activation energy for boundary motion and leads to compressive stresses, and the increase in thermal energy, which allows the phase transformation to progress and leads to tensile stresses. The total measured change in stress accompanying the phase transformation is in reasonable agreement with that predicted from changes in density due to the change in crystal structure, grain growth, and change in oxygen concentration. It is evident that through control of the oxygen content, the β - α phase transformation can be controlled, making it possible to more easily produce patterned α phase structures as well as more stable β phase films.

3.7 Acknowledgements

Primary support for this work was provided by the U.S. Department of Energy under grant number DE-FG02-02ER46001. This support, however, does not constitute an endorsement by DOE of the views expressed in this article. This work made use of the x-ray and ion beam facilities of the Cornell Center for Materials Research (CCMR) with support from the National Science Foundation Materials Research Science and Engineering Centers (MRSEC) program (DMR-0079992). Portions of the work were supported by the U.S. Department of Education (GAANN Fellowship award

P200A000800-02), the National Science Foundation (CAREER award DMR-9875119), the Office of Naval Research (Grant No. N00014-99-1-0650 DURIP), and by Cornell University.

REFERENCES

1. Westwood, W.D. and F.C. Livermore, *Phase composition and conductivity of sputtered tantalum*. Thin Solid Films, 1970. **5**, p. 407-420.
2. Feinstein, L.G. and R.D. Huttemann, *Factors controlling the structure of sputtered Ta films*. Thin Solid Films, 1973. **16**, p. 129-145.
3. Catania, P., R.A. Roy, and J.J. Cuomo, *Phase formation and microstructure changes in tantalum thin films induced by bias sputtering*. J. Appl. Phys., 1993. **74**(2), p. 1008-1014.
4. Hoogeveen, R., M. Moske, H. Geisler, and K. Samwer, *Texture and phase transformation of sputter-deposited metastable Ta films and Ta/Cu multilayers*. Thin Solid Films, 1996. **275**, p. 203-206.
5. Ino, K., T. Shinohara, T. Ushiki, and T. Ohmi, *Ion energy, ion flux, and ion species effects on crystallographic and electrical properties of sputter-deposited Ta thin films*. J. Vac. Sci. Technol. A, 1997. **15**(5), p. 2627-2635.
6. Read, M.H. and C. Altman, *A new structure in tantalum thin films*. Applied Physics Letters, 1965. **7**(3), p. 51-52.
7. Moseley, P.T. and C.J. Seabrook, *The crystal structure of β -tantalum*. Acta Cryst., 1973. **B29**, p. 1170-1171.
8. Arakcheeva, A., G. Chapuis, and V. Grinevitch, *The self-hosting structure of beta-Ta*. Acta Cryst., 2002. **B58**, p. 1-7.
9. Baker, P.N., *Preparation and properties of tantalum thin films*. Thin Solid Films, 1972. **14**, p. 3-25.
10. Schwartz, N., W.A. Reed, P. Polash, and M.H. Read, *Temperature coefficient of resistance of beta-tantalum films and mixtures with b.c.c.-tantalum*. Thin Solid Films, 1972. **14**, p. 333-347.
11. Westwood, W.D., N. Waterhouse, and P.S. Wilcox, *Tantalum Thin Films*. (Academic Press, London, 1975).
12. Kondo, K., M. Nakabayashi, K. Kawakami, T. Chijimatsu, M. Nakaishi, M. Yamada, M. Yamabe, and K. Sugishima, *Stress stabilization of β -tantalum and its crystal structure*. J. Vac. Sci. Technol. A, 1993. **11**, p. 3067-3071.
13. Yoshihara, T. and K. Suzuki, *Sputtering of fibrous-structured low-stress Ta films for x-ray masks*. J. Vac. Sci. Technol. B, 1994. **12**(6), p. 4001-4004.
14. Holloway, K. and P.M. Fryer, *Tantalum as a diffusion barrier between copper and silicon*. Applied Physics Letters, 1990. **57**(17), p. 1736-1738.

15. Clevenger, L.A., N.A. Bojarczuk, K. Holloway, J.M.E. Harper, C. Cabral, R.G. Schad, F. Cardone, and L. Stolt, *Comparison of high vacuum and ultra-high vacuum tantalum diffusion barrier performance against copper penetration*. J. Appl. Phys., 1993. **73**(1), p. 300-308.
16. Laurila, T., K. Zeng, and J.K. Kivilahti, *Effect of oxygen on the reactions in the Si/Ta/Cu metallization system*. J. Mater. Res., 2001. **16**(10), p. 2939-2946.
17. Cabral, C., L.A. Clevenger, and R.G. Schad, *Repeated compressive stress increase with 400 C thermal cycling in tantalum thin films due to increases in the oxygen content*. J. Vac. Sci. Technol. B, 1994. **12**(4), p. 2818-2821.
18. Wu, D.S., M.L. Lee, and T.Y. Lin, *Properties of multilayered thin films for thermal ink-jet printing devices*. Applied Surface Science, 1996. **92**, p. 626-629.
19. Wu, D.S., C.C. Chan, R.H. Horng, W.C. Lin, S.L. Chiu, and Y.Y. Wu, *Structural and electrical properties of Ta-Al thin films by magnetron sputtering*. Applied Surface Science, 1999. **144-145**, p. 315-318.
20. French, B.L. and J.C. Bilello, *In situ observations of the real-time stress-evolution and delamination of thin Ta films on Si (100)*. Thin Solid Films, 2004. **446**, p. 91-98.
21. Clevenger, L.A., A. Mutscheller, J.M.E. Harper, C. Cabral, and K. Barmak, *The relationship between deposition conditions, the beta to alpha phase transformation, and stress relaxation in tantalum thin films*. J. Appl. Phys., 1992. **72**(10), p. 4918-4924.
22. Kitchingman, W.J., *The atomic mechanism of the body-centered cubic to σ -phase transformation*. Acta Cryst., 1968. **A24**, p. 282-286.
23. Jiang, A., T.A. Tyson, and L. Axe, *The stability of the β -phase of tantalum: a molecular dynamics study*. J. Phys.: Condens. Matter, 2005. **17**, p. 1841-1850.
24. Mathieu, H.J., M. Datta, and D. Landolt, *Thickness of natural oxide films determined by AES and XPS with/without sputtering*. J. Vac. Sci. Technol. A, 1985. **3**(2), p. 331-335.
25. Kim, Y., J. Zhao, and K. Uosaki, *Formation and electric property measurement of nanosized patterns of tantalum oxide by current sensing atomic force microscope*. Journal of Applied Physics, 2003. **94**(12), p. 7733-7738.
26. Giber, J. and H. Oechsner, *Dissolution of anodic Ta₂O₅ layers into polycrystalline tantalum*. Thin Solid Films, 1985. **131**, p. 279-287.
27. Liu, L., H. Gong, Y. Wang, J. Wang, A.T.S. Wee, and R. Liu, *Annealing effects of tantalum thin films sputtered on [001] silicon substrate*. Materials Science and Engineering C, 2001. **16**, p. 85-89.
28. Shu, J.B., *Plastic deformation and thermomechanical behavior of passivated copper thin films on silicon substrates*, Ph.D. thesis, Cornell University, 2003.

29. Flinn, P.A., D.S. Gardner, and W.D. Nix, *Measurement and interpretation of stress in aluminum-based metallization as a function of thermal history*. IEEE Transactions on Electron Devices, 1987. **ED-34**(3), p. 689-699.
30. Nix, W.D., *Mechanical properties of thin films*. Metallurgical Transactions A, 1989. **20A**, p. 2217-2245.
31. Stoney, G., *The tension of metallic films deposited by electrolysis*. Proceedings of the Royal Society of London, 1909. **A82**, p. 172-175.
32. Scherrer, P., *Estimation of the size and structure of colloidal particles by Rontgen rays*. Nachrichten von der Koniglichen Gesellschaft der Wissenschaften zu Gottingen, Mathematisch-Physikalische Klasse, 1918. **2**, p. 96-100.
33. Knepper, R., R.S. Fertig, K. Jackson, and S.P. Baker, *Microstructure of phase-transformed tantalum thin films*. in preparation, 2007.
34. Jiang, A., A. Yohannan, N.O. Nnolim, T.A. Tyson, L. Axe, S.L. Lee, and P. Cote, *Investigation of the structure of β -tantalum*. Thin Solid Films, 2003. **437**, p. 116-122.
35. Feldman, L.C. and J.W. Mayer, *Fundamentals of surface and thin film analysis*. (PTR Prentice-Hall, Upper Saddle River, NJ, 1986).
36. Thompson, C.V. and R. Carel, *Stress and grain growth in thin films*. J. Mech. Phys. Solids, 1996. **44**(5), p. 657-673.
37. Porter, D.A. and K.E. Easterling, *Phase Transformations in Metals and Alloys*. 2nd ed. (CRC Press, London, 1992).
38. Gottstein, G., D.A. Molodov, and L.S. Shvindlerman, *Grain boundary migration in metals: recent developments*. Interface Science, 1998. **6**, p. 7-22.
39. Schonfelder, B., D. Wolf, S.R. Phillpot, and M. Furtkamp, *Molecular-dynamics method for the simulation of grain boundary migration*. Interface Science, 1997. **5**, p. 245-262.
40. Schonfelder, B., G. Gottstein, and L.S. Shvindlerman, *Comparative study of grain-boundary migration and grain-boundary self-diffusion of $[001]$ twist-grain boundaries in copper by atomistic simulations*. Acta Mater., 2005. **53**, p. 1597-1609.
41. Gerstenberg, D. and C.J. Calbick, *Effects of nitrogen, methane, and oxygen on structure and electrical properties of thin tantalum films*. Journal of Applied Physics, 1964. **35**(2), p. 402-407.
42. Westwood, W.D. and P.S. Wilcox, *Effect of substrate bias on tantalum films sputtered in an oxygen-argon mixture*. Journal of Applied Physics, 1971. **42**(10), p. 4055-4062.
43. Garg, S.P., N. Krishnamurthy, A. Awasthi, and M. Venkatraman, *The O-Ta (Oxygen-Tantalum) System*. Journal of Phase Equilibria, 1996. **17**(1), p. 63-77.

44. Steidel, C.A. and D. Gerstenberg, *Thermal oxidation of sputtered tantalum thin films between 100° and 525°C*. Journal of Applied Physics, 1969. **40**(9), p. 3828-3835.
45. Lucke, K. and K. Detert, *A quantitative theory of grain-boundary motion and recrystallization in metals in the presence of impurities*. Acta Metallurgica, 1957. **5**, p. 628-637.
46. Cahn, J.W., *The impurity-drag effect in grain boundary motion*. Acta Metallurgica, 1962. **10**, p. 789-798.
47. Lucke, K. and H.P. Stuwe, *On the theory of impurity controlled grain boundary motion*. Acta Metallurgica, 1971. **19**, p. 1087-1099.
48. Hillert, M., *Solute drag, solute trapping and diffusional dissipation of Gibbs energy*. Acta Mater., 1999. **47**(18), p. 4481-4505.
49. Hillert, M. and M. Schalin, *Modeling of solute drag in the massive phase transformation*. Acta Mater., 2000. **48**, p. 461-468.
50. Mendeleev, M.I. and D.J. Srolovitz, *A regular solution model for impurity drag on a migrating grain boundary*. Acta Mater., 2001. **49**, p. 589-597.
51. Lee, J.S. and C.J. Altstetter, *Thermodynamic studies of oxygen behavior in tantalum-based alloys*. Acta Metallurgica, 1986. **34**(1), p. 139-145.
52. Shewmon, P., *Diffusion in Solids*. 2nd ed. (The Minerals, Metals & Materials Society, Warrendale, PA, 1989).
53. Basseches, H., *The oxidation of sputtered tantalum films*. Journal of the Electrochemical Society, 1962. **109**(6), p. 475-479.
54. Sato, S., T. Inoue, and H. Sasaki, *Thermal oxidation of beta-Ta below 500°C*. Thin Solid Films, 1981. **86**, p. 21-30.
55. Lugomer, S., M. Kerenovic, M. Stipanovic, and S. Lekic, *Comparitive in situ study of tantalum thin film oxidation in isothermal and nonisothermal conditions*. Vacuum, 1988. **38**(1), p. 15-19.
56. Thornton, J.A., *High rate thick film growth*. Annu. Rev. Mater. Sci., 1977. **7**, p. 239-260.

Chapter 4

Driving force and activation energy for the β - α phase transformation in tantalum thin films

In the previous chapter, it was shown that the mechanism of the β - α phase transformation in tantalum thin films is a nucleation and growth process that is limited by growth, and an estimate of the activation energy as a function of oxygen content was presented based on a lower limit of the driving force that was determined from the change in strain energy during the phase transformation. It is expected that the driving force for the phase transformation is actually significantly larger than the strain energy, as the rate of the phase transformation appears to be unaffected by the stress in the film. Here, we directly measure the change in energy during the phase transformation using differential scanning calorimetry (DSC), giving us not only a much more accurate measure of the driving force of the transformation, but also allowing for a more accurate calculation of the activation energy necessary for the transformation to progress.

A tantalum film was sputter deposited in the metastable β phase onto (100) silicon wafers as described in Chapters 2 and 3 to a thickness of ~ 400 nm. Film thickness was determined using profilometry. Small pieces (~ 3 mm \times 3 mm) were cut from the film to be scanned in the DSC. Each piece was placed into an aluminum sample pan which was subsequently crimped shut. The DSC works by heating both the sample and a reference at the same constant rate in a nitrogen-purged atmosphere and measuring the power differential needed to maintain an identical heating rate. When energy is

given off or absorbed during a reaction (such as the β - α phase transformation), a peak or valley will appear in the DSC scan, with peaks indicating exothermic reactions and valleys endothermic reactions. With knowledge of the amount of material contributing to such a peak, the driving force for the phase transformation can be determined. As the β - α phase transformation typically does not take place at temperatures below $\sim 300^\circ\text{C}$, samples scanned in the DSC were heated quickly to 300°C and then at $10^\circ/\text{minute}$ from 300 – 430°C to measure the energy given off during the transformation.

As shown in Chapter 3, the transformation from β to α can be inhibited by the presence of oxygen in the film [1-3]. As the films scanned in the DSC were exposed to oxygen both from the air between deposition and testing and from residual oxygen in the atmosphere during thermal cycling in the DSC, it was expected that the film would not completely transform during testing. While it is difficult to gauge the amount of oxygen in the atmosphere during DSC testing, it is likely to be at least of the order of magnitude that Cabral *et al* [4] had in thermally cycling in a similar helium-purged atmosphere, and thus the film would be subject to substantial oxygen incorporation. In order to accurately gauge the driving force for the phase transformation, it was necessary to determine the quantity of material that underwent phase transformation in each sample. To do this, samples were scanned using x-ray diffraction in a General Area Detector Diffraction System (GADDS) both before and after cycling in the DSC. Each sample was exposed to the x-ray source for 2 minutes. Samples were aligned such that the (002) β peak from planes aligned parallel to the sample surface would illuminate the center of the GADDS CCD area detector. As the β phase is very strongly textured with a preferred (001) out-of-plane orientation, a comparison of the volumes of the (002) β x-ray peaks collected before and after cycling in the DSC was used to estimate the fraction of the film that had transformed during testing.

GADDS scans for a 400 nm tantalum film before and after DSC scanning are shown in Figure 4.1. While the sample shows a strong (002) β peak in both cases, additional α phase reflections are visible only after thermal cycling in the DSC. Note that the (202) β , (110) α , and (212) β peaks all appear within 1° in 2θ , and cannot be easily distinguished in GADDS. Peak volumes were determined from the total number of photons detected in a fixed angular range around the (002) β peak, as shown in Figure 4.1. The as-deposited film had an (002) β peak volume of 5.4×10^5 counts, which dropped to 5.0×10^5 after thermal cycling. The ratio of the peak volumes was taken as an indication of how much of the film had transformed, in this case, $\sim 7\%$.

The portion of the DSC scan in which an exothermic peak appears for the same 400 nm tantalum film is shown in Figure 4.2. As the film is thin, only a limited amount of material can be tested and the energy change, ΔE , is very small ($\sim 1.8 \times 10^4$ J). The driving force for the phase transformation, ΔG is given by:

$$\Delta G = \frac{M}{V\rho X} \Delta E, \quad (4.1)$$

where M is the atomic weight, X the fraction of the film that transforms, V the volume of film tested, and ρ the density. The film volume is determined from the measured dimensions of the sample, the atomic weight and density are taken from the literature, and the fraction of the film that transforms from the ratio of peak volumes as described above. From these data, the activation energy is estimated at ~ 5.7 kJ/mol, or roughly 200 times greater than the strain energy.

Despite the large difference between the driving force estimated in Chapter 3 and that determined from DSC measurements, the activation energies calculated from Equation (3.6) change only very little, increasing by $\sim 30\%$. While this difference is not substantial enough to greatly affect the qualitative comparisons to grain boundary and bulk diffusion made in Chapter 3, it will have a large impact on any quantitative

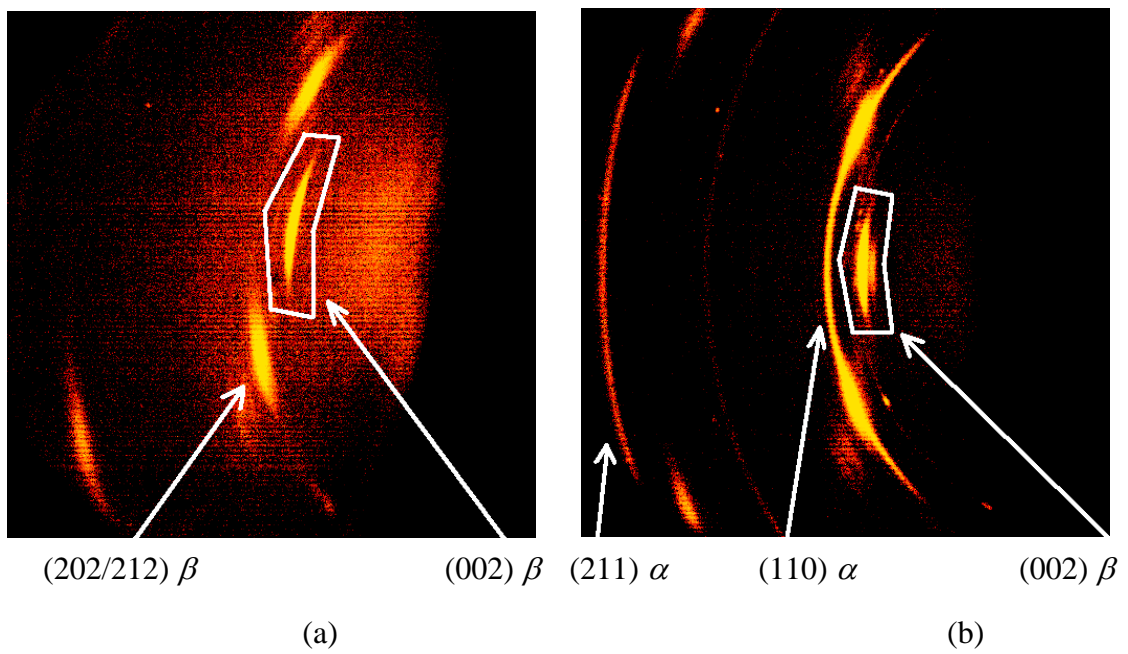


Figure 4.1: Images taken from GADDS x-ray scans of a 400 nm tantalum film (a) as-deposited in the β phase and (b) after scanning in the DSC. A comparison of the $(002) \beta$ peak volumes was used to determine how much of the film transformed during DSC experiments.

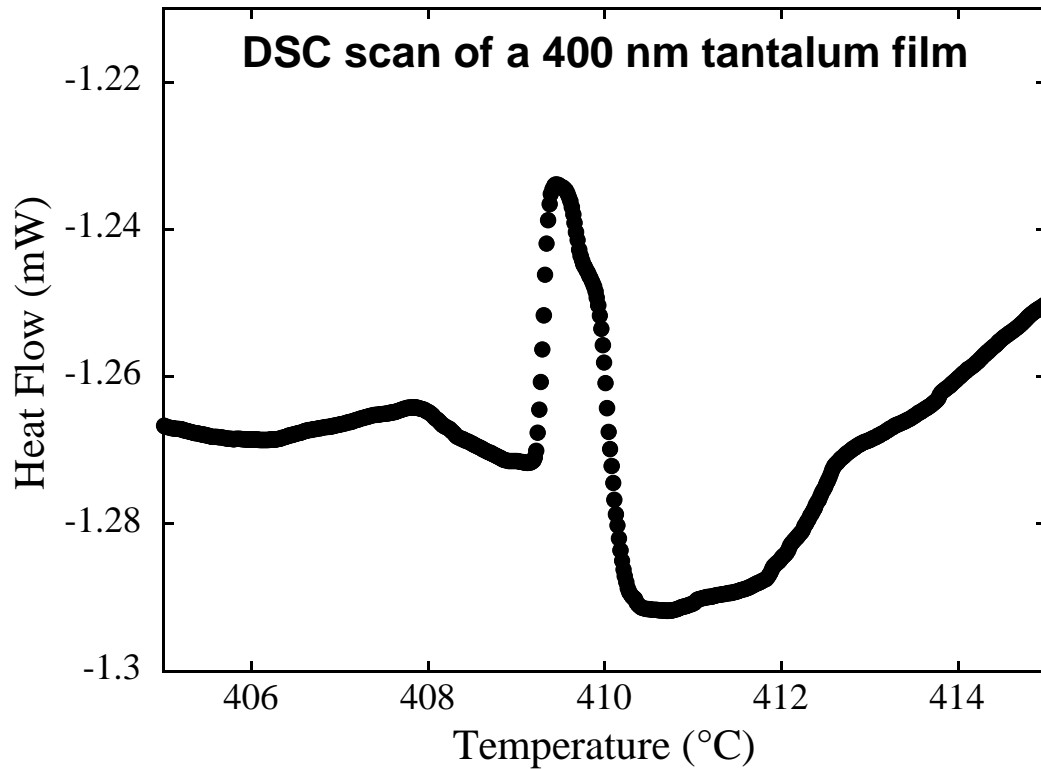


Figure 4.2: DSC scan of a tantalum film deposited in the metastable β phase. The peak indicates an exothermic reaction consistent with β - α phase transformation, and its area gives the energy released during the reaction (driving force of the transformation).

predictions of transformation temperature or rate. The variation in activation energy with oxygen content is shown in Figure 4.3, with the values estimated from the strain energy in Chapter 3 shown for comparison.

These experiments represent the first measurement of the driving force for the β - α phase transformation in tantalum films. However, the results presented here only reflect one sample, as the majority ($\sim 90\%$) do not measurably transform during DSC testing, presumably due to oxygen incorporation during heating in the DSC. There are also several potential sources of error in the experiment. Variations in film thickness from the edge of the substrate to the center (typically $\sim 10\%$ variation) are not accounted for, meaning that the film thickness of any given sample has a corresponding uncertainty, and measurement of in-plane dimensions of the samples was crude ($\pm \sim 0.1$ mm). Estimates of the amount of material transforming were also limited to $\pm \sim 2\%$ due to variations in peak volume with small variations in sample alignment. Additionally, the accuracy in measurement of the energy released during the phase transformation was limited due to the small sample size and any potential energetic effects of oxygen incorporation were ignored. In short, while these results provide an order of magnitude estimate for the driving force, further tests beyond the scope of this thesis must be taken to judge the precision of the experiment and to determine the driving force for the β - α phase transformation with greater accuracy.

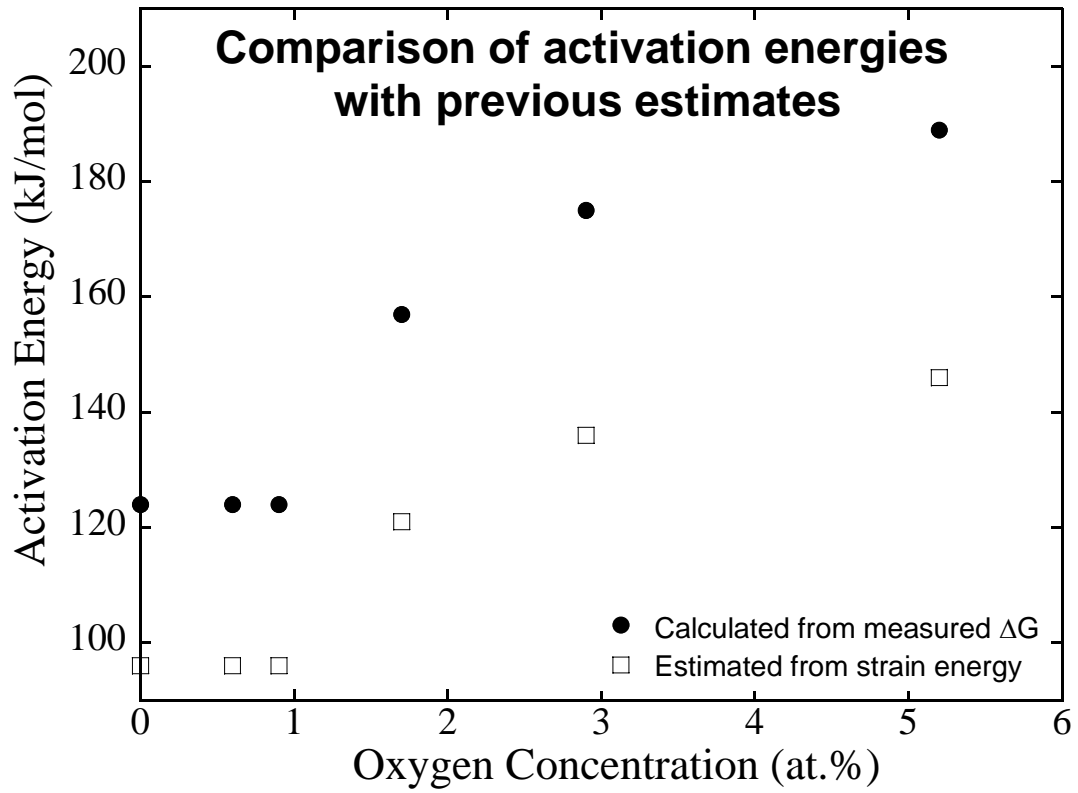


Figure 4.3: Activation energies for the β - α phase transformation as a function of oxygen content in the film. The activation energies that were estimated in Chapter 3 based on the change in strain energy during the transformation are displayed for comparison.

REFERENCES

1. Liu, L., Y. Wang, and H. Gong, *Annealing effects of tantalum films on Si and SiO₂ substrates in various vacuums*. Journal of Applied Physics, 2001. **90**(1), p. 416-420.
2. Liu, L., H. Gong, Y. Wang, J. Wang, A.T.S. Wee, and R. Liu, *Annealing effects of tantalum thin films sputtered on [001] silicon substrate*. Materials Science and Engineering C, 2001. **16**, p. 85-89.
3. Knepper, R., B. Stevens, and S.P. Baker, *Effect of oxygen on the thermomechanical behavior of tantalum thin films during the β - α phase transformation*. Journal of Applied Physics, 2006. **accepted**.
4. Cabral, C., L.A. Clevenger, and R.G. Schad, *Repeated compressive stress increase with 400 C thermal cycling in tantalum thin films due to increases in the oxygen content*. J. Vac. Sci. Technol. B, 1994. **12**(4), p. 2818-2821.

Chapter 5

Coefficient of thermal expansion and biaxial elastic modulus of β phase tantalum thin films

Tantalum thin films can be deposited in either the stable bcc α phase or the metastable tetragonal β phase. The α phase is the only known stable polymorph of tantalum. It has a low resistivity ($\sim 13 \mu\Omega \text{ cm}$), is quite ductile, is commonly used for thin film capacitors [1-3], and is the preferred phase for diffusion barriers between copper and silicon in microelectronic devices [4-6]. The β phase is found only in thin films, has a high resistivity ($\sim 180 \mu\Omega \text{ cm}$), is easier to pattern using reactive ion etching than the α phase [7], and is used for thin film resistors or heaters [1, 2, 8] or in x-ray optics applications [7, 9]. Despite its use in a number of applications, many of the physical properties of the β phase remain unknown. In this work, we determine the coefficient of thermal expansion (CTE) and average biaxial elastic modulus from the thermoelastic behavior of thin tantalum films deposited in the β phase on substrates with different CTEs.

Tantalum films were deposited onto $\sim 0.5 \text{ mm}$ thick substrates of either single crystal (100) silicon or amorphous fused silica. As CTE typically varies with temperature in a nonlinear fashion, nominal values of $3.15 \times 10^{-6} / ^\circ\text{C}$ for (100) silicon and $0.60 \times 10^{-6} / ^\circ\text{C}$ for fused silica were determined by averaging third order polynomial fits over the temperature range of interest (25–200°C) [10]. Substrate thickness was measured using a micrometer, with an accuracy of $\pm 3 \mu\text{m}$.

As exposure to small amounts of oxygen has been seen to greatly affect the thermomechanical behavior of tantalum films [11], great care was taken to minimize ex-

posure during sample preparation and testing. Samples were prepared by magnetron sputter deposition in a UHV chamber evacuated to less than 2×10^{-9} Torr. This UHV deposition system uses a confocal arrangement in which the substrate is mounted on a rotating stage over several 76 mm diameter magnetron sputter guns oriented 23° from the substrate normal and with a mean target-to-substrate distance of 12.5 cm. Before deposition, each substrate was cleaned using a 25 W radio-frequency bias in 8 mTorr of argon (99.9997% pure) for 1 minute to remove adsorbed gas molecules from the substrate surface. Tantalum films were then sputtered to thicknesses ranging from ~ 150 to ~ 400 nm using a DC magnetron source and a 99.95% pure Ta target. A sputtering pressure of 8 mTorr of argon and a sputtering power of 400 W were used. The Ta deposition rate was approximately 15 nm/min. All films were deposited with the substrate grounded. Substrates were rotated at 5 rpm and were unheated during deposition. The maximum temperature reached during deposition was approximately 100°C , as measured by a thermocouple located behind the substrate.

After deposition, films were thermally cycled between room temperature and 600°C in the same UHV system at $5^\circ\text{C}/\text{min}$. Stresses that developed in the films during the thermal cycle were determined by measuring changes in substrate curvature with a laser scanning system and determining the stress using the Stoney equation [12]. Film thicknesses were determined *ex situ* from an average of three profilometer measurements taken in regions near the edge of the substrate that were masked during deposition, with an uncertainty of $\pm \sim 10$ nm. Due to the sputtering geometry, the thickness of films deposited in this system will systematically vary by $\sim 10\%$ from the edge of the substrate to the center. As the substrate curvature measurements were taken over the central 80 mm of the 100 mm diameter substrates, an average film thickness over this region was used in determining film stress.

Stress-temperature data are shown in Figure 5.1a for a tantalum film on a silicon substrate and in Figure 5.1b for a similar film on a fused silica substrate. In both cases, the tantalum film transforms from the metastable β phase to the stable α phase from $\sim 250\text{--}375^\circ\text{C}$ during heating, accompanied by a large change in stress in the tensile direction caused by densification of the film during the transformation [11]. Linear fits to the data at temperatures below $\sim 200^\circ\text{C}$ were used to determine the thermoelastic slopes, $S = \Delta\sigma/\Delta T$, for both the β phase (during heating, before the phase transformation) and the α phase (during cooling, after the transformation). Thermoelastic slopes from two films deposited on each type of substrate are listed in Table 5.1.

The CTE and average biaxial elastic modulus can be calculated from this data following a formulation similar to that of Witvrouw and Spaepen [13]. Assuming linear elastic deformation below 200°C , the thermoelastic slope, caused by differential thermal expansion, can be written as:

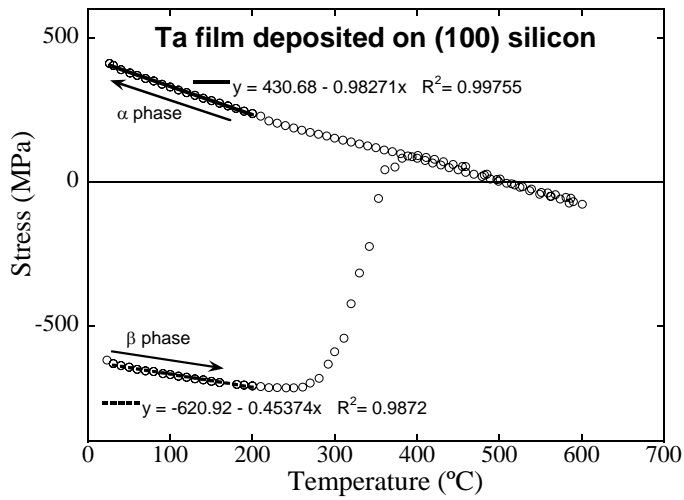
$$S = \frac{\Delta\sigma}{\Delta T} = -Y\Delta\alpha . \quad (5.1)$$

where $\Delta\alpha$ is the difference in CTE between film and substrate ($\Delta\alpha = \alpha_{film} - \alpha_{substrate}$) and $Y = E/(1 - \nu)$ is the biaxial elastic modulus, with E and ν the Young modulus and Poisson ratio, respectively. For a single film on a substrate, it is impossible to determine both Y and α_{film} . However, when the same film is deposited on two substrates with different known CTEs, a system of two equations with two unknowns can be constructed. For the current case, the average biaxial elastic modulus, Y_{Ta} , and CTE, α_{Ta} , are given by:

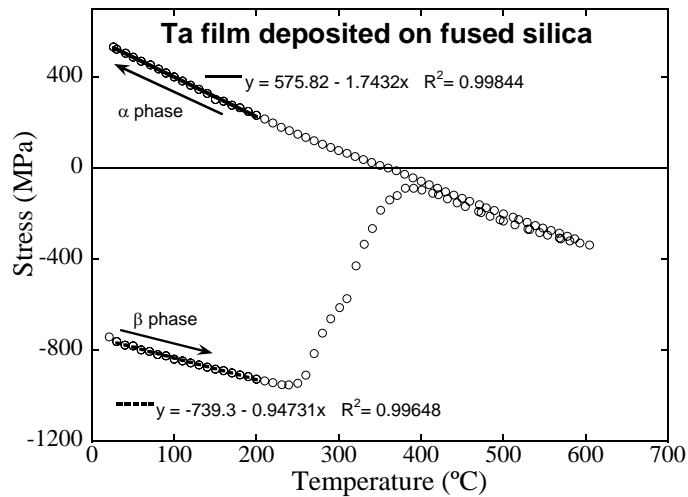
$$Y_{Ta} = \frac{S_{SiO_2} - S_{Si}}{\alpha_{SiO_2} - \alpha_{Si}} \quad (5.2)$$

and

$$\alpha_{Ta} = \frac{S_{SiO_2}\alpha_{Si} - S_{Si}\alpha_{SiO_2}}{S_{SiO_2} - S_{Si}} \quad (5.3)$$



(a)



(b)

Figure 5.1: Stress vs. temperature data for (a) a 390 nm tantalum film deposited in the β phase on an ~ 0.5 mm (100) silicon substrate and (b) a 280 nm tantalum film deposited in the β phase on an ~ 0.5 mm fused silica substrate. The large increase in stress at $\sim 300^\circ\text{C}$ during heating is due to densification of the film during the β - α phase transformation [11]. Linear fits to the data below 200°C are shown by the solid lines and represent thermoelastic slopes for the β phase (heating, before the transformation) and the α phase (cooling, after the transformation).

Table 5.1: Comparison of thermoelastic slopes of β and α phase tantalum films deposited on (100) silicon and fused silica substrates and the calculated CTE and biaxial elastic modulus of each phase. Values of the CTE [14] and the biaxial elastic modulus (for both (100) and (111) crystal orientations) [15] of bulk bcc tantalum are given for comparison.

	β phase	α phase	Bulk α phase
Thermoelastic Slopes on (100) Silicon (MPa / °C)	-0.45 ± 0.02	-0.98 ± 0.03	...
	-0.52 ± 0.03	-1.01 ± 0.04	
Thermoelastic Slopes on Fused Silica (MPa / °C)	-0.95 ± 0.04	-1.74 ± 0.06	...
	-0.89 ± 0.07	-1.60 ± 0.11	
Average CTE ($\times 10^{-6}$ / °C)	6.0 ± 0.8	6.9 ± 0.9	6.5
Average Biaxial Elastic Modulus (GPa)	170 ± 20	265 ± 30	230 [(100) orientation]
			310 [(111) orientation]

where α_{Si} is the CTE of the silicon substrates, α_{SiO_2} the CTE of the fused silica substrates, S_{Si} the thermoelastic slope of a tantalum film on a silicon substrate, and S_{SiO_2} the thermoelastic slope of a tantalum film on a fused silica substrate. Films deposited on silicon and fused silica substrates should be nominally the same, as the interface conditions between the film and substrate are very similar in the two systems due to the native oxide on the silicon substrates.

The calculated CTEs and biaxial elastic moduli for both the α and β phases are shown in Table 5.1, along with values reported for bulk bcc tantalum for comparison. Good agreement was found between values for the CTE and biaxial modulus calculated for α phase films and values reported for bulk bcc tantalum [14]. The CTE calculated for α phase films was within 5% of the reported bulk value and well within the experimental uncertainty. The calculated value for the average biaxial elastic modulus of the α phase films was approximately halfway between reported values for (100) and (111) orientations. (These orientations correspond to the minimum and maximum average biaxial elastic moduli in cubic materials.) As phase-transformed films typically show a broad distribution of out-of-plane crystal orientations [16], such behavior is consistent with expectations.

While the properties of the phase-transformed films were essentially those of bulk tantalum, the as-deposited β films have CTEs that are about 15% lower and elastic moduli that are quite different, with Y_α exceeding Y_β by more than 50%. The calculated modulus of the β phase was also substantially less than the minimum possible for any crystal orientation of bcc tantalum, indicating that the two phases have very different elastic behaviors. Thus, it appears that the majority of the difference in the observed thermoelastic behavior of the two phases can be attributed to differences in the elastic constants, with differences in CTE playing a secondary role.

Some degree of error is expected in the calculations due to uncertainties in the film thickness and the fairly wide range of CTEs reported in the literature for silicon and fused silica. As different reported functions for $\alpha(T)$ of the substrate materials can lead to variations in average CTE of up to 10% over the temperature range of interest [10, 14, 17], the experimental uncertainty increases as well. The calculated modulus of the film varies linearly with the difference in substrate CTE, $\alpha_{SiO_2} - \alpha_{Si}$, and while the functional form for the calculation of film CTE is more complex, the calculated CTEs will vary similarly. In addition, there is some uncertainty in the measured thermoelastic slopes due to uncertainties in film thickness. If there are systematic errors in the average thickness of the film, t_f , and thus the stress values and thermoelastic slopes, this would be reflected only in the calculation of the biaxial elastic modulus calculation, where $Y \propto 1/t_f$; the CTE calculation is insensitive to systematic errors in film thickness. Such errors can potentially cause a variation in the absolute values of Y but the relative difference between the two phases will remain constant.

Values of the CTE and average biaxial elastic modulus have been determined for tantalum films deposited in the metastable β phase both before and after transformation to the stable α phase. While the CTEs vary only slightly between the two phases and are in good agreement with bulk values, there are significant differences in the elastic moduli that account for the very different thermoelastic slopes of the films before and after the phase transformation. While the modulus for the α phase films is in good agreement with bulk isotropic values, it is found that the tantalum films as-deposited in the β phase are significantly more compliant.

The authors would like to thank Max Aubain for his assistance with the profilometer measurements.

REFERENCES

1. Baker, P.N., *Preparation and properties of tantalum thin films*. Thin Solid Films, 1972. **14**, p. 3-25.
2. Schwartz, N., W.A. Reed, P. Polash, and M.H. Read, *Temperature coefficient of resistance of beta-tantalum films and mixtures with b.c.c.-tantalum*. Thin Solid Films, 1972. **14**, p. 333-347.
3. Westwood, W.D., N. Waterhouse, and P.S. Wilcox, *Tantalum Thin Films*. (Academic Press, London, 1975).
4. Holloway, K. and P.M. Fryer, *Tantalum as a diffusion barrier between copper and silicon*. Applied Physics Letters, 1990. **57**(17), p. 1736-1738.
5. Clevenger, L.A., N.A. Bojarczuk, K. Holloway, J.M.E. Harper, C. Cabral, R.G. Schad, F. Cardone, and L. Stolt, *Comparison of high vacuum and ultra-high vacuum tantalum diffusion barrier performance against copper penetration*. J. Appl. Phys., 1993. **73**(1), p. 300-308.
6. Laurila, T., K. Zeng, and J.K. Kivilahti, *Effect of oxygen on the reactions in the Si/Ta/Cu metallization system*. J. Mater. Res., 2001. **16**(10), p. 2939-2946.
7. Kondo, K., M. Nakabayashi, K. Kawakami, T. Chijimatsu, M. Nakaishi, M. Yamada, M. Yamabe, and K. Sugishima, *Stress stabilization of β -tantalum and its crystal structure*. J. Vac. Sci. Technol. A, 1993. **11**, p. 3067-3071.
8. Westwood, W.D. and F.C. Livermore, *Phase composition and conductivity of sputtered tantalum*. Thin Solid Films, 1970. **5**, p. 407-420.
9. Yoshihara, T. and K. Suzuki, *Sputtering of fibrous-structured low-stress Ta films for x-ray masks*. J. Vac. Sci. Technol. B, 1994. **12**(6), p. 4001-4004.
10. Touloukian, Y.S., R.K. Kirby, R.E. Taylor, and T.Y.R. Lee, eds. *Thermal Expansion: Nonmetallic Solids*. Thermophysical Properties of Matter, ed. Y.S. Touloukian. Vol. 13. 1977, IFI/Plenum Data Company: New York.
11. Knepper, R., B. Stevens, and S.P. Baker, *Effect of oxygen on the thermomechanical behavior of tantalum thin films during the β - α phase transformation*. Journal of Applied Physics, 2006. **accepted**.
12. Stoney, G., *The tension of metallic films deposited by electrolysis*. Proceedings of the Royal Society of London, 1909. **A82**, p. 172-175.
13. Witvrouw, A. and F. Spaepen, *Viscosity and elastic constants of amorphous Si and Ge*. Journal of Applied Physics, 1993. **74**(12), p. 7154-7161.
14. Touloukian, Y.S., R.K. Kirby, R.E. Taylor, and P.D. Desai, eds. *Thermal Expansion: Metallic Elements and Alloys*. Thermophysical Properties of Matter, ed. Y.S. Touloukian. Vol. 12. 1975, IFI/Plenum Data Company: New York.

15. Featherston, F.H. and J.R. Neighbours, *Elastic constants of tantalum, tungsten, and molybdenum*. *Physical Review*, 1963. **130**(4), p. 1324-1333.
16. Knepper, R., R. Fertig, K. Jackson, and S.P. Baker, *Microstructure of phase-transformed tantalum thin films*. (in preparation).
17. Freund, L.B. and S. Suresh, *Thin Film Materials: Stress, Defect Formation, and Surface Evolution*. (Cambridge University Press, Cambridge, 2003).

Chapter 6

Microstructure of phase-transformed tantalum thin films

Robert Knepper, Ray Fertig, Katherine Jackson, and Shefford P. Baker

*Cornell University, Department of Materials Science and Engineering, Bard Hall,
Ithaca, NY 14853-1501*

6.1 Abstract

The microstructures of tantalum films deposited in the bcc α phase and films deposited in the metastable tetragonal β phase and transformed to the α phase by thermal cycling were analyzed using electron backscatter diffraction. While films deposited in the α phase demonstrate a typical thin film microstructure, phase-transformed films have an unusual microstructure characterized by a discontinuous grain boundary structure and consistent gradients in crystal orientation within individual grains of up to $4^\circ/\mu\text{m}$ over a distance of several micrometers. Analysis of the distribution of pixel-to-pixel axes of rotation using rotation pole figures strongly suggests that these gradients are due to aligned arrays of edge dislocations on primary slip systems parallel or nearly parallel to the plane of the film. A dislocation density of $2.4 \times 10^{14}/\text{m}^2$ is geometrically necessary to account for the measured orientation gradients. It is suggested that these arrays of aligned dislocations are the result of large shear stresses in the film due to the densification of the crystal structure causing large changes in stress across the moving phase boundary during the transformation.

6.2 Introduction

Tantalum thin films have been studied due to their applications in microelectronic devices and in x-ray optics. Depending on the deposition conditions and substrate [1-5], tantalum films can be deposited with two different crystal structures: either the stable bcc α phase, or the metastable tetragonal β phase. It has been shown previously [6-9] that tantalum films deposited in the β phase will transform to the α phase with sufficient heating by a nucleation and growth process [9]. When pure β phase tantalum films are annealed in ultra-high vacuum (UHV) conditions, they begin to transform to the α phase at $\sim 300^\circ\text{C}$ [9]. As shown in Figure 6.1, this transformation is accompanied by a large change in stress in the tensile direction that is caused by densification of the film due primarily to the change in crystal structure [9]. Typically, the microstructure of annealed metal films is characterized by well-defined columnar grains with fiber texture having an average grain size on the same order as the film thickness [10]. The microstructure of films that have undergone transformation from the β to the α phase is quite different and one that has not previously been seen in any kind of thin metal film. This paper details these differences and suggests a mechanism by which such a microstructure might arise.

6.3 Experiment

6.3.1 Sample preparation

Samples were prepared by magnetron sputter deposition in a UHV chamber evacuated to less than 2×10^{-9} Torr. This UHV deposition system uses a confocal arrangement in which the substrate is mounted on a rotating stage over several 76 mm diameter magnetron sputter guns oriented 23° from the substrate normal and with a mean target-to-substrate distance of 12.5 cm. 100 mm diameter oxidized (100) Si substrates were used. Before deposition, each substrate was cleaned using a 25 W radio-frequency bias

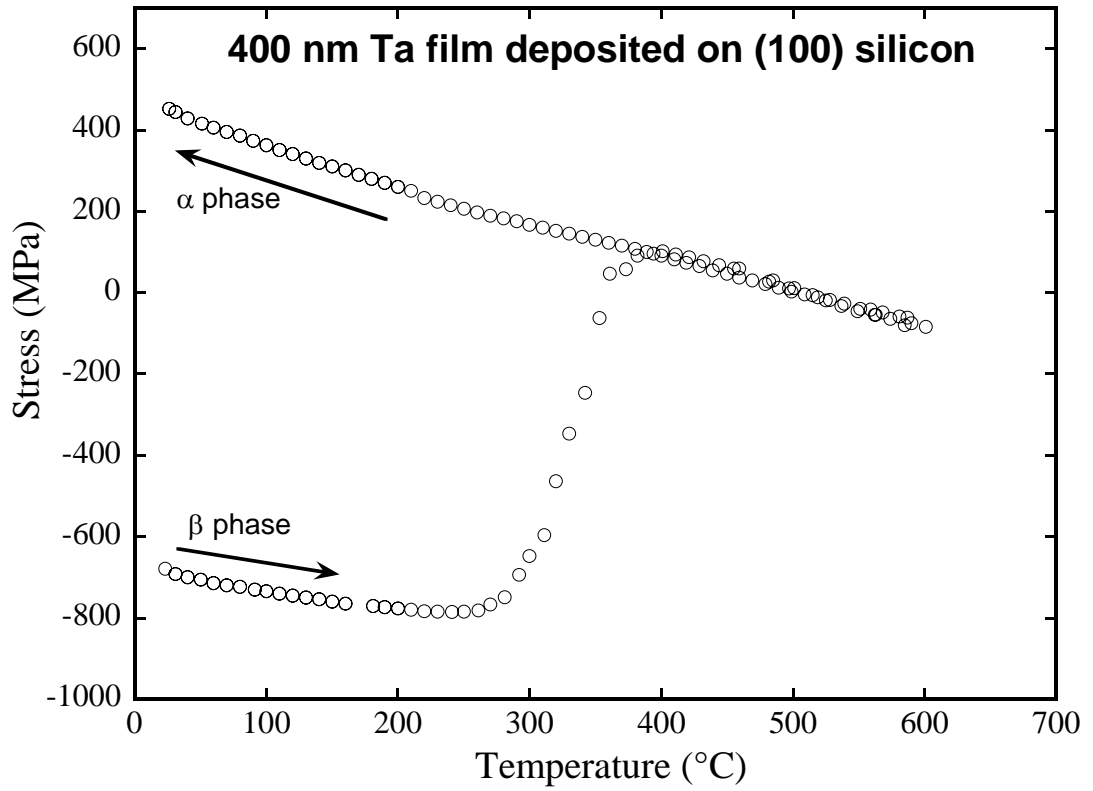


Figure 6.1: Stress-temperature plot of a 400 nm tantalum film deposited in the metastable β phase thermally cycled between room temperature and 700°C. The film transforms to the stable α phase between 300° and 375°C, accompanied by a large change in stress in the tensile direction.

in 8 mTorr of argon for 1 min. to remove adsorbed gas molecules from the substrate surface. Tantalum films were then sputtered to a thickness of 300–400 nm using a DC magnetron source and a 99.95% pure Ta target. A sputtering pressure of 8 mTorr of argon and a sputtering power of ~ 400 W were used. The Ta deposition rate was approximately 15 nm/min. All films were deposited with the substrate grounded. Substrates were rotated at 5 rpm and were unheated during deposition. The maximum temperature reached during deposition for films deposited in the β phase was approximately 100°C, as measured by a thermocouple located behind the substrate. Several films were deposited in the α phase by increasing the substrate temperature to 500°C during deposition. After deposition, samples were transferred to a vacuum furnace within the same UHV system. Samples were then thermally cycled between room temperature and 700–750°C at $\sim 5^\circ\text{C}/\text{min}$. During thermal cycling, films deposited in the β phase transform to the α phase, as determined by *ex situ* x-ray analysis [9].

6.3.2 Microstructure Characterization

Electron backscatter diffraction (EBSD) was used to determine local crystallographic orientation information in both deposited and phase-transformed α tantalum films. The EBSD system used in this work (HKL Technology, Inc.) operates in conjunction with a Leica 440 SEM operating with a beam voltage and current of 25 kV and 1.2 nA, respectively. A small area (~ 50 nm diameter) of the sample is subjected to an electron beam at an angle 70° from the sample normal. The electrons are scattered as they enter the sample, and these scattered electrons undergo Bragg diffraction from the various crystal planes in that region. The diffracted electrons produce bands of high and low intensity (called Kikuchi patterns) that are detected by a CCD area detector. These images are subsequently noise reduced by averaging over ten frames. The crystal orientation of the sample at this location is determined by computerized analysis of

the Kikuchi pattern using the four or five most prominent bands using CHANNEL 5 software (HKL, Inc.). By scanning an array of points with 100 nm spacing over a $12\ \mu\text{m} \times 12\ \mu\text{m}$ grid, detailed maps of local crystallographic orientation are generated. Similar arrays, scanned at a lower resolution and over a larger area (1–2 μm spacing over $\sim 100\ \mu\text{m}$), are used to provide a more general view of the crystal orientation distribution within each sample. Further, a series of line scans with a 100 nm point spacing along the line and several μm between lines were used to determine grain size. Boundaries were defined as abrupt changes in orientation of more than 2° where the orientation on either side of the boundary remained relatively constant for at least two pixels. Single pixel grains were not considered, as it was impossible to determine from the line scans whether or not such points were correctly indexed. As such, only grains larger than $\sim 200\ \text{nm}$ were considered in the current analysis. Based on reports of similar EBSD systems [11, 12], we estimate angular accuracy at $\sim 1^\circ$ and the precision at $\sim 0.1^\circ$.

6.4 EBSD Orientation Maps

6.4.1 Analysis

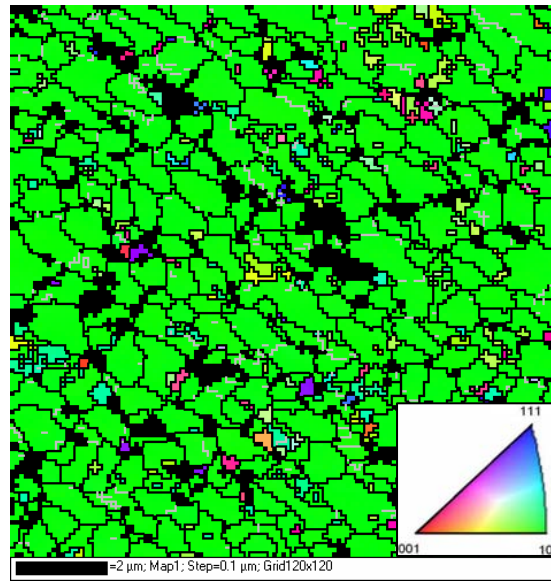
EBSD orientation maps were generated to show local distributions of out-of-plane crystal orientations in both as-deposited α and phase-transformed α films. The image shows out-of-plane crystallographic information by color, as detailed by the stereographic triangle in the lower right-hand corner of each map. The black lines in the image depict high-angle grain boundaries (defined as a misorientation between neighboring pixels of greater than 8°), while gray lines indicate low-angle grain boundaries (defined as a misorientation between neighboring pixels of between 2° and 8°). Black pixels indicate regions where the EBSD software was not able to match the measured Kikuchi pattern with a corresponding α -Ta crystal orientation. In generating orienta-

tion maps for the tantalum films studied in this work, typically about 80–85% of the points were correctly indexed by the CHANNEL 5 software, with ~ 1–2% wild spikes (isolated incorrectly indexed points) and the remainder non-indexed. Following noise reduction, greater than 90% of the points on an orientation map were indexed. Noise reduction was performed only on orientation maps to provide a better representation of the local microstructure of these films.

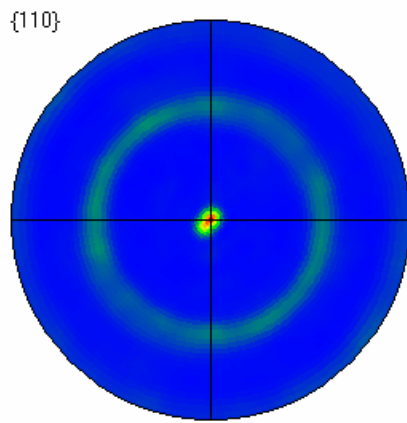
6.4.2 Results

Figure 6.2a shows an EBSD orientation map of a tantalum film that was deposited in the α phase. It can be seen from these data that the film is very strongly and sharply textured, with a preferred (110) out-of-plane orientation. The strong (110) texture is clearly evident on the local scale shown in Figure 6.2a and from the (110) pole figure and inverse pole figure shown in Figures 6.2b and c, respectively. The grain size is on the order of the film thickness (~ 400 nm), indicating that the grains are likely to be columnar in nature. The grain boundaries are all well defined and continuous. In short, the film deposited in the α phase has a microstructure typical of thin metal films.

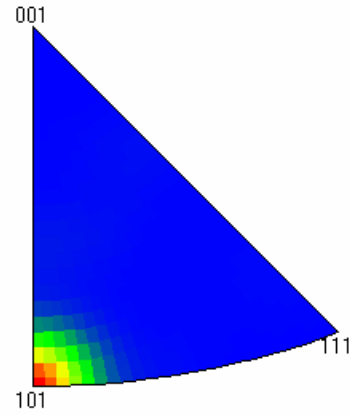
Films that were deposited in the β phase, but later transformed to α during thermal cycling have a much different microstructure. The most striking features of the phase-transformed tantalum films can be seen in the EBSD map of the local microstructure shown in Figure 6.3. The phase-transformed microstructure is characterized by large gradients in crystal orientation that are often present within a single “grain”. Few high-angle grain boundaries are seen in these films, and the ones that are present are often not continuous, making it difficult to define a grain in the traditional sense. It is occasionally possible to go from one side of a high-angle grain boundary to the other without crossing any high- or low-angle boundaries. Grains also tend to be elongated, often with a preferred direction of elongation and are much larger than the film thickness (~



(a)



(b)



(c)

Figure 6.2: (a) EBSD map showing the local out-of-plane crystal orientations of a tantalum film deposited in the α phase. The film has a strong (110) out-of-plane orientation, as can be seen from (b) the (110) pole figure and (c) the out-of-plane inverse pole figure, and a grain size on the order of the film thickness. Note the well-defined grains enclosed by high angle grain boundaries.

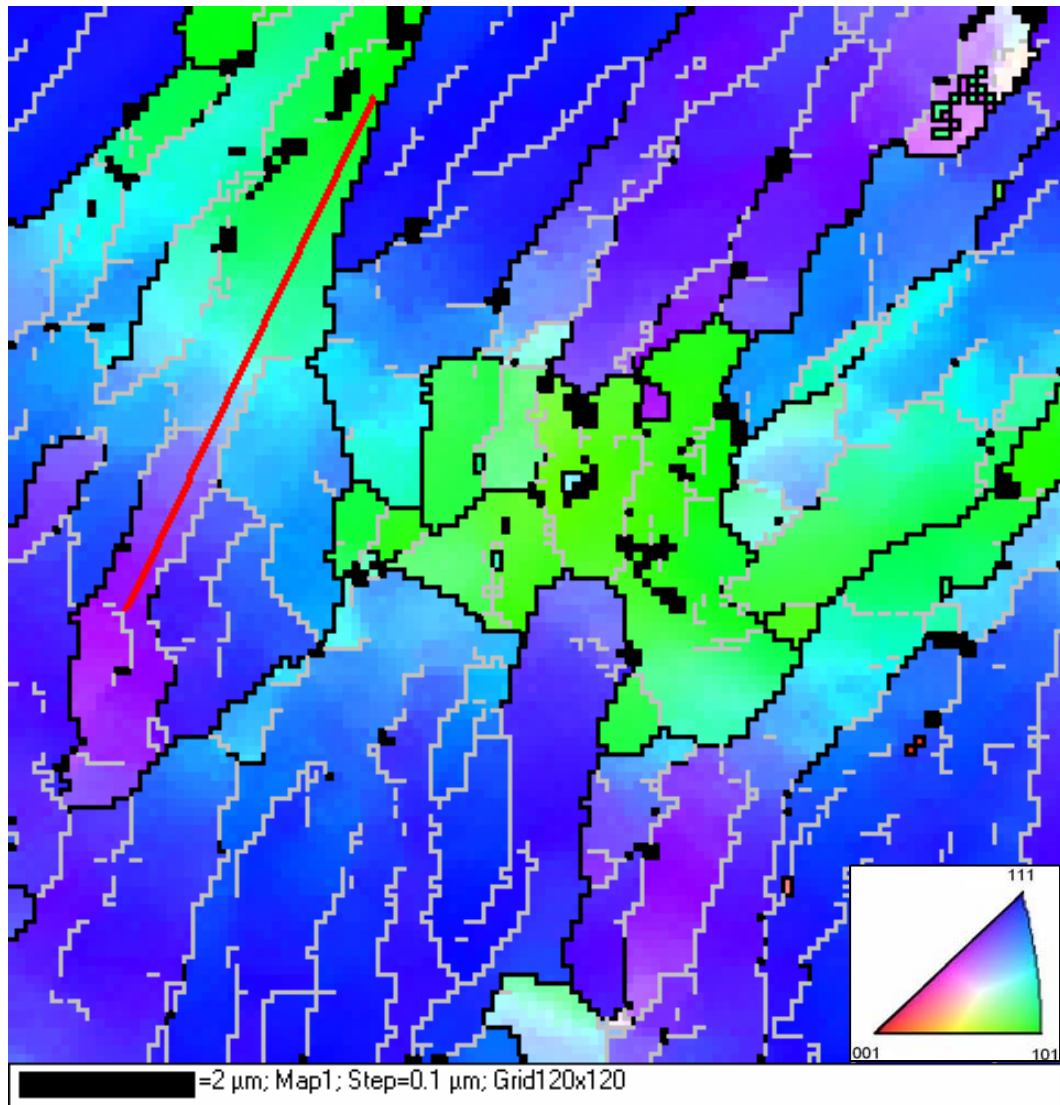


Figure 6.3: EBSD map showing the local out-of-plane crystal orientations of a tantalum film deposited in the β phase and transformed to the α phase during thermal cycling. The crystal orientation gradually changes with position in much of the film. Few high angle ($> 8^\circ$, shown by black lines) or low angle grain boundaries (between 2° and 8° , shown by gray lines) are present, and many are discontinuous. The red line lies in the middle of a region that visibly demonstrates a large, gradual change in crystal orientation seen commonly in these films.

1.8 μm). The microstructure shown in Figure 6.3 is representative of the seven different oxygen-free phase-transformed tantalum films ranging in thickness from $\sim 150\text{--}500$ nm that we have analyzed. While the EBSD maps show local out-of-plane orientations ranging from (110) to (111) to (211), as seen in the PFs and IPF in Figure 6.4, these films have a preferred crystal orientation in the vicinity of (111) out-of-plane, but the peak is diffuse and a broad distribution of orientations are seen.

6.4.3 Discussion

The gradients in crystal orientation appear in most grains and are often quite substantial. Gradients larger than $3^\circ/\mu\text{m}$ are not uncommon and often extend over a range of several micrometers. For example, in the region of Figure 6.3 highlighted by the red line, the out-of-plane orientation changes from close to (110) to approximately (211) without crossing any high-angle or even low-angle grain boundaries. To further illustrate this point, a plot depicting crystal misorientation (relative to the line's endpoint) with position along this line is shown in Figure 6.5. The plot shows that the crystal orientation is changing in a nearly linear fashion through this region with a magnitude of $\sim 4^\circ/\mu\text{m}$.

As gradients in orientation of this magnitude are highly unusual for a crystalline material and can even challenge common perceptions of what defines a crystal, one must consider how it is possible for such variation in orientation to exist. The most probable solution employs the concept of geometrically necessary dislocations (GNDs), where in order for a gradient in crystal orientation to exist in the absence of grain boundaries, there must also exist an array of dislocations with a preferred alignment and Burger's vector (see Nye [13], Arsenlis and Parks [14], and El-Dasher *et al* [15] for additional details). For example, an array of aligned edge dislocations having both their Burger's vectors and sense vectors (the line along which the dislocation lies)

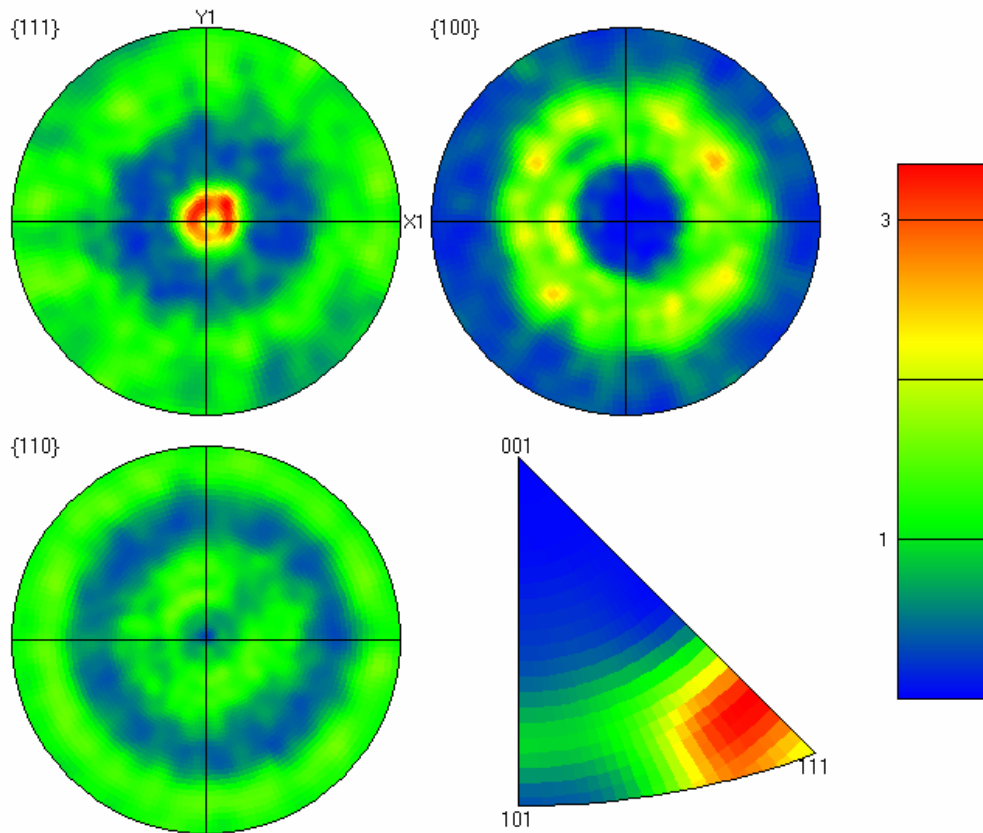


Figure 6.4: (001), (110), and (111) out-of-plane pole figures of a phase-transformed tantalum film and an out-of-plane inverse pole figure of the same film. Note the diffuse nature of the PFs and the peak in the IPF, indicating a film that is textured, but not sharply.

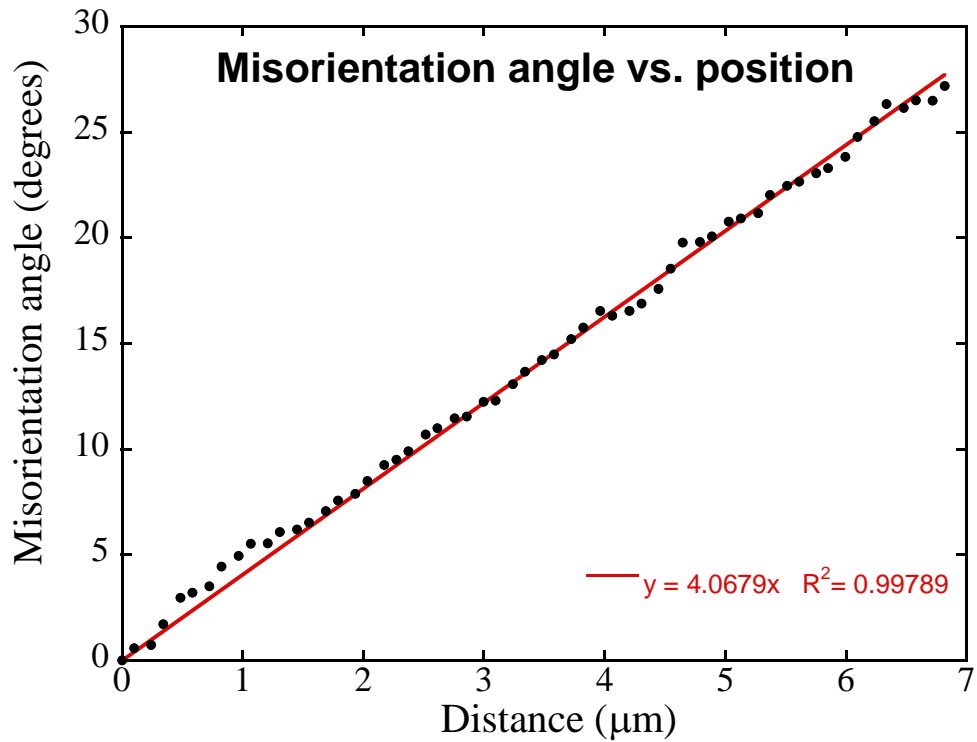


Figure 6.5: Plot depicting the change in misorientation angle with position along the red line shown in Figure 6.3 (relative to the bottom endpoint). Note that the linear trend indicates a constant rotation of $\sim 4^\circ/\mu\text{m}$ over a distance of more than seven micrometers.

in the plane of the film would cause a rotation of the crystal about an axis laying parallel to the sense vector. Using a simple 2-D model based on the work of Nye [13], the GND density, ρ , can be calculated, assuming such an array of aligned edge dislocations, from the rate of angular misorientation with position, θ/x , and the magnitude of the Burger's vector, b , from

$$\rho = \frac{\theta}{bx}. \quad (6.1)$$

From the measured θ/x of $4^\circ/\mu\text{m}$ and the value of b for bcc tantalum of 2.863 \AA , a value of $\sim 2.4 \times 10^{14}/\text{m}^2$ is found for ρ . If the GNDs were spread uniformly throughout the film, this density would result in an in-plane spacing between dislocations of $\sim 12 \text{ nm}$. However, as the in-plane resolution of the EBSD scan was 100 nm , it is impossible to tell from these data whether the dislocations are spread evenly or grouped into subgrain boundaries at a length scale smaller than the resolution of the scan. The calculated value for ρ is moderate for a metal, and it is not unreasonable that such a density would arise from processes associated with the phase transformation. It is important to note that this is only the minimum density of dislocations needed to obtain the observed orientation gradients. It is often the case that the total dislocation density is much greater than the GND density [16]; as such, GNDs are often best studied by EBSD, where their effect on orientation on the micron-scale can be easily seen and quantified, rather than using TEM, where GNDs can be lost amid the much higher density of randomly oriented dislocations [15].

While variations in local crystal orientation have been seen in EBSD studies of heavily deformed bulk aluminum [15, 17], copper [18], and steel [19] and within single grains in copper thin films studied by x-ray microdiffraction [20], the magnitude of the orientation gradients in these materials are generally at least an order of magnitude less than those seen in phase-transformed tantalum films. Variations in GND density

with position have been analyzed in bulk aluminum and copper, based on local curvatures of the crystal obtained from EBSD data [17, 18]. While GND densities of greater than $10^{16}/\text{m}^2$ have been reported in these studies, such values can be misleading, as they include rotations due to grain boundaries of up to 14° . If low angle boundaries greater than 2° were to be excluded from GND determination as in the current study, the typical GND densities in deformed bulk metals are likely to be several orders of magnitude lower and less than the GND density for phase-transformed tantalum films. Additionally, while other materials in which variations in local crystal orientation have been studied show only small, highly localized perturbations (typically less than $\sim 1^\circ$) about the mean orientation of a grain or subgrain, the phase-transformed tantalum films we have studied often have continuous orientation gradients over long distances that can cover the entirety of a grain and produce misorientations of greater than 20° .

6.5 Rotation Pole Figures

6.5.1 Analysis

At this point in the analysis, the character and location of the dislocations that cause the gradients in crystal orientation have yet to be considered. In order to gain further insight into this matter, we have taken a more detailed look at the axes around which these rotations occur by constructing “rotation pole figures” (RPFs). RPFs plot the distribution of all axes of rotation between neighboring pixels in an EBSD orientation map (excluding those across grain boundaries) on a stereographic plot. To do this, a list of Euler angles describing the orientation of each pixel along with its location is exported from the CHANNEL 5 software. The axis and magnitude of rotation between all neighboring pixels is then determined using a MATLAB code, after which the distribution of rotation axes can be plotted for any range of misorientation angles. As the crystal can be rotated around many different axes to produce crystallographically iden-

tical results, only those axes that use the minimum magnitude of rotation are plotted. These rotation axes can be plotted relative to either the crystal unit cell coordinate axes (crystal RPF) or relative to a fixed real-space coordinate system (sample RPF). Crystal RPFs can be used to show whether rotations occur around particular crystallographic axes, as would be the case if a particular type and character of dislocation were responsible for the rotations. Similarly, sample RPFs can be used to show if rotations occur about particular directions in the sample. The intensities shown in the RPFs are all normalized by their mean intensity. Note that crystal and sample RPFs have different shapes due to the different application of symmetry conditions in crystal and sample coordinates.

6.5.2 Results

A series of crystal RPFs calculated from the EBSD map in Figure 6.3 are shown in Figure 6.6. Crystal RPFs are depicted as stereographic triangles similar to that seen in an inverse pole figure, except that each location in a crystal RPF corresponds to an axis in a cubic crystal about which a rotation may occur. Crystal RPFs are shown for several different ranges of misorientations smaller than that required to compose a low-angle grain boundary, 0–0.2° (“small”), 0.2–0.45° (“medium”), and 0.45–2° (“large”). A substantial peak is evident around the $\langle 211 \rangle$ -type directions for “medium” misorientations (denoted by the star in Figure 6.6). While the distributions appear mostly random for “small” and “large” misorientations, a smaller peak around the same location can be seen for “small” misorientations as well.

A series of sample RPFs also calculated from the EBSD map in Figure 6.3 are shown in Figure 6.7. Sample RPF are similar to standard out-of-plane pole figures in that the center of the sample RPF corresponds to rotation axes normal to the plane of the film, while the edge of the sample RPF corresponds to rotation axes in the plane of

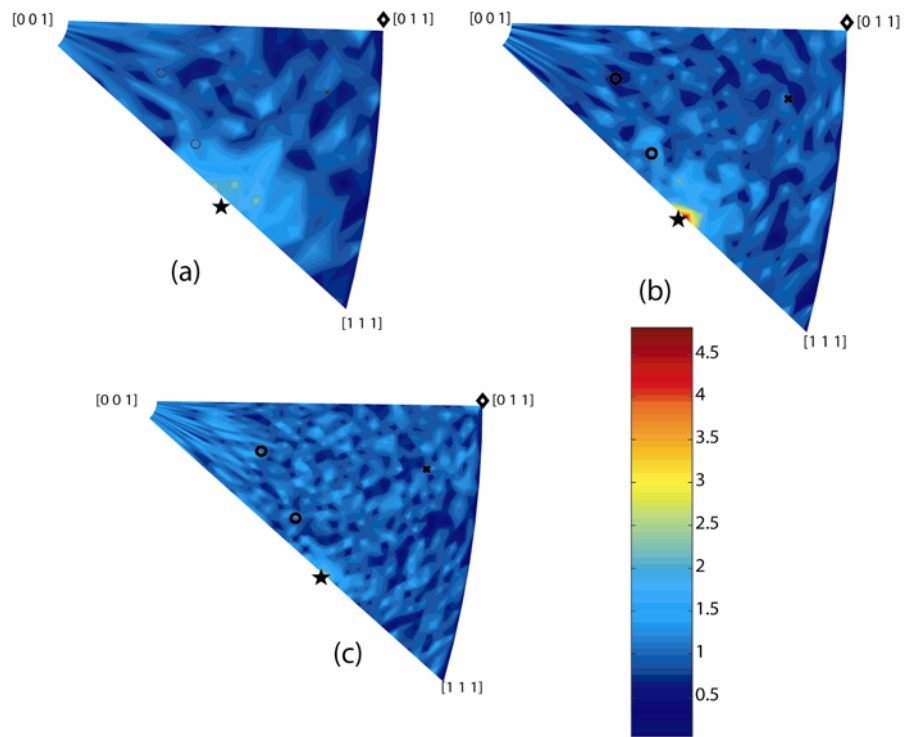


Figure 6.6: Rotation pole figures in crystal coordinates showing the distribution of pixel-to-pixel rotations about crystal axes in a phase-transformed Ta film for (a) $0-0.2^\circ$, (b) $0.2-0.45^\circ$, and (c) $0.45-2^\circ$ misorientations. The peak around the $[211]$ direction (denoted by the star) is consistent with the rotation generated by an array of aligned edge dislocations on a primary slip system.

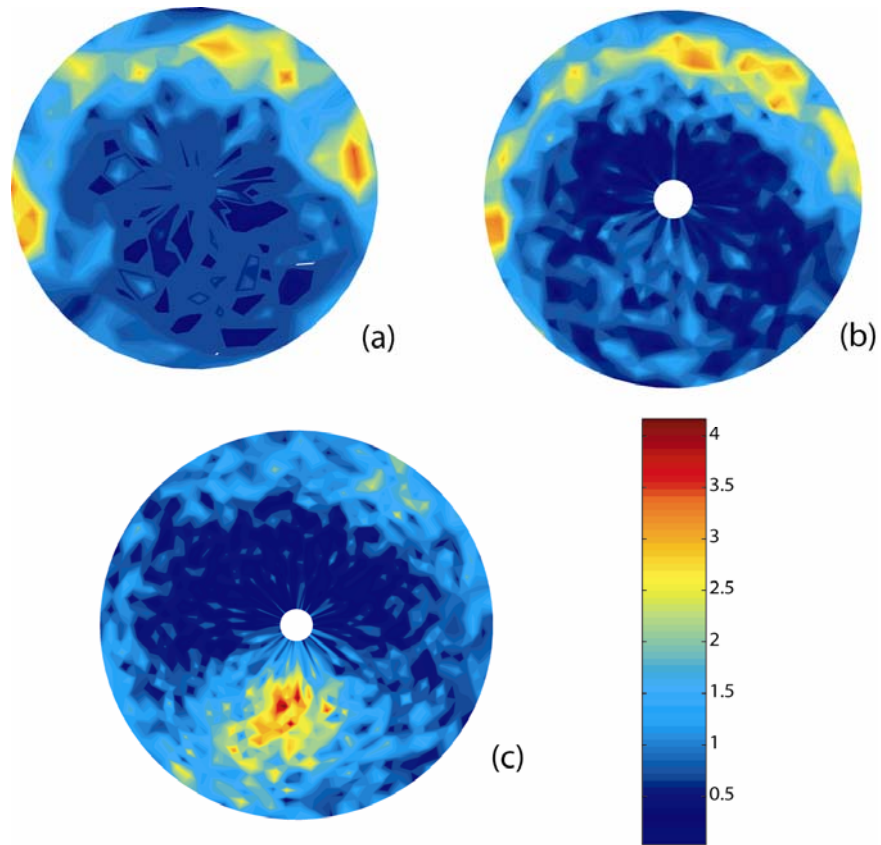


Figure 6.7: Rotation pole figures in sample coordinates showing the distribution of pixel-to-pixel axes of rotation relative to the sample coordinate system for (a) $0\text{--}0.2^\circ$, (b) $0.2\text{--}0.45^\circ$, and (c) $0.45\text{--}2^\circ$ misorientations. The intensity near the edge of the sample RPF indicates that the rotation axes are primarily in or near the plane of the film.

the film. As with the crystal RPFs, sample RPFs are shown for different ranges of misorientations, 0–0.2° (“small”), 0.2–0.45° (“medium”), and 0.45–2° (“large”). Nearly all of the intensity is located at or near the edge of the sample RPFs for “small” and “medium” misorientations, indicating that the rotation axes are located in or near to the plane of the film. “Large” misorientations, however, show a large, diffuse peak approximately 45° from the sample normal in addition to lesser intensities near the plane of the film.

6.5.3 Discussion

Much can be inferred about the dislocation structure of phase-transformed tantalum films from RPF data. $\langle 211 \rangle$ -type crystal rotation axes are dominant over the range of misorientations that are commonly seen as consistent, smooth orientation gradients in the EBSD maps. The $\langle 211 \rangle$ axes also coincide with the sense vectors of edge dislocations on primary bcc slip systems ($\langle 111 \rangle$ slip directions on $\{110\}$ slip planes). As an array of aligned edge dislocations will cause a rotation about an axis parallel to their sense vectors, this provides strong evidence that the crystal orientation gradients are caused by such arrays of dislocations. It is important to note that no substantial peaks are evident in the crystal RPF on any of the rotation axes consistent with arrays of screw dislocations on primary slip planes (shown by the diamond) or edge dislocations located on secondary slip systems (i.e. $\langle 111 \rangle$ slip directions on $\{112\}$ slip planes, shown as the \times , or $\langle 111 \rangle$ slip directions on $\{123\}$ slip planes, shown by the circles), and thus the crystal RPF points only to arrays of edge dislocations on primary slip systems. Combined with the information from the sample RPFs, the data strongly support the presence of edge dislocations on primary slip systems lying in or near the plane of the film as leading to the observed crystal orientation gradients.

It is clear from the crystal RPFs that the GNDs have a fairly constant density and do not appear for misorientations greater than $\sim 4.5^\circ/\mu\text{m}$ ($0.45^\circ/\text{pixel}$). While the crystal RPFs show no preferred rotation axis or type of dislocation at “large” misorientations, it is not clear why the dominant rotation axis in the sample RPF changes from the plane of the film to $\sim 45^\circ$ off-normal, though it is likely to have to do with the relaxation of stress in the film during the phase transformation.

It is important to note that there is a spread in the distributions of rotation axes in both the crystal and sample RPFs. There are several possible reasons for this. One is that there may be randomly oriented dislocations mixed in with the GNDs that causes local axes of rotation to vary about a mean. However, this is unlikely to be the primary cause of the spread, as the 100 nm spacing between pixels includes more than 5 GNDs on average, reducing the impact of randomly oriented dislocations. A more likely cause is the angular precision of the EBSD. As shown by Prior [21], for small misorientations, the angular resolution of the EBSD may limit the accuracy in which a particular axis of rotation can be determined. Bate *et al* [22] have shown that the angular uncertainty in determining the axis of rotation between pixels, β , can be determined by:

$$\langle \beta \rangle = \tan^{-1} \left(\frac{\delta}{\omega} \right) \quad (6.2)$$

where δ is the angular precision of the EBSD and ω the misorientation between pixels. As the precision of the EBSD ($\sim 0.1^\circ$) is of the same order as the pixel-to-pixel misorientation ($\sim 0.3^\circ$), the potential for error in the measurement of any particular axis of rotation is high ($\sim 20^\circ$), though it is evident from the crystal RPF of “medium” misorientations that it is still possible to obtain fairly sharp peaks. This uncertainty in determining the axis of rotation is likely to cause some of the observed spread in the RPFs.

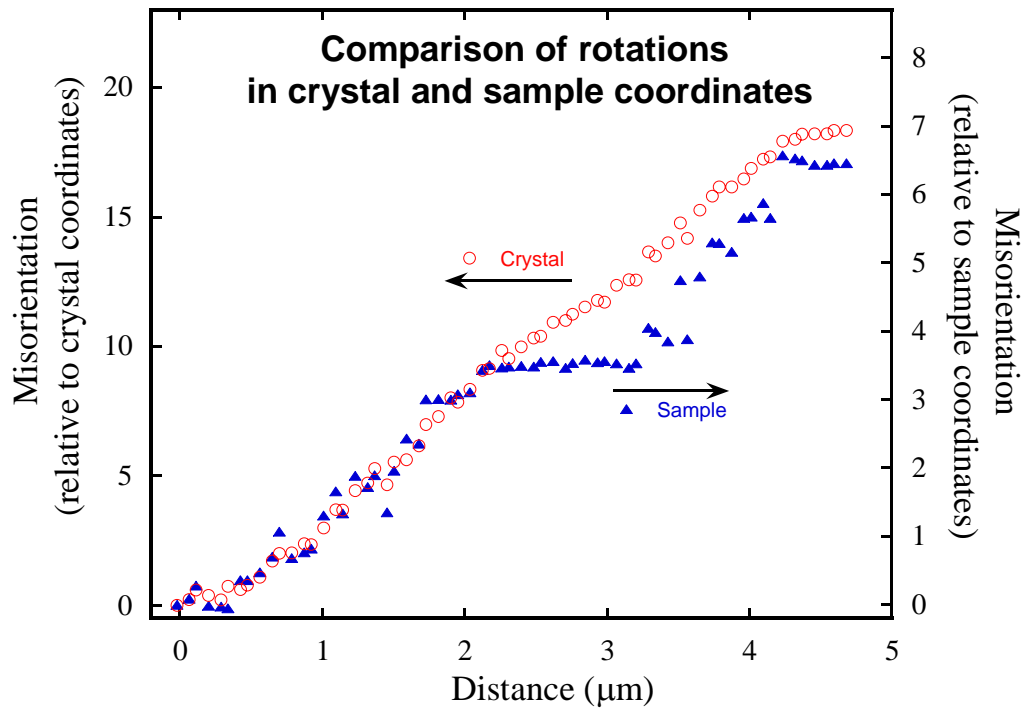


Figure 6.8: Comparison of misorientation in crystal reference coordinates with misorientation in sample reference coordinates with position along the red line shown in Figure 6.3. Note that while the misorientation crystal coordinates varies linearly with position over the entire distance, the misorientation in sample coordinates has distinct changes in slope characteristic of a change in the dominant axis of rotation.

While the RPFs provide strong evidence of the location and type of dislocation causing the observed rotation, further analysis can provide even more information about the dislocation structure. Similar to how rotation axes can be plotted relative to either crystal or sample coordinate systems, misorientation angles can also be plotted relative to either crystal or sample reference frames, as shown in Figure 6.8 for misorientations along the red line shown in Figure 6.3. While the misorientation relative to the crystal is linear with position, the misorientation relative to the sample reference frame is piecewise linear with regions having distinctly different slopes. This is a clear indication that rotations are occurring around different specific axes in different regions, and thus that different arrays of dislocations are dominant in different areas of the film. This conclusion is not inconsistent with our previous interpretation of arrays of edge dislocations on primary slip systems lying in or near the plane of the film, as there are many different primary slip systems on which the arrays of dislocations could be located. Thus, we demonstrate the ability to predict a dislocation structure in phase-transformed tantalum films solely from EBSD data.

6.6 General Discussion

While we have discussed in detail the microstructure and, specifically, the predicted dislocation structure of phase-transformed tantalum films, we have not yet discussed the mechanisms by which such a structure might arise. As can be seen in Figure 6.1, there is a large change in stress during the phase transformation, which is mainly due to densification of the crystal structure [9]. As such, there will be very different local stress levels, and thus very large shear stresses must exist across the phase boundary. It is likely that dislocations are nucleated during the growth of the α phase to relax these shears. If this is the case, there will be a particular dislocation character and Burger's vector that will most efficiently relax the stresses and may lead to arrays of

aligned dislocations such as those discussed earlier. As can be seen from the orientation gradients in Figure 6.3, the orientation of the phase-transformed crystal will gradually change as the phase boundary moves through the film during the transformation. This may cause different arrays of dislocations to be the most efficient at relaxing stresses in different regions of the film. Such a mechanism would necessitate that orientation gradients occur primarily along the direction of α phase growth. This is consistent with the qualitative observation that EBSD maps of phase-transformed films typically demonstrate maximum orientation gradients along the elongated direction of the grains.

6.7 Conclusions

The microstructure of tantalum films both deposited in the bcc α phase and deposited in the β phase and transformed to the α phase by thermal cycling was analyzed using EBSD. While films deposited in the α phase demonstrate a typical thin film microstructure, phase-transformed tantalum films have an unusual microstructure characterized by grains much larger than the film thickness and gradients in crystal orientation within individual grains of up to $4^\circ/\mu\text{m}$. Analysis of the distribution of pixel-to-pixel axes of rotation strongly suggest that these gradients are due to aligned arrays of edge dislocations on primary slip systems located in or near to the plane of the film. It is likely that these arrays of aligned dislocations are the result of large shear stresses that occur in the film during the phase transformation due to the densification of the crystal structure and large changes in local stress.

The authors would like to thank John Hunt for his assistance with the EBSD.

REFERENCES

1. Hoogeveen, R., M. Moske, H. Geisler, and K. Samwer, *Texture and phase transformation of sputter-deposited metastable Ta films and Ta/Cu multilayers*. Thin Solid Films, 1996. **275**, p. 203-206.
2. Westwood, W.D. and F.C. Livermore, *Phase composition and conductivity of sputtered tantalum*. Thin Solid Films, 1970. **5**, p. 407-420.
3. Feinstein, L.G. and R.D. Huttemann, *Factors controlling the structure of sputtered Ta films*. Thin Solid Films, 1973. **16**, p. 129-145.
4. Catania, P., R.A. Roy, and J.J. Cuomo, *Phase formation and microstructure changes in tantalum thin films induced by bias sputtering*. J. Appl. Phys., 1993. **74**(2), p. 1008-1014.
5. Ino, K., T. Shinohara, T. Ushiki, and T. Ohmi, *Ion energy, ion flux, and ion species effects on crystallographic and electrical properties of sputter-deposited Ta thin films*. J. Vac. Sci. Technol. A, 1997. **15**(5), p. 2627-2635.
6. Clevenger, L.A., A. Mutscheller, J.M.E. Harper, C. Cabral, and K. Barmak, *The relationship between deposition conditions, the beta to alpha phase transformation, and stress relaxation in tantalum thin films*. J. Appl. Phys., 1992. **72**(10), p. 4918-4924.
7. Liu, L., H. Gong, Y. Wang, J. Wang, A.T.S. Wee, and R. Liu, *Annealing effects of tantalum thin films sputtered on [001] silicon substrate*. Materials Science and Engineering C, 2001. **16**, p. 85-89.
8. Liu, L., Y. Wang, and H. Gong, *Annealing effects of tantalum films on Si and SiO₂ substrates in various vacuums*. Journal of Applied Physics, 2001. **90**(1), p. 416-420.
9. Knepper, R., B. Stevens, and S.P. Baker, *Effect of oxygen on the thermomechanical behavior of tantalum thin films during the β - α phase transformation*. Journal of Applied Physics, 2006. **accepted**.
10. Thompson, C.V., *Structure evolution during processing of polycrystalline films*. Annu. Rev. Mater. Sci., 2000. **30**, p. 159-190.
11. Humphreys, F.J., Y. Huang, I. Brough, and C. Harris, *Electron backscatter diffraction of grain and subgrain structures - resolution considerations*. Journal of Microscopy, 1999. **195**(3), p. 212-216.
12. Humphreys, F.J., *Grain and subgrain characterisation by electron backscatter diffraction*. Journal of Materials Science, 2001. **36**, p. 3833-3854.
13. Nye, J.F., *Some geometrical relations in dislocated crystals*. Acta Metallurgica, 1953. **1**, p. 153-162.

14. Arsenlis, A. and D.M. Parks, *Crystallographic aspects of geometrically-necessary and statistically-stored dislocation density*. Acta Mater., 1999. **47**(5), p. 1597-1611.
15. El-Dasher, B.S., B.L. Adams, and A.D. Rollett, *Viewpoint: experimental recovery of geometrically necessary dislocation density in polycrystals*. Scripta Materialia, 2003. **48**, p. 141-145.
16. McCabe, R.J., A. Misra, and T.E. Mitchell, *Experimentally determined content of a geometrically necessary dislocation boundary in copper*. Acta Materialia, 2004. **52**(3), p. 705-714.
17. Field, D.P., P. Trivedi, S.I. Wright, and M. Kumar, *Analysis of local orientation gradients in deformed single crystals*. Ultramicroscopy, 2005. **103**, p. 33-39.
18. Field, D.P., M.M. Nowell, P. Trivedi, S.I. Wright, and T.M. Lillo, *Local orientation gradient and recrystallization of deformed copper*. Solid State Phenomena, 2005. **105**, p. 157-162.
19. Li, B.L., A. Godfrey, and Q. Liu, *Investigation of macroscopic grain sub-division of an IF-steel during cold-rolling*. Materials Science Forum, 2002. **408-412**, p. 1185-1190.
20. Phillips, M.A., R. Spolenak, N. Tamura, W.L. Brown, A.A. MacDowell, R.S. Celestre, H.A. Padmore, B.W. Batterman, E. Arzt, and J.R. Patel, *X-ray microdiffraction: local stress distributions in polycrystalline and epitaxial thin films*. Micro-electronic Engineering, 2004. **75**, p. 117-126.
21. Prior, D.J., *Problems in determining the misorientation axes, for small angular misorientations, using electron backscatter diffraction in the SEM*. Journal of Microscopy, 1999. **195**(3), p. 217-225.
22. Bate, P.S., R.D. Knutsen, I. Brough, and F.J. Humphreys, *The characterization of low-angle boundaries by EBSD*. Journal of Microscopy, 2005. **220**(1), p. 36-46.

Chapter 7

Effect of oxygen on the microstructure of phase-transformed tantalum thin films

Robert Knepper, Max Aubain, Ray Fertig, and Shefford P. Baker

*Cornell University, Department of Materials Science and Engineering, Bard Hall,
Ithaca, NY 14853-1501*

7.1 Abstract

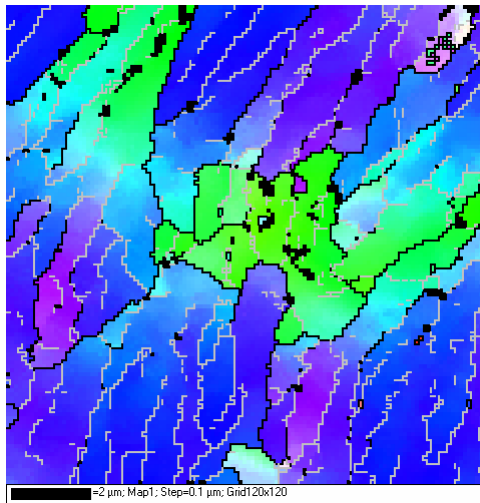
Tantalum films were deposited in the metastable β phase with varying partial pressures of oxygen and transformed to the stable α phase during thermal cycling. The microstructures of the phase-transformed films were investigated using electron backscatter diffraction. As oxygen content increases, the grain size becomes much larger, grain boundaries angle is reduced, and the intragrain orientation gradients observed in oxygen-free phase-transformed films are less prevalent. It is posited that oxygen in the grain boundaries of the as-deposited film reduces the number of α phase nucleation sites, leading to larger grain sizes in the phase-transformed film. Higher transformation temperatures were observed in oxygen-containing films, which will affect dislocation mobility and, consequently, orientation gradients. Thus, the addition of oxygen to tantalum films during deposition is an effective method of controlling not only the temperature of the β - α phase transformation, but the resultant microstructure as well.

7.2 Introduction

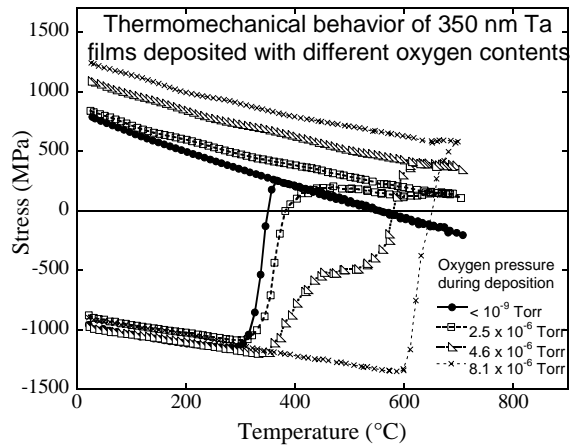
Tantalum thin films have been studied due to their applications in microelectronic devices and in x-ray optics. Depending on deposition conditions and substrate [1-5], tantalum films can be deposited with two different crystal structures: the stable bcc α phase or the metastable tetragonal β phase. The β phase is found only in thin films and has a high resistivity ($\sim 180 \mu\Omega \text{ cm}$), making it suitable for thin film resistors and heaters. β tantalum is also easier to pattern using reactive ion etching than the α phase [6] and is therefore used for masks in x-ray optics. The α phase has a much lower resistivity ($\sim 13 \mu\Omega \text{ cm}$), is less brittle, and is commonly used for thin film interconnections and capacitors and as a diffusion barrier between copper and silicon in microelectronic devices.

It has been observed that tantalum films deposited in the β phase can transform to the α phase upon sufficient heating and that the transformation will be accompanied by a significant change in stress in the tensile direction [7, 8]. We have previously shown that the microstructure of oxygen-free tantalum films that have undergone the β - α phase transformation is quite different than the microstructure seen in similar films that were directly deposited in the α phase [9]. The phase-transformed microstructure is instead characterized by a discontinuous grain boundary network and continuous gradients in crystal orientation within individual grains of up to $4^\circ/\mu\text{m}$, as shown in Figure 7.1a.

We have also shown previously that adding a small partial pressure of oxygen to the deposition atmosphere ($\sim 10^{-6}$ Torr) inhibits the β - α phase transformation by increasing the activation energy for boundary motion, thus requiring higher temperatures for the transformation to reach completion, as seen in Figure 7.1b [8]. Oxygen content also affects the microstructure: grain size, orientation distribution, and orientation gradients. In this paper, we explore these microstructural differences using electron back-



(a)



(b)

Figure 7.1: (a) EBSD map of a 300 nm oxygen-free tantalum film deposited in the β phase and transformed to the α phase during thermal cycling [9]. The oxygen-free phase-transformed film has a discontinuous grain boundary structure, and continuous gradients in crystal orientation within individual grains. (b) Stress-temperature plot of tantalum films deposited with varying partial pressures of oxygen [8]. Increasing oxygen content inhibits the phase transformation, requiring higher temperatures to initiate and to reach completion.

scatter diffraction (EBSD) and discuss some of the mechanisms that might account for these differences.

7.3 Experiment

7.3.1 Sample Preparation

Samples were prepared by magnetron sputter deposition in an ultra-high vacuum (UHV) chamber evacuated to less than 2×10^{-9} Torr using equipment described in detail elsewhere [8]. 100 mm diameter oxidized Si (100) substrates were used. Before deposition, each substrate was cleaned using a 25 W radio-frequency bias in 8 mTorr of argon for 1 minute to remove adsorbed gas molecules from the substrate surface. Tantalum films were then sputtered to a thickness of 300–400 nm using a DC magnetron source and a 99.95% pure Ta target. A sputtering pressure of 8 mTorr of argon and a sputtering power of ~ 400 W were used. Oxygen was incorporated into the films by adding a fixed oxygen partial pressure in the range of 2.5×10^{-6} to 8.1×10^{-6} Torr to the sputtering gas during deposition by use of a leak valve, with the partial pressure measured both before and after deposition. The Ta deposition rate was approximately 15 nm/min. All films were deposited with the substrate grounded. Substrates were rotated at 5 rpm and were unheated during deposition. The maximum temperature reached during deposition was approximately 100°C, as measured by a thermocouple located behind the substrate.

After deposition, samples were transferred to a vacuum furnace within the same UHV system. Samples were then thermally cycled between room temperature and 700°C at 5°C/min. Films deposited in the β phase transformed to the α phase during thermal cycling, as determined by *ex situ* x-ray analysis.

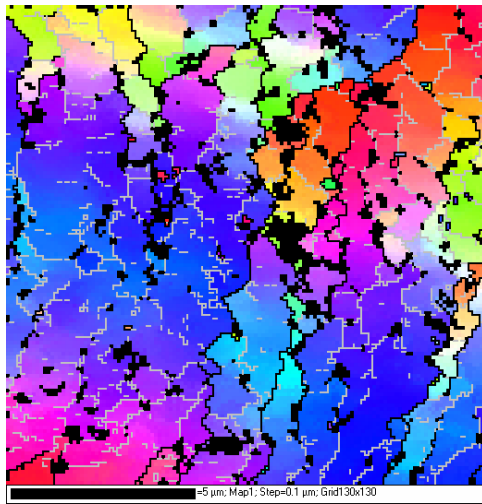
7.3.2 Microstructure Characterization

EBSD was used to determine local crystallographic orientation information in both as-deposited and phase-transformed α tantalum films. The EBSD system (HKL Technology, Inc.) operates in conjunction with a Leica 440 SEM operating at 25 kV and 1.2 nA as described elsewhere [9]. By scanning an array of points with 100 nm spacing over a $12\ \mu\text{m} \times 12\ \mu\text{m}$ grid, detailed crystallographic orientation maps are generated. Similar arrays, scanned at a lower resolution and over a larger area (1–2 μm spacing over $\sim 100\ \mu\text{m}$), are used to provide a more general view of the orientation distribution within each sample.

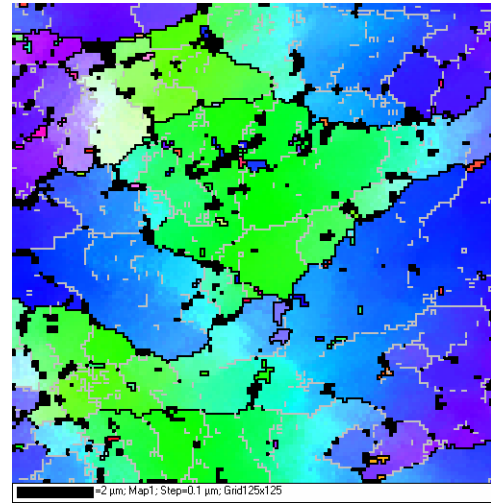
Grain sizes and the distribution of boundary angles were determined from several series of line scans with a 100 nm measurement spacing along the line and several μm between lines. Boundaries were defined as abrupt changes in orientation of more than 2° where the orientation on either side of the boundary remained relatively constant for at least two pixels. Single pixel grains were not considered, as it was impossible to determine from the line scans if such points were correctly indexed. As such, only grains larger than $\sim 200\ \text{nm}$ were considered in the current analysis.

7.4 Results

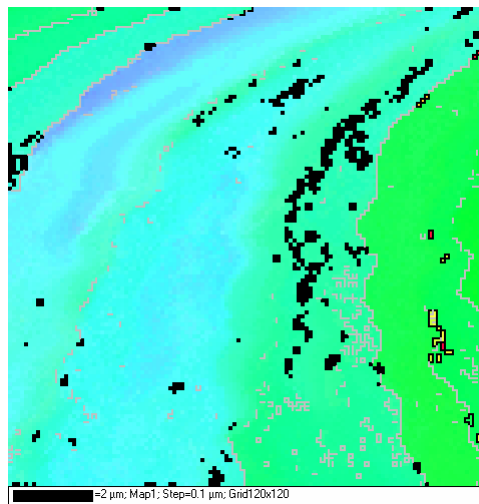
EBSD maps of phase-transformed tantalum films that were deposited with 2.5×10^{-6} , 4.6×10^{-6} , and 8.1×10^{-6} Torr of oxygen are shown in Figure 7.2. The black lines in the images depict high-angle grain boundaries (defined as a misorientation between neighboring pixels of greater than 8°), while gray lines indicate low-angle grain boundaries (defined as a misorientation between neighboring pixels of between 2° and 8°). Black pixels indicate regions where the EBSD software was not able to match the measured Kikuchi pattern with a corresponding α -Ta crystal orientation. As can be seen in the EBSD maps, the local microstructure changes dramatically with the addi-



(a)



(b)



(c)

Figure 7.2: EBSD maps of phase-transformed tantalum films deposited with (a) 2.5×10^{-6} , (b) 4.6×10^{-6} , and (c) 8.1×10^{-6} Torr of oxygen.

tion of increasing amounts of oxygen to the film. Immediately visible is the increase in grain size with increasing oxygen content. As shown in Figure 7.3, while smaller amounts of oxygen have little or no effect on the grain size, the average grain size increases by nearly an order of magnitude with the addition of 8.1×10^{-6} Torr of oxygen. In addition, small angle grain boundaries constitute a much larger fraction of the boundaries as the oxygen content in the film increases, as shown in Figure 7.4. Further, the large, continuous gradients in crystal orientation seen in films with little or no oxygen added during deposition appear much less frequently in the film deposited with 8.1×10^{-6} Torr of oxygen and cover a much smaller part of the film. Figure 7.5 shows the distribution of misorientations between neighboring pixels in the EBSD maps of phase-transformed tantalum films in Figure 7.1. While all films have a peak at $\sim 0.4^\circ/\text{pixel}$, the film deposited with 8.1×10^{-6} Torr of oxygen has an additional peak at $\sim 0.1^\circ/\text{pixel}$ (approximately the precision of the system), indicating that a substantial fraction of the film has only very small local gradients in crystal orientation. The global distribution of out-of-plane crystal orientations also changes considerably with oxygen content, as shown in the out-of-plane inverse pole figures (IPFs) in Figure 7.6. In films with lower oxygen concentrations, the IPFs remain nearly constant, with peaks slightly offset from the (111) out-of-plane orientation and comparable spreads in the distributions of orientations, though the spread is somewhat larger for the film deposited with 4.6×10^{-6} Torr of oxygen. The IPF undergoes a dramatic change in the film deposited with 8.1×10^{-6} Torr of oxygen. While there is still only one peak evident in the distribution, it moves to a position near a (110) out-of-plane orientation and is significantly sharper than those seen in the other films.

The distribution of axes of rotation between neighboring pixels in the EBSD orientation maps were analyzed using rotation pole figures (RPFs). As described previously [9], RPFs plot the distribution of all axes of rotation between neighboring pixels in an

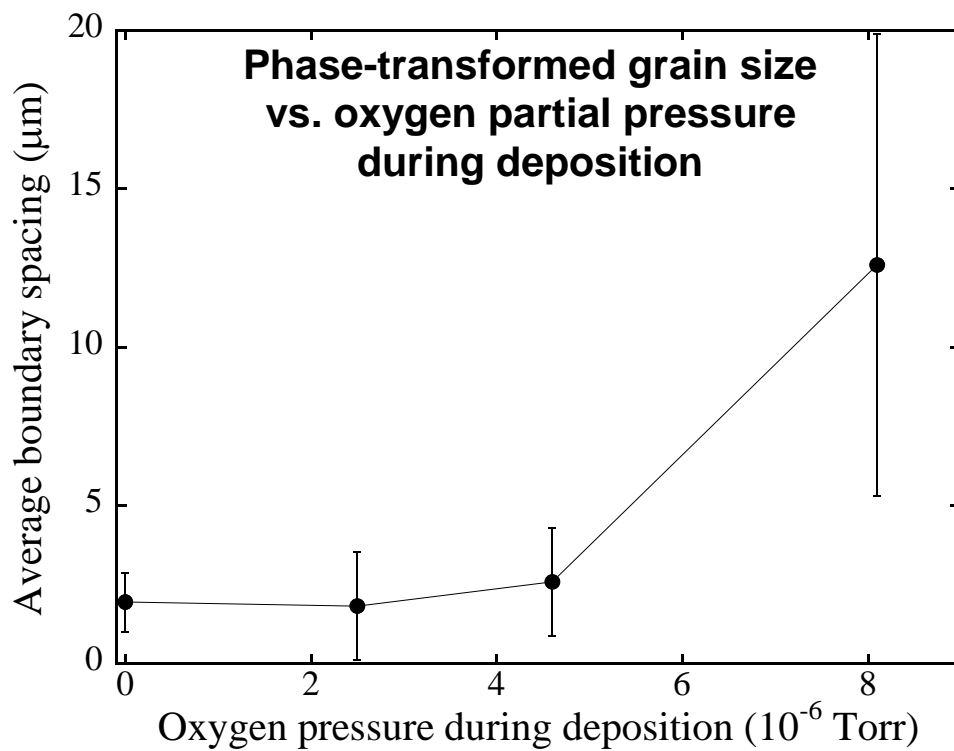


Figure 7.3: Plot of average grain size with oxygen content. Error bars indicate the standard deviation. The grain size increases with increasing oxygen.

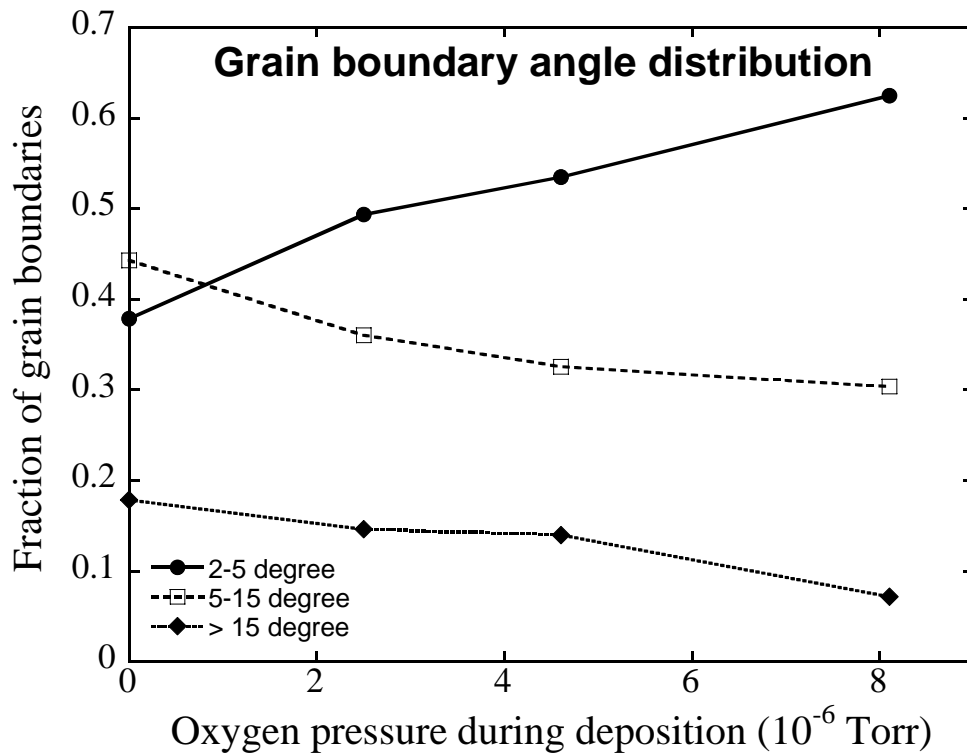


Figure 7.4: Histograms showing the variation in grain boundary angles with increasing oxygen partial pressure during deposition. As the oxygen content increases, high-angle grain boundaries are gradually replaced with a greater percentage of low-angle boundaries.

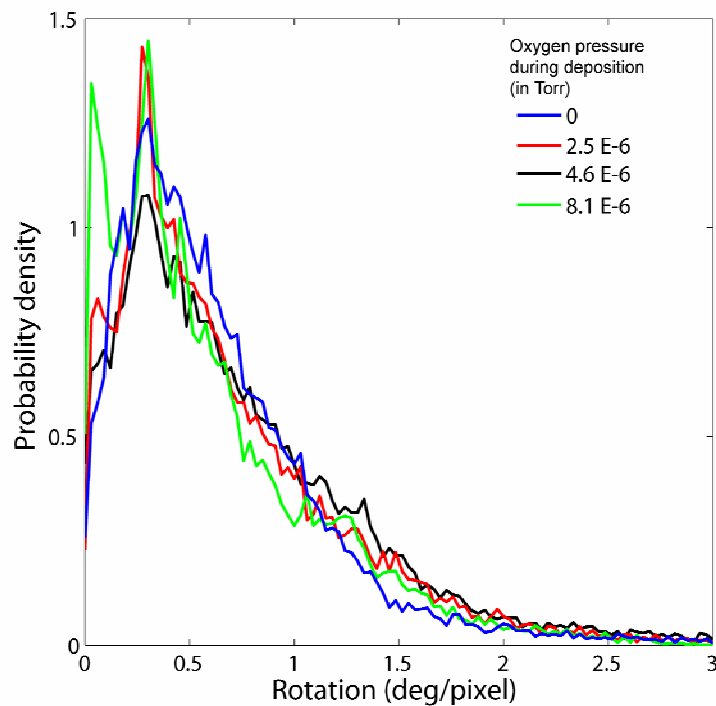


Figure 7.5: Comparison of the distribution of misorientations between neighboring pixels with increasing oxygen partial pressure during deposition. While all films show a peak at $\sim 0.4^\circ/\text{pixel}$, note appearance of a second peak at $\sim 0.1^\circ/\text{pixel}$ in the film deposited in 8.1×10^{-6} Torr of oxygen.

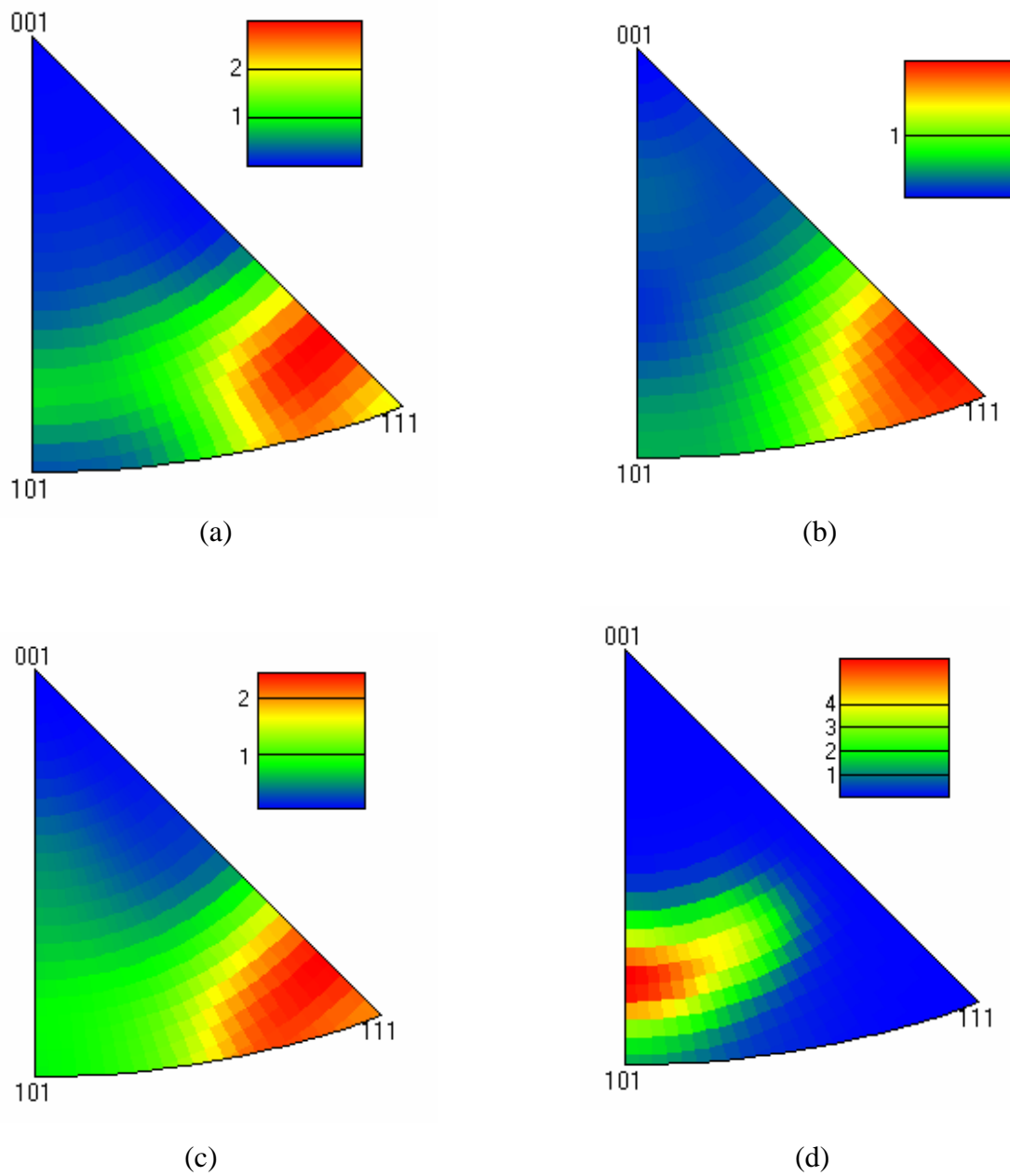


Figure 7.6: Inverse pole figures depicting the out-of-plane crystal orientation distribution in phase-transformed tantalum films deposited with (a) no oxygen, (b) 2.5×10^{-6} , (c) 4.6×10^{-6} , and (d) 8.1×10^{-6} Torr of oxygen. All IPFs are normalized to their mean intensity, with color scaling as shown.

EBSD orientation map (excluding those across high-angle grain boundaries) on a stereographic plot. These rotation axes can be plotted relative to either the crystal unit cell coordinate axes (crystal RPF) or relative to a fixed real-space coordinate system (sample RPF). Crystal RPFs can be used to show whether rotations occur around particular crystallographic axes, as would be the case if a particular type and character of dislocation were responsible for the rotations. Similarly, sample RPFs can be used to show if rotations occur about particular directions in the sample.

A series of crystal and sample RPFs for various ranges of misorientations between neighboring pixels smaller than 2° (the minimum for low-angle grain boundaries) are shown in Figures 7.7 and 7.8 for an oxygen-free film and the film deposited with 8.1×10^{-6} Torr of oxygen, respectively. RPFs are shown for small ($0-0.2^\circ$ for the oxygen-free film, $0-0.1^\circ$ for the oxygen-containing film), moderate ($0.2-0.45^\circ$ for the oxygen-free film, $0.1-0.35^\circ$ for the oxygen-containing film), and large ($0.45-2^\circ$ for the oxygen-free film, $0.35-2^\circ$ for the oxygen-containing film) misorientations. For small misorientations, rotation axes are distributed randomly in both films in crystal and sample coordinates, with a slight preference for [211] crystal axes in the oxygen-free film. Both films show a substantial peak around the [211] crystal axis in the crystal RPF for moderate misorientations and have rotation axes near the plane of the film, as seen in the sample RPF. However, while the oxygen-free film shows a distribution of rotation axes around an arc in the sample RPF, the oxygen-containing film has only a single strong peak. For large misorientations, the RPFs are very different. The crystal RPF for the oxygen-free film looks very similar to the one for small misorientations, with a mostly random distribution and slight preference for [211] crystal axes. The sample RPF, however, shows only a single peak $\sim 45^\circ$ from the film normal. In the oxygen-containing film, the crystal RPF has a diffuse peak in the vicinity of the [111] crystal axis while the sample RPF shows two distinct peaks: a sharp, intense peak in the same

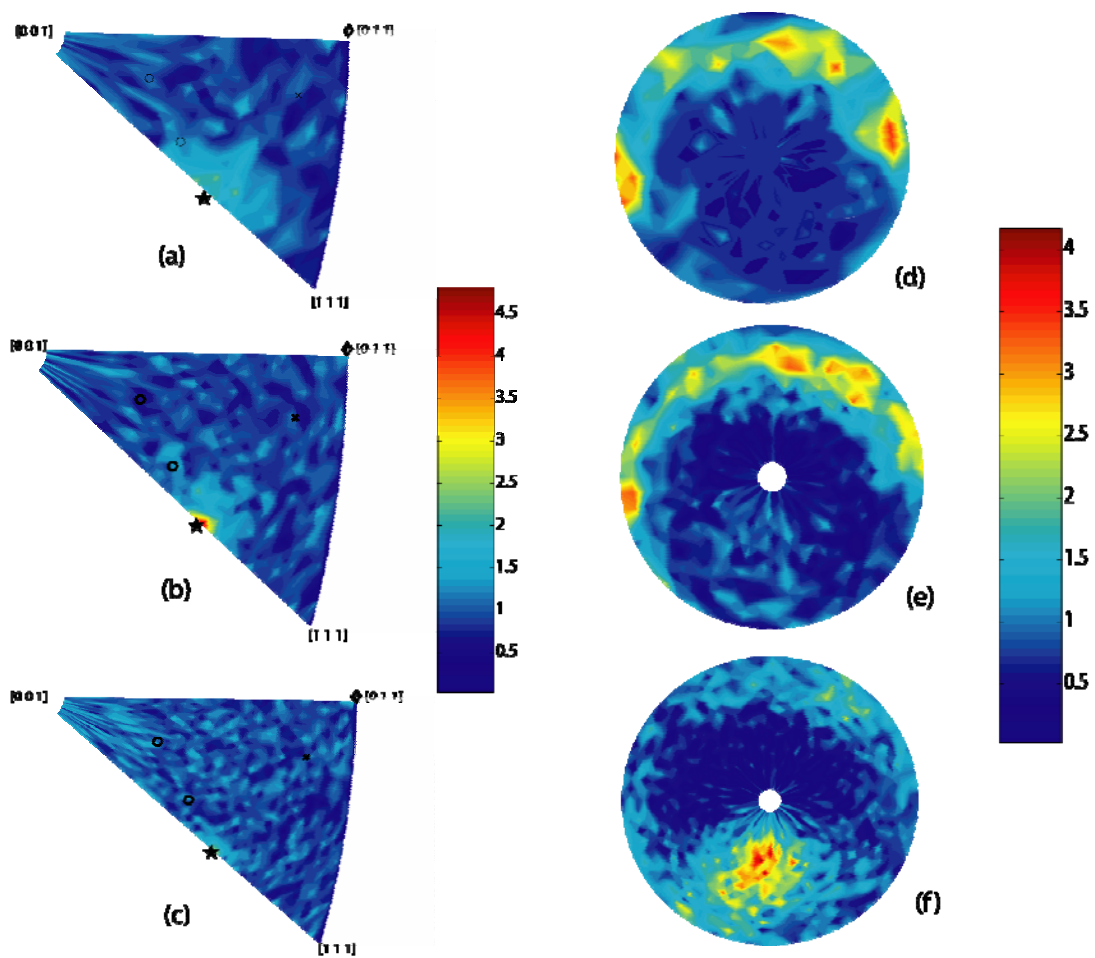


Figure 7.7: Rotation pole figures showing distributions of axes of rotation in an oxygen-free film in crystal and sample coordinates for (a) and (d) 0-0.2°, (b) and (e) 0.2-0.45°, and (c) and (f) 0.45-2° misorientations.

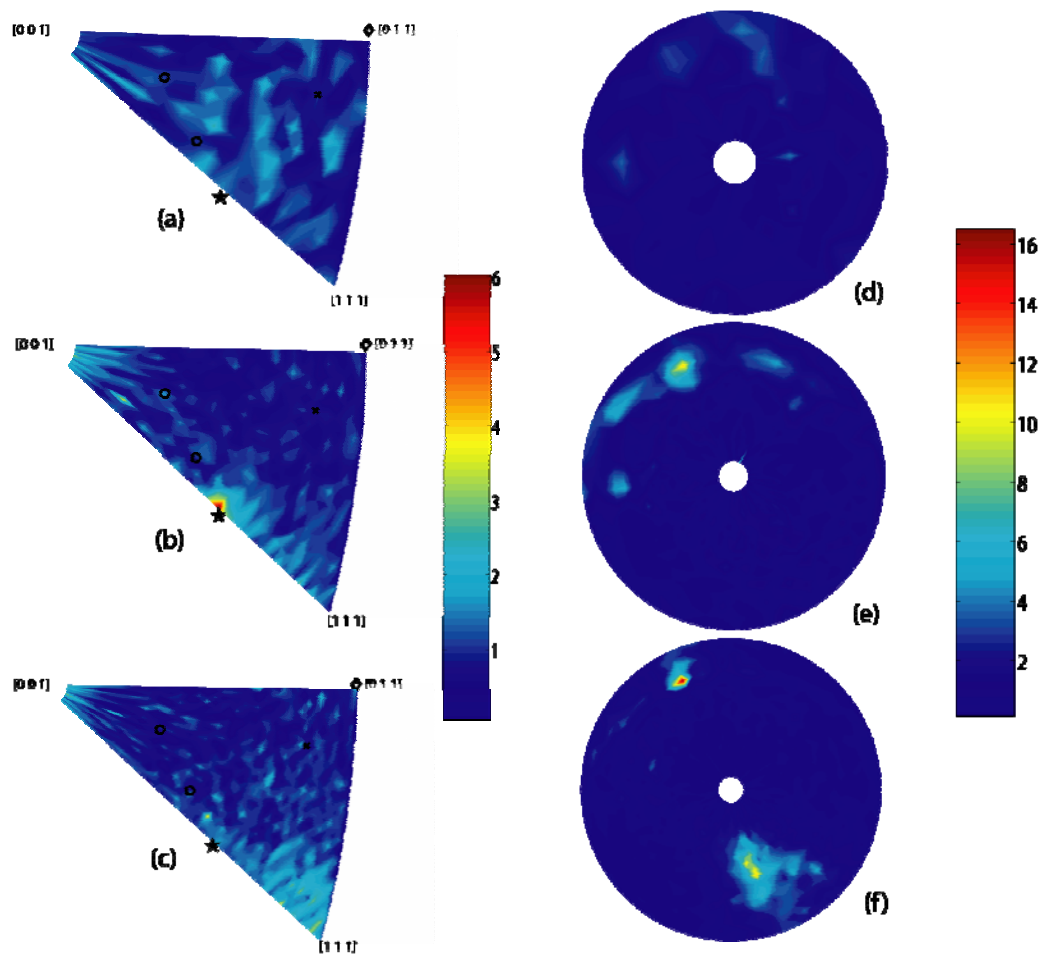


Figure 7.8: Rotation pole figures showing distributions of axes of rotation in the film deposited with 8.1×10^{-6} Torr of oxygen in crystal and sample coordinates for (a) and (d) $0-0.1^\circ$, (b) and (e) $0.1-0.35^\circ$, and (c) and (f) $0.35-2^\circ$ misorientations.

location as the peak at moderate misorientations, and a more diffuse peak in the same location as in the oxygen-free film. Interpretation of these features is discussed in the following section.

7.5 Discussion

As the grain size increases significantly with increasing oxygen content, either α phase nucleation is inhibited or fewer nuclei are able to grow. As shown by Jiang *et al* [10] in molecular dynamics simulations, homogeneous nucleation of α phase nuclei in a β crystallite is very unlikely and was not observed in their simulations of the β - α phase transformation in tantalum films. As such, the other alternatives for α phase nucleation are either during deposition or heterogeneous nucleation along grain boundaries or other surfaces. As oxygen incorporated during deposition is likely to segregate to the grain boundaries of the β phase film, it may inhibit the formation of α nuclei, similar to the observations of Lucke and Detert in recrystallization experiments [11]. A smaller number of nuclei would then lead to a larger grain size in the phase-transformed film. Alternatively, if nucleation is not inhibited or if nuclei are already present from deposition, growth may begin in regions where the local oxygen concentration is low due reduced solute drag. As the phase boundary moves and encounters additional oxygen, some of the energy recovered during the transformation may serve to drive oxygen from the film, as described by in an earlier paper [8].

Previously, we showed that RPFs can be used to infer the structure of arrays of geometrically necessary dislocations that cause the large orientation gradients in phase-transformed tantalum films [9]; the [211] peak in the crystal RPF is indicative of edge dislocations on primary bcc slip systems, and the sample RPF showed that the axes of rotation, and thus the arrays of edge dislocations, lay in or near to the plane of the film. While the rotation axes found for small misorientations are mostly random,

the consistent peak in the distribution of axes of rotation in the crystal in the [211] direction for both films indicates that the mechanism leading to the formation of geometrically necessary dislocations is consistent, regardless of the oxygen content of the film. While the mechanism for dislocation formation remains consistent, something in the film deposited with 8.1×10^{-6} Torr of oxygen suppresses the large, continuous orientation gradients seen in the films having smaller oxygen contents. A possible explanation relies on the ability of oxygen to inhibit the phase transformation and the high transformation temperature of the film deposited with 8.1×10^{-6} Torr of oxygen (see Figure 7.1). If dislocations with a preferred orientation are nucleated during the transformation, the driving force for dislocation motion will be the highest when the phase boundary is near because of the large shear stresses that develop due to the difference in stress across the boundary between the β and α phases. The higher transformation temperature for the film deposited with 8.1×10^{-6} Torr of oxygen allows for greater dislocation mobility while the driving force is high and may lead to a significant fraction of the dislocations moving on their slip planes to the film surfaces where they would no longer contribute to an orientation gradient.

For larger misorientations, it appears that a different mechanism dominates dislocation formation, as the crystal RPFs are mostly random, while the sample RPFs show distinct peaks. This indicates that no particular dislocation orientation or character is preferred in the crystal, but there is still a preferred orientation in the sample. We are currently unable to explain why a preferred axis of rotation relative to the sample persists in the film when there are no apparent preferred dislocations. In addition, the differences in the distributions of crystal orientations or grain boundary angles with increasing oxygen content remain unexplained. As the current data is insufficient to determine all aspects of the dislocation structure of phase-transformed tantalum films and its variation with oxygen content, atomistic simulations a polycrystalline tantalum

film during the β - α phase transformation may provide a greater understanding of the mechanisms controlling these factors as well as to confirm the mechanisms suggested to control grain size and orientation gradient.

7.6 Conclusions

The addition of oxygen to β phase tantalum films during deposition has a large impact on the microstructure of the phase-transformed film. As oxygen content increases, the grain size becomes much larger, average grain boundaries angle decreases, and the intragrain orientation gradients observed in oxygen-free phase-transformed films are less prevalent. The higher transformation temperatures for oxygen-containing films may allow for enhanced dislocation mobility to the interfaces and lead to fewer orientation gradients in the phase-transformed film. The addition of oxygen to tantalum films during deposition is an effective method of controlling not only the temperature of the β - α phase transformation, but the resultant microstructure as well.

The authors would like to thank John Hunt for his assistance with the EBSD system.

REFERENCES

1. Westwood, W.D. and F.C. Livermore, *Phase composition and conductivity of sputtered tantalum*. Thin Solid Films, 1970. **5**, p. 407-420.
2. Feinstein, L.G. and R.D. Huttemann, *Factors controlling the structure of sputtered Ta films*. Thin Solid Films, 1973. **16**, p. 129-145.
3. Catania, P., R.A. Roy, and J.J. Cuomo, *Phase formation and microstructure changes in tantalum thin films induced by bias sputtering*. J. Appl. Phys., 1993. **74**(2), p. 1008-1014.
4. Hoogeveen, R., M. Moske, H. Geisler, and K. Samwer, *Texture and phase transformation of sputter-deposited metastable Ta films and Ta/Cu multilayers*. Thin Solid Films, 1996. **275**, p. 203-206.
5. Ino, K., T. Shinohara, T. Ushiki, and T. Ohmi, *Ion energy, ion flux, and ion species effects on crystallographic and electrical properties of sputter-deposited Ta thin films*. J. Vac. Sci. Technol. A, 1997. **15**(5), p. 2627-2635.
6. Kondo, K., M. Nakabayashi, K. Kawakami, T. Chijimatsu, M. Nakaishi, M. Yamada, M. Yamabe, and K. Sugishima, *Stress stabilization of β -tantalum and its crystal structure*. J. Vac. Sci. Technol. A, 1993. **11**, p. 3067-3071.
7. Clevenger, L.A., A. Mutscheller, J.M.E. Harper, C. Cabral, and K. Barmak, *The relationship between deposition conditions, the beta to alpha phase transformation, and stress relaxation in tantalum thin films*. J. Appl. Phys., 1992. **72**(10), p. 4918-4924.
8. Knepper, R., B. Stevens, and S.P. Baker, *Effect of oxygen on the thermomechanical behavior of tantalum thin films during the β - α phase transformation*. Journal of Applied Physics (accepted).
9. Knepper, R., R.S. Fertig, K. Jackson, and S.P. Baker, *Microstructure of phase-transformed tantalum thin films*. (in preparation).
10. Jiang, A., T.A. Tyson, and L. Axe, *The stability of the β -phase of tantalum: a molecular dynamics study*. J. Phys.: Condens. Matter, 2005. **17**, p. 1841-1850.
11. Lucke, K. and K. Detert, *A quantitative theory of grain-boundary motion and recrystallization in metals in the presence of impurities*. Acta Metallurgica, 1957. **5**, p. 628-637.

Chapter 8

Summary and Outlook

Tantalum films have been deposited with excellent control over the amount of impurities added. Oxygen-free films deposited in the metastable β phase have been shown to transform to the stable α phase at temperatures much lower than previously reported. The coefficient of thermal expansion and biaxial elastic modulus for as-deposited β phase and phase-transformed α phase films were calculated from the thermoelastic slopes of films deposited on (100) silicon and amorphous fused silica substrates. The large change in stress in the tensile direction that accompanies the transformation is due to film densification caused by the change in crystal structure and the elimination of free volume associated with grain boundaries in the as-deposited film. The β - α phase transformation has been shown to be a nucleation and growth process that is limited by growth and the driving force for the transformation has been measured using DSC.

EBSD analysis of phase-transformed tantalum films showed a very unusual microstructure that has not been previously seen in which the grain sizes were approximately an order of magnitude greater than the film thickness, the grain boundary structure was discontinuous, and large continuous gradients in crystal orientation of up to $4^\circ/\mu\text{m}$ within individual grains were common. Analysis of the distribution of axes of rotation using rotation pole figures was used to determine the orientation and character of arrays of geometrically necessary dislocations that could account for the observed microstructure. The addition of oxygen during deposition also had a large impact on

the resultant phase-transformed microstructure. Increasing oxygen content resulted in a much larger grain size, a smaller average grain boundary angle, reduced orientation gradients, and a change in preferred out-of-plane crystal orientation.

The addition of oxygen to the film either by depositing in an oxygen-containing atmosphere, by exposing to oxygen immediately following deposition and forming a surface oxide, or by thermally cycling in an oxygen-containing atmosphere inhibited the phase transformation by solute drag and required higher temperatures to completely transform the film from β to α . The increase in activation energy necessary for the transformation to progress was estimated as a function of oxygen content in the film.

The work detailed in this thesis not only provides insight into the reliability of tantalum films in devices from the very large stresses that develop during both the β - α phase transformation and oxygen incorporation, but can also provide a basis for engineering tantalum films to best suit the application at hand. Control of the oxygen content in a deposited β phase film can be used to impose a particular transformation temperature, allowing films to be easily patterned in the β phase and then transformed to the α phase at low temperatures for use in applications like diffusion barriers, or wear and corrosion resistant coatings where the α phase is preferred. Alternatively, adding oxygen to a film allows it to remain in the β phase at very high temperatures, which can be useful for thin film resistors and heaters where β phase films are often used. Oxygen addition may allow not only for control over the temperature at which the transformation occurs, but also of the resultant phase-transformed microstructure, making it possible to engineer the microstructure of α phase films and exert control over both crystal orientation and grain size.

Further experiments are suggested to elucidate the grain and dislocation structure, the mechanisms of α phase and dislocation nucleation, and to study tantalum films

under conditions closer to those seen in many devices. Some suggested experiments are:

- TEM – Plan view samples can be analyzed for total dislocation density and to determine whether dislocations are uniformly distributed or organized into subgrain boundaries in phase-transformed films. Further, cross-section samples can be used to determine how dislocations are distributed through the thickness of the film, whether there are any significant differences in crystal structure through the thickness in phase-transformed films, and also to observe the grain structure of as-deposited films in the β phase.
- Effects of film thickness – The tantalum films used in many applications (such as diffusion barriers between copper and silicon) are often significantly thinner than those in the current study. Preliminary experiments suggest that phase-transformed microstructure can vary significantly with film thickness; further study is necessary to quantify how it varies.
- Effect of interface – Tantalum films may be deposited on many different surfaces for different applications which can lead to differences in phase and/or texture in the film. Only a limited number of substrates have been studied here; others common in various applications (i.e. TaN_x in diffusion barriers [1] or steel for wear-resistant gun barrel coatings [2]) have not.
- UHV DSC – DSC experiments in this thesis were conducted in an atmosphere that contained significant amounts of oxygen, which greatly inhibited the phase transformation. Conducting similar DSC measurements with UHV background pressures would allow for much better control over the reactions that may occur during testing.
- Properties of phase-transformed films – Phase-transformed tantalum films have a microstructure that is very different from bulk tantalum or films de-

posited in the α phase. As such, they may have properties well-suited to a number of applications. For example, wear-resistant coatings may last longer and diffusion barriers may perform better due to the large grain sizes and few high-angle grain boundaries present in the phase-transformed films.

- Effects of constrained dimensionality – Patterned films can behave differently than blanket films as the stress in a patterned line is no longer distributed in an equal biaxial manner. This may lead to significant variations in phase-transformed microstructure that have not been studied.
- Similar systems – Metastable crystal structures similar to β -Ta have been observed in both tungsten [3] and chromium [4]. Do these systems behave in a manner similar to that seen for tantalum films?
- Molecular dynamics simulations – Atomistic simulations of the β - α phase transformation have the potential to provide a great deal of insight as to the mechanisms behind α phase nucleation and dislocation nucleation and motion during the transformation. In addition, such simulations could also quantify the effects of oxygen contamination at the atomic scale and explain why particular out-of-plane crystal orientations are more prevalent than others. To accurately model the transformation, such a simulation must account for the both the substrate and the small-grained polycrystalline structure of the as-deposited β phase.

REFERENCES

1. Shimada, H., I. Ohshima, T. Ushiki, S. Sugawa, and T. Ohmi, *Tantalum nitride metal gate FD-SOI CMOS FETs using low resistivity self-grown bcc-tantalum layer*. IEEE Transactions on Electron Devices, 2001. **48**(8), p. 1619-1626.
2. Lee, S.L., D. Windover, M. Audino, D.W. Matson, and E.D. McClanahan, *High-rate sputter deposited tantalum coating on steel for wear and erosion mitigation*. Surface and Coatings Technology, 2002. **149**, p. 62-69.
3. Rossnagel, S.M., I.C. Noyan, and C. Cabral Jr., *Phase transformation of thin sputter-deposited tungsten*. Journal of vacuum Science and Technology B, 2002. **20**(5), p. 2047-2051.
4. O'Keefe, M.J., S. Horiuchi, J.M. Rigsbee, and J.P. Chu, *Effect of oxygen and carbon on the formation and stability of A-15 crystal structure chromium thin films*. Thin Solid Films, 1994. **247**, p. 169-177.